In-situ analysis on interfacial nano-structures and reactions by using surface-enhanced Raman spectroscopy

表面増強ラマン分光法を用いた界面ナノ構造および反応プロセスの in-situ 解析

February, 2017

Yingying SUN

ソン　エイエイ

In-situ analysis on interfacial nano-structures and reactions by using surface-enhanced Raman spectroscopy

表面増強ラマン分光法を用いた界面ナノ構造および
反応プロセスの in-situ 解析

February, 2017

Waseda University
Graduate School of Advanced Science and Engineering
Department of Applied Chemistry, Research on Interface Electrochemistry

Yingying SUN
ソン　エイエイ

Preface

Chemistry of interfaces and surfaces play a key role in understanding numbers of diverse phenomena, such as chemical reactions, electrochemical processes, nanoparticle behavior, and so on. In-situ studies on these interfacial processes and depth profiling play an important role for properly addressing the issues of worldwide relevance, and for this, experimental methods, which discriminate interfacial structure with high resolution, are required. Raman spectroscopy is a powerful technique which can achieve in-situ observation of the molecular vibration. Nevertheless, it is known that some vibrations show weak Raman scattering so that micro constituents are difficulty to be observed by this approach. In these situations, surface-enhanced Raman spectroscopy (SERS) could be beneficial to enhance weak Raman signals and distinguish the vibration of a group or a chemical bond in the sample with low concentration. However, for the analysis of the interfacial reaction, SERS is not widely employed comparing to other traditional approaches, due to the confined SERS sensor to enhance the signals.

To advance the interfacial analysis, Raman spectroscopy and SERS were employed in this study to realize the analysis on several ultra-thin samples. The originality of this study is applying the SERS sensors and realizing in-situ and kinetic measurements on three types of nano-films, with high sensitivity and resolution. In addition, temperature calculation from anti-Stokes Raman scattering and depth profile with a step of 0.1 nm also support the interface analysis. The measurements and analyses were successfully expanded to various kinds of nano-film samples, including (3-aminopropyl) triethoxysilane derived self-assembled monolayers (APTES SAMs), single layer graphene (SLG), and the solid-electrolyte interface (SEI) films formed at the electrode surface of Li-ion battery (LIB).

In this study, APTES SAMs and SLG with known structure were used to evaluate the application potential of SERS and Raman spectroscopy in analyzing the interfacial reaction of thin-film materials. Meanwhile, some new phenomena were also discovered on these samples, including the analysis on the phase transition, the accurate vertical structure and the two interfacial junctions of APTES SAMs, and the thermal stability of SLG. Furthermore, SERS was applied to characterize the SEI layers in LIB, including the kinetics of their formation, the depth profiling, and their generation mechanism focusing upon the species such as Li_2CO_3. The in-situ interfacial observation on the thin-film materials was completed with atomic resolution, high quality and kinetically by using the SERS sensors.

This thesis constitutes to five chapters as below.

Chapter 1 is the general introduction. It explains the motivation of the entire research, the techniques employed, the target samples and the strategy in this study. Some fundamental concepts and theories are introduced. Moreover, some important supporting approaches are also explained in detail.

Chapter 2 demonstrates the ability of SERS in the interfacial analysis of nanoscale structures. The depth profiling of APTES SAMs was observed using SERS at atomic level, combining with a piezo field gradient device. It distinguishes the vertical vibrations from specific groups and analyzes the orientation in APTES SAMs. In addition, it also describes the in-situ anti-Stokes and Stokes Raman spectroscopy observation on phase transition process of APTES SMAs and the thermal stability of SLG, subjected to confocal laser heating.

In chapters 3 and 4, SERS is further applied to the interfacial analysis of LIB electrodes, to observe the important but unclear structure, the SEI films. Chapter 3 presents the kinetic observation on SEI film formation and thermal stability at the graphite electrode, which is measured by using SERS sensor. Furthermore, the real-time 2D mapping of the SEI formation is carried out by using the Raman microscopy installed with 11 x 11 multi-laser spots.

Chapter 4 further investigates the Li_2CO_3 products by using Au NPs SERS sensor and figures out the mechanism of Li_2CO_3 formation. The interfacial behavior of PC and EC at the surface of graphite is deeply explored and its relation with interfacial reduction pathway is analyzed. Finally, the depth profiling of SEI film is presented to observe the location of Li_2CO_3 product in SEI film.

Chapter 5 summarizes the observations and discoveries from the analysis of this study. Some perspectives are also discussed for future improvement.

Table of contents

Preface ..... **I**

Table of contents ..... **III**

CHAPTER 1: GENERAL INTRODUCTION

1.1 Introduction of Raman spectroscopy and SERS **2**

1.1.1 Raman spectroscopy 2

1.1.2 Surface-enhanced Raman spectroscopy (SERS) 5

1.1.2.1 The theory of SERS 5

1.1.2.2 SERS sensor 6

1.1.2.3 Application of SERS 10

1.1.3 Time-resolved measurement 13

1.1.3.1 Observation on kinetic reaction 13

1.1.3.2 Kinetic temperature calculation 14

1.1.4 Depth profile measurement 16

1.2 Introduction of three target samples **18**

1.2.1 APTES SAMs 18

1.2.2 Single layer Graphene (SLG) 20

1.2.3 SEI film in Li-ion battery 21

1.2.3.1 Basic theory in Li-ion battery 21

1.2.3.2 Chemistry of SEI film in Li-ion battery 22

1.2.3.3 Controversies in SEI film 22

1.2.3.4 Characterization techniques 25

1.3 Strategy of this research **27**

References **28**

CHAPTER 2: ANALYSIS ON NANO-FILM SAMPLES: DEPTH PROFILE AND KINETIC REACTION

2.1 Introduction **36**
2.1.1 Depth profile on APTES SAMs 36
2.1.2 Kinetic reaction of APTES SAMs 37
2.1.3 Kinetic reaction of SLG 38
2.2 Experimental section **40**
2.2.1 Samples and materials 40
2.2.2 Raman Spectroscopy and SERS 41
2.2.3 Atomic Force Microscopy (AFM) 41
2.2.4 Depth profile measurement on APTES SAMs using Raman spectroscopy and piezo electric stage 41
2.2.5 Heating method and kinetic measurement on APTES SAMs and SLG using Raman machine 42
2.2.6 DFT calculation on the theoretical Raman frequencies of APTES 43
2.3 Results and discussion **44**
2.3.1 Depth profile and interfacial analysis on APTES SAMs by using SERS 44
2.3.1.1 Characterization of APTES SAMs by AFM 44
2.3.1.2 Surface-Enhanced Raman Spectra of APTES SAMs 46
2.3.1.3 Vertical structure of internal APTES SAMs 48
2.3.1.4 Frequency shift at interfaces 50
2.3.2 Kinetic reaction of APTES SAMs and SLG observed by using SERS and Raman spectroscopy 54
2.3.2.1 In-situ kinetic anti-Stokes and Stokes Raman spectra observed on APTES SAMs. 54
2.3.2.2 In-situ kinetic anti-Stokes and Stokes Raman scattering observation on SLG 59
2.4 Summary and conclusion **64**
References **66**

CHAPTER 3: KINETIC OBSERVATION ON SEI FORMATION IN LI-ION BATTERY

3.1 Introduction **70**
3.2 Experimental section **72**
3.2.1 Samples and materials 72
3.2.2 Raman spectroscopy 72
3.2.3 SERS sensor 73

3.2.4 Cell set up for the in-situ SERS measurement and electrochemical reaction..... 74
3.2.5 Formation of SEI film 76
3.3 Results and discussion..... 77
3.3.1 Raman spectra of standard samples and frequency assignment 77
3.3.2 Formation of SEI film 79
3.3.2.1 Cyclic voltammetry 79
3.3.2.2 Stability of SEI under laser heating 80
3.3.3 Kinetic observation on SEI formation by single laser spot 81
3.3.3.1 Appropriate SERS sensor for graphite material..... 81
3.3.3.2 Kinetic SEI formation on graphite anode in Li-EC-EMC 82
3.3.3.3 Kinetic SEI formation on graphite anode in Li-PC-EMC 83
3.3.4 Kinetic observation on SEI formation in PC-based electrolyte using multi laser spots . 84
3.4 Conclusion..... 89
References 90

CHAPTER 4: DEPTH PROFILE ON SEI FILM AND THE MECHANISM OF LI_2CO_3 FORMATION IN LIB

4.1 Introduction 92
4.2 Experimental section..... 94
4.2.1 Samples and materials 94
4.2.2 Raman measurement 94
4.2.3 SERS sensor 95
4.2.4 Cell set up for the in-situ SERS measurement and electrochemical reaction..... 95
4.3 Results and discussion..... 96
4.3.1 Li_2CO_3 generation and mechanism..... 96
4.3.1.1 Detection of Li_2CO_3 products by using Au NPs SERS sensor 96
4.3.1.2 Mechanism of Li_2CO_3 formation and its relation with interfacial behavior of PC and EC at the graphite surface..... 98
4.3.1.3 Correlation of interfacial behavior and solvent molecules interaction 105
4.3.2 Depth profile on SEI formed on graphite anode, using Raman spectroscopy and SERS 110
4.4 Conclusion.....112

References **113**

CHAPTER 5: GENERAL CONCLUSION

5.1 Conclusion **118**
5.2 Perspectives **121**

LIST OF ACHIEVEMENTS

Original articles **124**
Presentations **125**

ACKNOWLEDGEMENTS

Acknowledgements **127**

Chapter 1: General introduction

1.1 Introduction of Raman spectroscopy and SERS

High-performance characterization near the surface and interface regions of materials could play a significant role in the interfacial reaction analysis. Many spectroscopic techniques have been applied to the characterization, such as Fourier transform infrared spectroscopy (FTIR), x-ray photoelectron spectroscopy (XPS) and time-of-flight secondary-ion mass spectroscopy (ToF-SIMS), and so on. Each approach has its own merit and more methods could supply more comprehensive view of a structure or a reaction.

Raman spectroscopy is capable of depth profile, in-situ kinetic measurement and temperature calculation. Combining with SERS sensor, the weak Raman scattering could be dramatically enhanced, which is usually called Surface-enhance Raman spectroscopy (SERS). SERS could distinguish the molecular information which cannot be analyzed by normal Raman spectroscopy and other methods. It is expected to provide a powerful technique to observe the subtle variation information in thin-film materials and interfaces. However, comparing with other traditional approaches, the application of SERS in interfacial analysis is quite limited, due to the confined SERS sensor.

This study attempts to demonstrate the capacity of SERS and apply it on understanding the in-situ kinetic interfacial reaction and structure of thin-film materials. The main techniques are Raman spectroscopy, SERS with several types of SERS sensors, temperature calculation from anti-Stokes and Stokes Raman scattering and depth profile measurement with a step of 0.1 nm. The in-situ analyses were completed with atomic resolution, high quality, and kinetically. In section 1.1, all the techniques employed in this study for analyzing interfacial reaction, will be introduced one by one.

1.1.1 Raman spectroscopy

Raman spectroscopy is a vibrational spectroscopy used to collect the unique chemical fingerprint information of molecules, based on the Raman scattering (*Figure 1.1*) found by Indian scientist C.V. Raman. The information of molecular vibration is beneficial for analyzing the molecular structure. The process of Raman spectroscopy work involves the inelastic scattering of monochromatic light via a sample material. Usually, a laser is irradiated on a sample for generating this light from the interacts with phonons, vibrating molecules, or other stimulations in the target samples. The majority of the scattering shows the frequency, which is the same as

the excitation source. It is called Rayleigh scattering. Minority of the scattering displays the shifted frequency that is different from the excitation source, owing to the interactions of the electromagnetic waves incidence and the vibrational energy levels of the molecules. It results in shifting the energy level of the laser photons oscillating up and down and gives the information about vibrations, called the Raman effect. A Raman spectrum is plotted with the intensity of frequency results versus shifted frequency. The frequencies position will represent each band position, corresponding to the energy levels of functional group vibrations. [1]

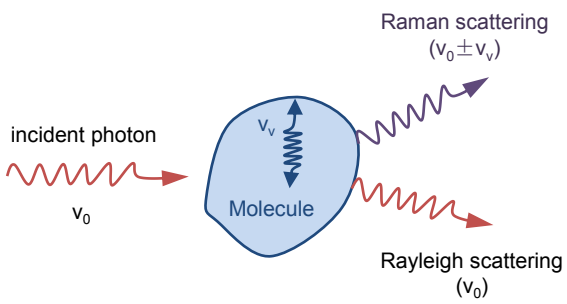

Figure 1.1 Illustration of Raman scattering

Usually, a Raman spectroscopy instrument contains the laser source, the sample and the necessary apparatus to detect the Raman spectrum as shown in *Figure 1.2*. Each part of apparatus, ND filter, objective lens, Pinhole size, grating, and so on, could influence the observed signals in various degree. For example, the objective lens with high magnification would reduce the laser power irradiated on the sample, but its large NA value allow the high spatial resolution when measuring Raman spectrum. On the contrary, objective lens with low magnification could allow larger laser power at the sample, but its low NA value is not good for the Raman mapping with high spatial resolution. Carefully adjusting all the apparatus is crucial to observe Raman spectrum with high quality.

Raman spectroscopy can detect the information of molecular vibrations, which can be used to quantitate and identify some specific functional groups or molecular bands. There are many merits of Raman spectroscopy. It allows the in-situ observation that requires little or no sample preparation; the spectra range includes wavenumber below 400 cm^{-1}, which makes it more effective than infrared spectroscopy for the detection of the variation at low frequency shift; The frequency position of each peak can be easily attributed to chemical structure; Raman spectroscopy can measure vibrations of symmetric linkages that are hardly seen via infrared

spectroscopy, and so on. So far, there are a number of new developments on Raman spectroscopy, such as SERS, resonance Raman spectroscopy, tip-enhanced Raman spectroscopy (TERS), polarized Raman spectroscopy, transmission Raman spectroscopy, spatially offset Raman spectroscopy, and hyper Raman spectroscopy. [2] SERS is the key approach in this study and will be introduced more in following section.

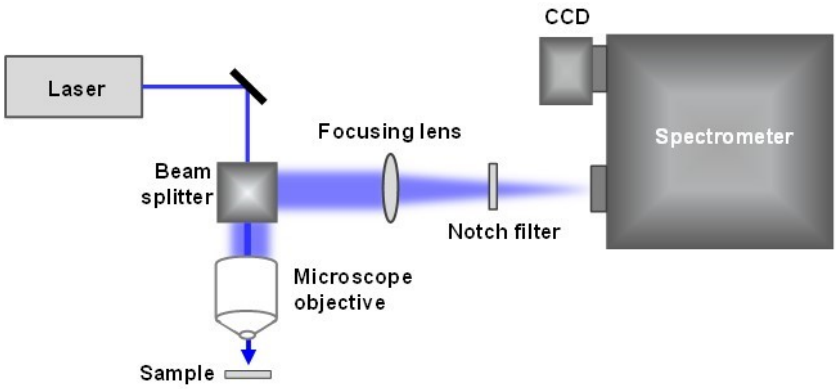

Figure 1.2 The schematic of the basic set up of a Raman spectroscopy instrumentation

1.1.2 Surface-enhanced Raman spectroscopy (SERS)

1.1.2.1 The theory of SERS

SERS, a family of Raman scattering, can be observed via the enhancement caused by rough metal nanoparticles (NPs). The development of SERS started from 1970s. Since Fleischmann et al. [3] discovered the dramatic enhancement of the Raman scattering of pyridine molecules that were adsorbed on the surface of rough Ag electrode, SERS attracted numerous attentions more and more. SERS can solve the issue of the low sensitivity when using common Raman spectroscopy. So far, the observed maximum enhancement factor can reach 10^{14} comparing with the normal Raman scattering [4]. It is beneficial to decrease the detection limit, analyze the minority of a target sample, and even achieve single molecule detection some times. It is a crucial advantage for the interfacial analysis. The enhancement mechanism of SERS was believed to be electromagnetic enhancement [5, 6] and chemical enhancement [7, 8] as shown in *Figure 1.3*.

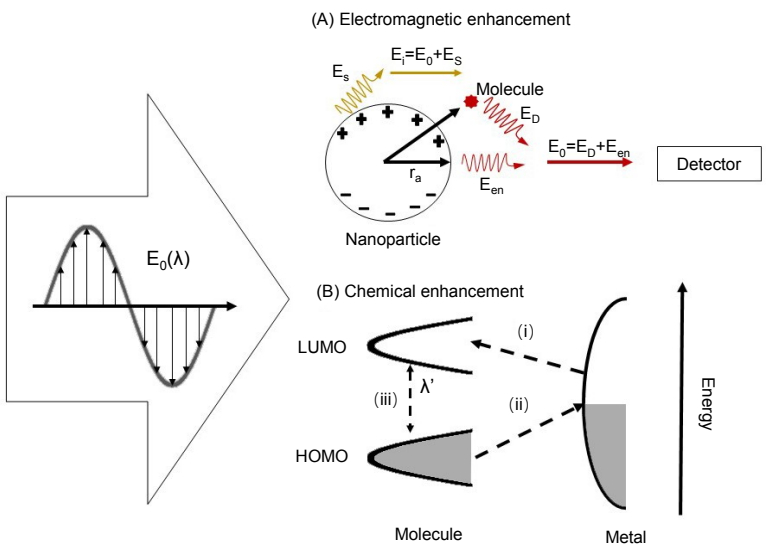

Figure 1.3 Schematic of the electromagnetic enhancement and chemical enhancement in SERS [9]

The electromagnetic mechanism (EM) enhancement is mainly owing to the excitation of localized surface plasmon resonances (LSPRs) caused by the trapped light wave at the nano-gaps

of metal NPs. The excitation of LSPR would result in high intensity surface electromagnetic field (EM enhancement) at the metal NPs surface. The molecules close to the enhanced electromagnetic field, could be excited stronger Raman scattering (SERS). EM is a distance-field effect, which may influence the range of several tens nanometer away from metal NPs surface. The enhancement factor of EM could be up to the order of 10^4 to 10^6 [10] and is considered to be the dominant mechanism of SERS. There is no special bond between adsorbed molecule and NP surface when considering EM mechanism. It cannot explain the diversity of SERS enhancement from various adsorbed molecule species, while it can explicate the SERS enhancement when target molecule is not at the very near surface of metal NPs but a little far away in tens nanometer scale.

In addition, chemical mechanism also has close relation with SERS effect and is believed to contribute the enhancement factor to the order of 10^2 [10]. The most believed model in the chemical enhancement is charge transfer (CT) mechanism. When the irradiation light is emitted on the metal surface with appropriate wavenumber, the resonance transition of electronic energy would occur between adsorbate and metal surface. It could alter the molecular polarizability of adsorbate and arouse the SERS effect. The bond between adsorbed molecule and metal surface is necessary for the CT mechanism [11]. The CT enhancement can only come about at the near-field of metal surface.

SERS enhancement is considered to be a combination of EM and CT mechanism. No matter which mechanism contribute more to the SERS effect, to create local field intensity enhancement, effective SERS sensors are crucial.

1.1.2.2 SERS sensor

For applying SERS approach in various fields, the SERS sensor with high enchantment factor, sensitivity and reproducibility plays an important role. The SERS effect can be generated from an electric enhanced field (plasmonic hotspots), which could occur at the sharp corners and/or with intra-particle gaps of metal nanostructures. In general, Au, Ag and Cu are traditional and classic materials for SERS sensor. The LSPRs of Au, Ag and Au cover wide wavelength range, where most Raman measurements occur. It results in choosing different laser wavelength for each metal NP as shown in *Figure 1.4*.

The SERS hotspots occur mainly at crevices of rough metal surface, the gaps between NPs, or sharp features of regular pattern (*Figure 1.5*). Attempting various materials and structures is beneficial for finding appropriate SERS sensor that support maximizing the SERS enhancement.

[12] Many practical potentials are still undiscovered because of the lack of appropriate SERS sensor.

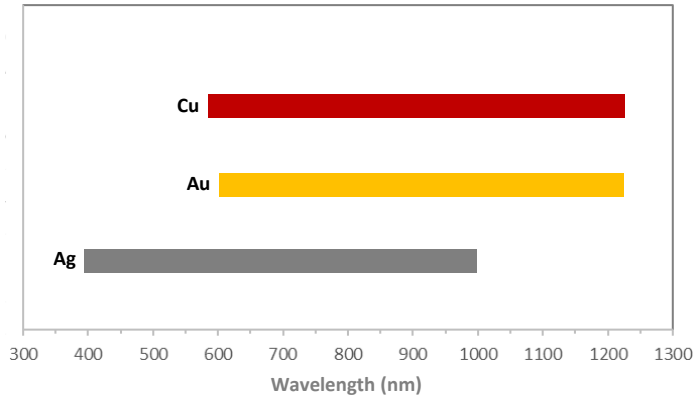

Figure 1.4 Approximate wavelength ranges for using Ag, Au, and Cu as SERS sensors [12]

Numerous efforts have been made to develop effective SERS sensor for wide application. Exploring new material, optimization the pattern of substrate and developing the structure of metal NPs result in various SERS sensors such as Shell-isolated NPs [13], polyhedral Ag mesocages [14] and SERS-active nanostructures [15], and so on. In this chapter, three types of SERS sensor that are focused on designing substrate patterns will be introduced in detail.

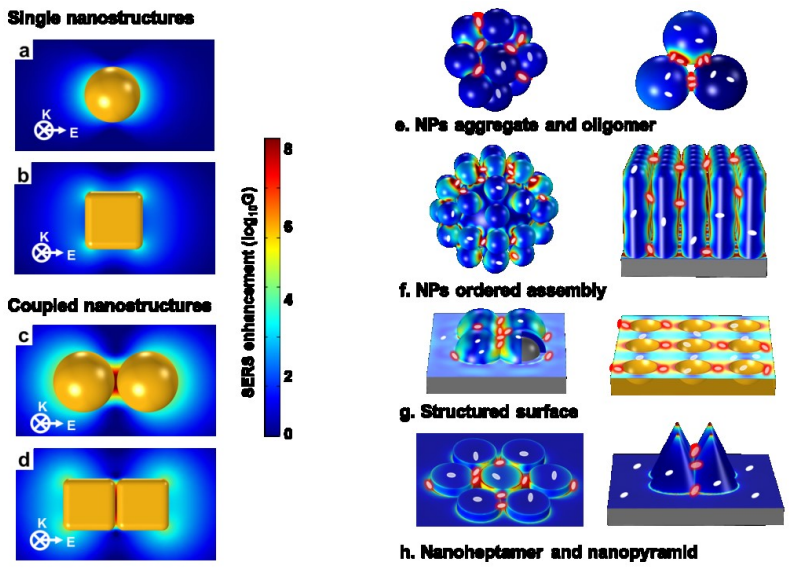

Figure 1.5 SERS Hotspots generated from metal nanostructures. Reprinted by permission from Macmillan Publishers Ltd: Nature Reviews Materials ref [16], copyright 2016

Nanoparticle film

Nanoparticle films, which are the suitable choice for SERS studies, have been producing enlightening results, for example the silver NPs. Silver NPs have been produced mainly by chemical solution processes involving the use of aggressive chemical reducing agents, capping agents, and organic solvents. *Figure 1.6* [17] includes some scanning electron microscopy (SEM) images of silver NPs film. The silver NPs films were demonstrated to offer great surface enhancement and the surface enhancement factor can be efficiently changed by the silver atom concentrations of the films. Zeng et al. [18] compare the enhancement ability of the triangular and spherical silver NPs film and found that the triangular silver NP is remarkable but somewhat lower than that of the spherical silver NP film. In this study, SERS sensors with spherical metal NPs film structure were applied to the analysis in liquid/solid interface in chapters 3 and 4.

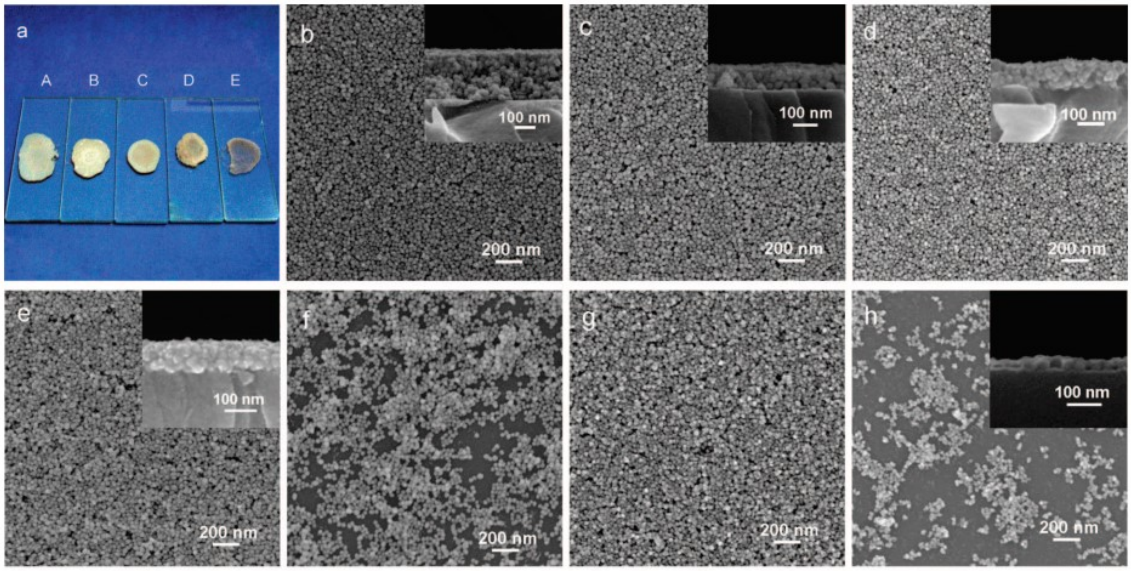

Figure 1.6 Photograph of the silver NPs films with different silver NP concentrations. Reprinted with permission from ref [17]. Copyright 2008 American Chemical Society

Nanoparticle arrays

To realize the practical applications of SERS sensor, it is important for the SERS sensors to show highly ordered, reproducible and controllable structures. A nano-patterned structure, either 3D or 2D, can provide not only significant Raman enhancement, but also high potential for application, for example, the nano-pattern in *Figure 1.7*. In the case of 2D SERS sensors, a lot of techniques are available for the pattering such as the conventional electron beam lithography,

photolithography, block copolymer lithography. Furthermore, 3D nanostructures have been demonstrated to be even higher SERS sensitivity. The 3D nanostructures have advantages of large surface area for the formation of hot spots between those closely neighbored NPs and the adsorption of target analytes. Many available 3D SERS sensors have been proposed, such as Al_2O_3 nanochanels, Si nanotips and nanowires, ZnO nanowire arrays, etc. [19] In this thesis, a SERS sensor fabricated with micro-lens array (MLA) was also tested on interfacial analysis in chapter 3.

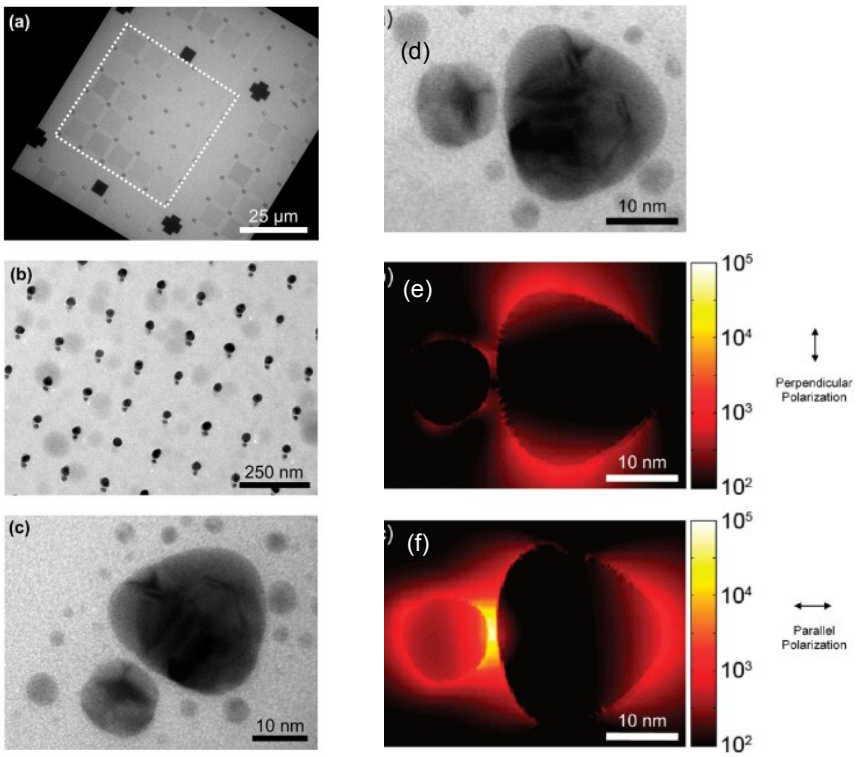

Figure 1.7 An example of Ag nanoparticle array, TEM image and FDTD simulations. Reprinted with permission from ref [20]. Copyright 2010 American Chemical Society

Core-shell Nanoparticles

Shell-isolated nanoparticle-enhanced Raman spectroscopy (SHINERS) was invented by Tian and co-workers [13], using core-shell NPs (Au@SiO_2 NPs) (morphology as shown in *Figure 1.8*). Core-shell NPs was composing from at least two nanomaterials. It is a oriented assembly that can be fabricated by cladding one nanomaterial onto another NP structure. The main virtue of SHINERS is that it is universally applicable to the sample with different surface morphology. The contamination and corrosion between SERS sensor and target sample can be avoided.

Numerous materials can be fabricated on various metal nanostructures to form the core-shell NPs, so that they can be used on diverse target samples with high sensitivity [21]. It has tremendous potential to be applied in various field, such as surface science, life sciences, food safety, and so on. Developing various ultrathin shells is crucial to the application, such as Au@SiO_2 [13], Au@Al_2O_3 [13], Au@Pt [22], Fe_2O_3@Au [23], Au@ poly (2-aminothiophenol) (PAT) NPs [21], Au@Pd [24], etc. Based on these theory and applications, the Ag NPs SERS sensor coating with a Al_2O_3 nano-film was employed in chapter 3. The Al_2O_3 nano-film was not for isolated Ag NPs from each other, but for protecting Ag NPs film the corrosion by electrolyte.

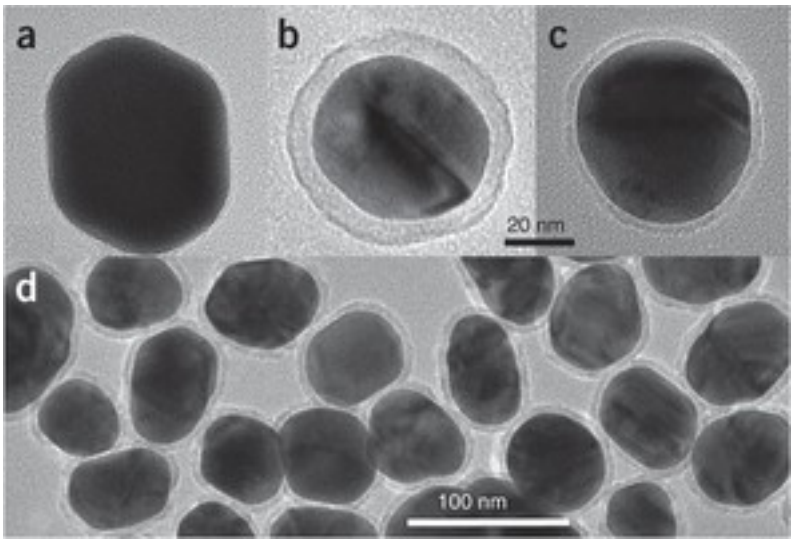

Figure 1.8 Au@SiO_2 NPs prepared under different pH conditions reported in the reference. Reprinted by permission from Macmillan Publishers Ltd: Nature Protocols ref [25], copyright 2013.

1.1.2.3 Application of SERS

SERS has great potential for providing information on slight molecular vibrations, even single molecule detection. So far, SERS has been widely employed in various fields, such as microbiology [26, 27], organic materials [28], and electrochemistry [29, 30].

Single molecule detection [4, 12, 31, 32]: The development of single molecule detection makes SERS technique attractive more and more. It demonstrates the detection resolution of SERS is rather high and SERS has vast potential for various analysis. Single molecule SERS

(SMSERS) was report by Kneipp et al [33] and Nie et al.[4] in 1997. Kneipp and co-worker studied the adsorbed crystal violet on Ag NPs colloidal solution. NaCl solution was firstly added into AgNPs colloidal solution for obtaining Ag NPs aggregation. Then, 3.3×10^{-14} mol/L of crystal violet was mixed in Ag NPs colloidal solution which mean less than one crystal violet molecule in one probe volume. The SERS enhancement was detected and the enhancement factor was calculated to be 10^{14}. The SMSERS observations in the literature concentrated on the SERS sensor of Ag NPs aggregation. Efforts are also made for realizing SMSERS on other fundamental research fields. *Figure 1.9* is a label-free sensing platform for the unambiguous detection of single-stranded DNA using SERS reported by Braun et al. The probe-tethered Ag NPs were assembled on Ag film via the agency of the target DNA strand, resulting in creating an intense EM hot spot.

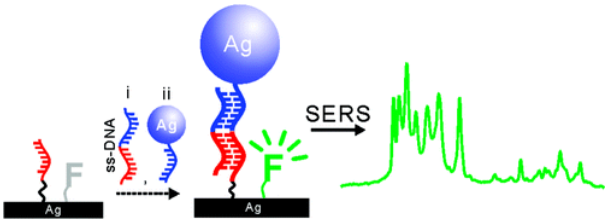

Figure 1.9 Detection of single-stranded DNA by using SERS. Reprinted with permission from ref [34]. Copyright 2007 American Chemical Society

Application in detection on various samples: some reports describe the detection on Polymer material [35-37] by using SERS, such as, the self-assembled monolayers (SAMs) adsorbed on SERS-inactive metal surfaces which show strong SERS enhancement or deposit polymer samples on rough SERS substrate to obtain enhance Raman scattering. Besides, SERS is also widely studied in biological application [38, 39], which allows the investigation of biological samples under in-situ or minimally invasive conditions. Moreover, in the field of electrochemistry, for instance, SERS can support the analysis on characterization and reaction mechanism of electrodeposition process [40, 41].

However, the application of SERS in the study of interfacial analysis and Li-ion battery (LIB) is not as mature as other traditional approaches. *Figure 1.10* (a) is the publication item each year about the interfacial analysis with SERS, comparing the traditional approaches XRD, XPS, FTIR and Raman spectroscopy. As a result, SERS is not widely used as much as other traditional methods. Besides, in the field of LIB, as the collected data in *Figure 1.10* (b), although Raman

spectroscopy was employed many in the analysis of LIB, the report about using SERS on studying LIB related research is nothing much.

SERS, as a member of Raman spectroscopy, can not only elevate the sensitivity of Raman scattering, but also be capable of time-resolved measurement and depth profiling. The narrow application of SERS in LIB and interfacial analysis maybe affected by the confined SERS sensor. With appropriate SERS sensor, SERS could be expected to show more application and ability in the analysis of interfacial reaction.

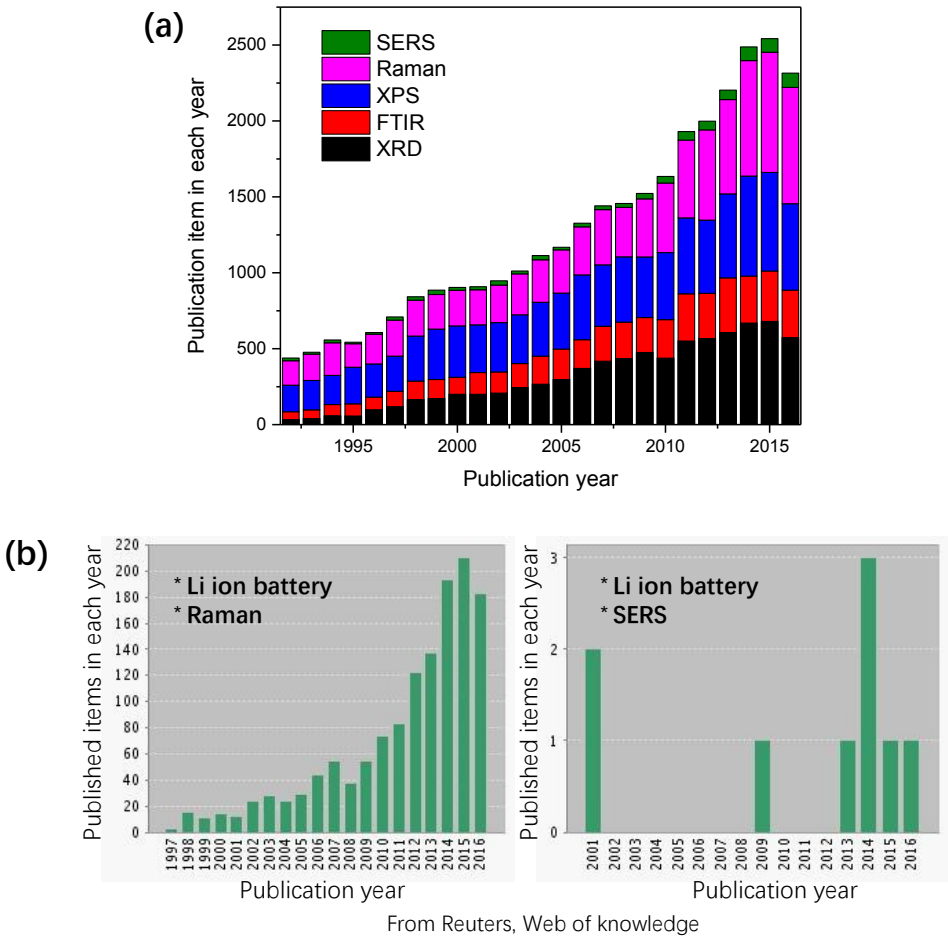

Figure 1.10 (a) Published items each year about the interfacial analysis with the methods of XRD, FTIR, XPS, Raman and SERS, from Thomson Reuters' Web of Knowledge, Web of Science (as of 5th Nov. 2016); (b) Published items each year containing the search topic term "Li ion battery & Raman" (left) and "Li ion battery & SERS", from Thomson Reuters' Web of Knowledge, Web of Science (as of 5th Nov. 2016)

1.1.3 Time-resolved measurement

1.1.3.1 Observation on kinetic reaction

To support the analysis of kinetic reaction at interfaces, real-time observation is significant to the accurate monitoring. Time-resolved techniques allow the analysis on kinetic reaction and structure variation, such as chemical reaction process, melting process, crystallizing kinetics, surface dynamics and many more. Electron microscopy methods and electron diffraction techniques are sensitive to the morphology and nuclear positions within the molecule [42]. Thus, for the time-resolved observation, ultrafast electron microscopy [43, 44] and electro diffraction [45-47] are usually used to directly probe the transient positions of atoms inside a molecule. Different from them, spectroscopic methods can provide more direct access to the molecular energy spectrum, such as Raman spectroscopy. Raman spectroscopy has been well proven as an approach for analyzing molecular structure, molecular chemistry, and intermediates in solution. It is of great advantageous comparing to some time-resolved absorption and emission spectroscopy.

To the present, the time-resolved measurement using Raman spectroscopy is mature and widely applied [48-52]. Taking the *Figure 1.11* as an example, Fontané et al. [48] demonstrated that the secondary phases of ZnS in $Cu_2ZnSnSe_4$ layers during the sputtering process, which cannot be distinguished by XRD based techniques could be detected kinetically by using Raman spectroscopy. Meanwhile, along with sputter time, the in-depth structure of layers could be monitored, which mean the in-depth resolved measurement was realized. It also illustrates that time-resolved Raman spectroscopy can support various observation combining with other devices and techniques. The development of time-resolved observation using Raman could be much improved by the advent of highly efficient spectrometers, pulsed tunable lasers, and highly sensitive multichannel detectors [53]. The generation of ultrashort pulses is a revolutionary development, which can reduce the optical pulse widths to sub-picosecond [54]. For the Raman spectroscopy in our group, the minimum exposure time could be 0.002 s by installing pulse laser shutter on Raman spectroscopy, so that the kinetic monitoring is available in microsecond scale. In addition, the emergence of SERS highly improves the spectrum quality, which makes the time-resolved observation on structure variation more accurate.

In this study, the time-resolved measurements were carried out for monitoring the phase transition process of (3-aminopropyl)triethoxysilane derived self-assembled monolayers (APTES

SAMs), the thermal stability of single layer graphene (SLG) and the kinetic formation of the passivation film at the solid-electrolyte interface (SEI film) in LIB. To observing the weak Raman scattering of APTES SAMs and SEI films, the SERS sensors were used for enhancing Raman signals. Besides, in order to monitor the phase transition of APTES SAMs and thermal stability of SLG, another function of Raman spectroscopy, temperature calculation by using anti-stokes and stokes Raman scattering, will be conducted and analyzed together with time-resolved measurement. The details of temperature estimation will be introduced in the following section 1.1.3.2.

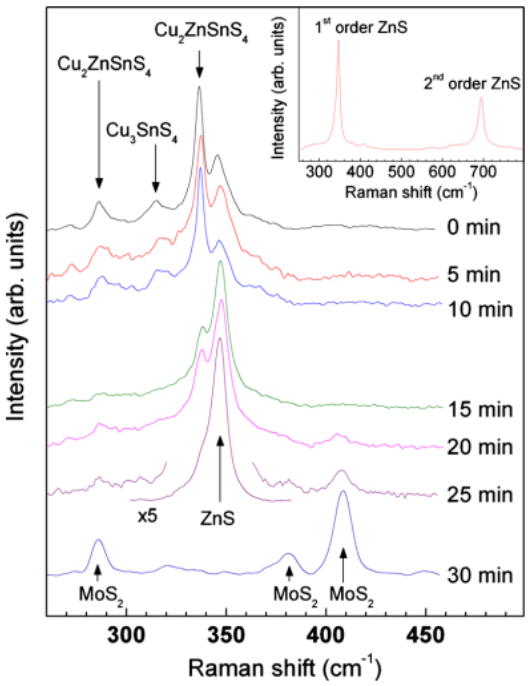

Figure 1.11 A Raman spectra measured on $Cu_2ZnSnSe_4$ layers at different sputter time using a 325 nm excitation wavelength: The sputter process was characterized by the presence of a peak at about 700 cm^{-1}, corresponding to the second order band of ZnS, in addition to the main first order ZnS mode at 350 cm^{-1}. Reprinted from ref [48], with the permission of AIP Publishing

1.1.3.2 Kinetic temperature calculation

During the observation on kinetic reaction, if the anti-Stokes Raman scattering is detectable, the temperature of material can be monitored from the Raman frequency, and the ratio of the intensities of the anti-Stokes and Stokes Raman signals (the Ias/Is ratio) [55-57]. Anti-Stokes and Stokes Raman scattering are two possible outcomes of the Raman interaction. The material absorbs energy and emits photon with higher or lower energy than the absorbed photon. These

two possibilities are called anti-Stokes Raman scattering and Stokes Raman scattering, respectively. (*Figure 1.12*)

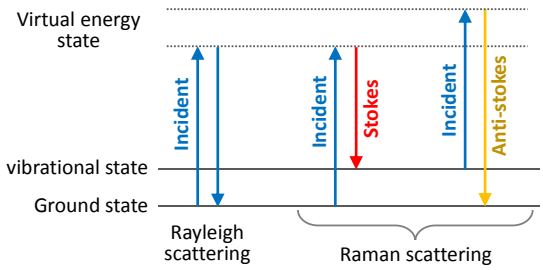

Figure 1.12 Energy level diagram of Raman scattering

Stokes scattering peaks are stronger than anti-Stokes scattering peaks, and their ratio depends on the temperature. This fact can be exploited practically for the temperature measurement. [58, 59] The intensity ratio of anti-Stokes to Stokes scattering is theoretically expressed as

$$Ias/Is = \exp(-h\nu/kT) \qquad \text{eq (1)}$$

where ν is the Raman shift of one vibration, k is the Boltzmann constant, and h is the Planck constant. With recording a series ratio of Ias/Is during a kinetic observation, the kinetic temperature (T) variation can be calculated accordingly.

The anti-Stokes Raman scattering is of high potential to become a powerful technique for the in-situ temperature investigations. For example, the extension of Raman scattering from materials above the temperatures of 1000 °C is a crucial challenge, yet the structural and chemical variation of industrial materials usually occur in this temperature range [60]. In the case of this tough situation, this method is useful for high temperature measurement. Besides, for the observation in low temperature range, this method was also effectively applied. For instance, Tsuji et al. [61] observed the Stokes and anti-Stokes Raman scattering from organic light-emitting diodes based on copper phthalocyanine (CuPc), α-NPD, and Alq_3 with excitation at 633 nm and demonstrated the temperature of the CuPc layer operated at 400 mA should be 140 ºC.

The temperature calculation in this thesis were carried out for kinetic temperature observation at the range from room temperature to 600 ºC. These studies will be explained in chapter 2.

1.1.4 Depth profile measurement

Except for the time-resolved measurement, another supporting technique for this study is the depth profile measurement. The most common depth profiling approaches include destructive method and non-destructive method, such as microtome method, TOF-SIMS, attenuated total reflection (ATR) FTIR, angle resolved XPS (ARXPS), and so on. The depth resolution appears to be from nanometer scale to micrometer. The Raman laser can penetrate sample surface from depth of tens of micrometers with a depth resolution of around 1~2 μm. Many applications [62-64] demonstrate that confocal Raman spectroscopy is suitable to depth profile, but only realized in micrometer scale. Efforts can be made on improve the depth profile resolution, such as objective lens with high Numerical Aperture and effective SERS sensors.

Previous achievement in depth profile of our group

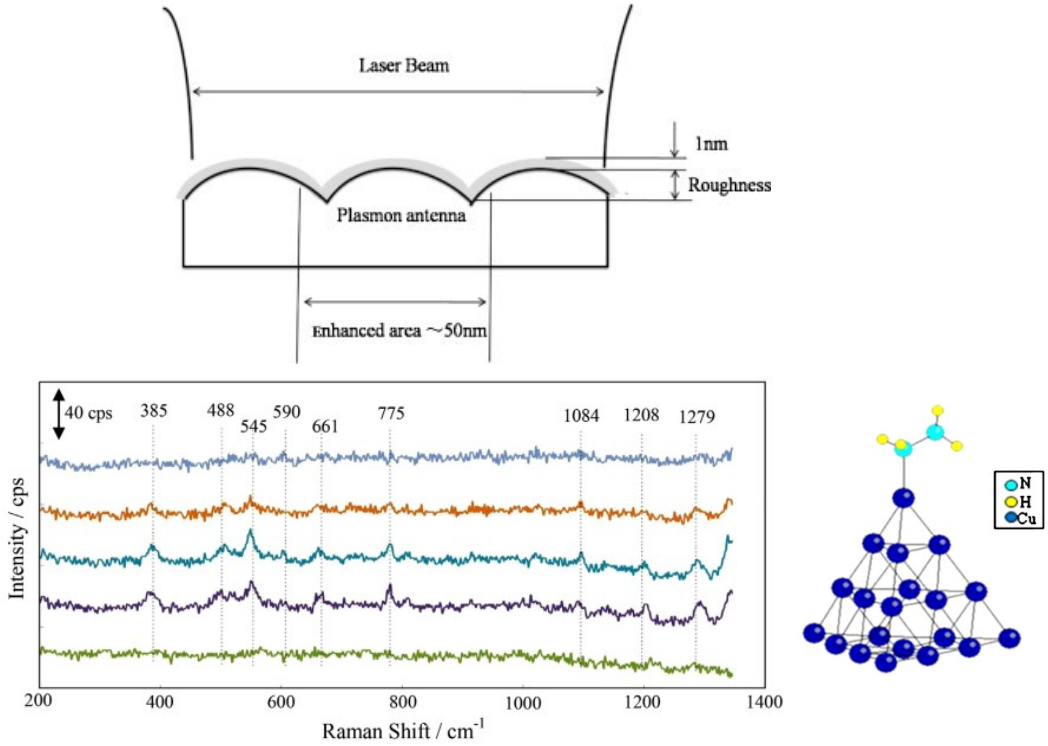

Figure 1.13 Left: Raman spectrum of hydrazine on the Cu antenna SERS sensor with depth step of 1 nm between each spectrum; Right: The prospective configuration of hydrazine on Cu (gauche-conformation). Reprinted from ref [65], Copyright 2013, with permission from Elsevier

In our group, there are efforts of developing SERS sensors have been made to improve the depth profile resolution by using Raman spectroscopy. Various SERS sensors are designed and applied in the analysis of liquid/solid interface and solid/solid interface, so that the resolution and intensity of the electric field could be both enhanced by SERS sensor. Moreover, to support the accurate vertical movement of Raman laser, a piezo field gradient stage is installed to control the depth displacement with the minimum step of 0.05 nm. Based on these developments, the depth profiling has been achieved to nanometer level. For instance, Jiang et al. [65] developed a SERS sensor with a plasmon antenna structure and applied the SERS sensor in characterizing the hydrazine adsorption on Cu surface with a depth resolution of nanometer as shown in *Figure 1.13*.

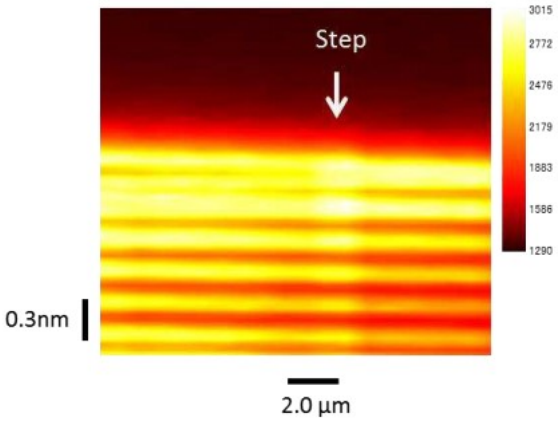

Figure 1.14 Raman depth image of G-band intensity for HOPG layers [66]

Furthermore, Yanagisawa et al. [66] developed a plasmonic SERS sensor and applied the SERS sensor to the structure analysis in Highly Ordered Pyrolytic Graphite (HOPG) interlayer and the Diamond-like carbon (DLC)/Si interface. The depth image of G-band intensity of HOPG in *Figure 1.14* showed good agreement with the layer distance, 0.335 nm, which demonstrate the depth profile resolution of sub-nanometer.

In the chapters 2 and 4, several SERS sensors are also applied in characterizing the internal structure and the interfacial structure of the nano-film samples, APTES SAMs and SEI film in LIB.

1.2 Introduction of three target samples

The techniques introduced in the section 1.1 are employed in analyzing the in-situ kinetic interfacial reaction of three Nano-film structures, which are organic film of (3-aminopropyl) triethoxysilane derived self-assembled monolayers (APTES SAMs), inorganic film of single-layer Graphene (SLG), and the passivation film at the solid-electrolyte interface (SEI film) in Li-ion batteries (LIB) consisting of both organic and inorganic components. Amongst them, APTES SAMs and SLG with known structures were used for evaluating the ability of SERS in the interfacial analysis. The SEI film in LIB is for applying SERS to observe the unknown structure. These three samples will be introduced one by one in following sections.

1.2.1 APTES SAMs

APTES is a typical organosilane agent for the preparation of amino-terminated films, which can be used for promoting adhesion of polymer films on substrate, promoting protein adhesion and cell growth, attaching metal NPs to a silica substrate, and so on. APTES moieties are attached through the formation of Si-O-Si bond between the silanol groups and substrate surface. APTES has been widely used because its amino terminal group [67, 68] and is attractive for DNA microarrays [69], protein arrays [70], and many more.

The surface functionalization of SiO_2 substrates could be accomplished by the self-assembly process of the APTES monolayer. The bond formation between the SiO_2 substrate surface and the APTES moieties generated from the first step of hydrolysis of the ethoxy ($–C_2H_5$) groups, which result in the formation of silanols (Si–O–H). The followed second step lead to the covalent adsorption of the hydroxysilane product. Thereby, a self-assembled monolayer of APTES moieties would be formed, which is constructed by the siloxane (Si–O–Si) network. As can be seen in the structure of APTES SAMs in *Figure 1.15*, the APTES moieties are oriented in a way that the positively charged amine groups ($–NH_2^+$) are aligned away from the underlying silicon substrate. [70, 71]

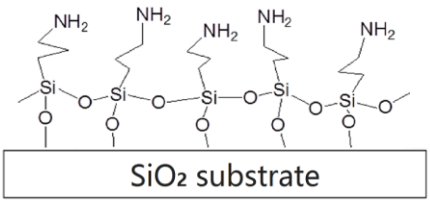

Figure 1.15 An ideal APTES SAM layer with high orientation array

In actual preparation, the APTES moieties have been demonstrated to be not as complete order as the ideal structure in *Figure 1.15*. Zhu et al. [72] discussed the possible irregular structure of APTES-derived layer. Upon the lowest layer, there might be almost no APTES moieties orientated vertically and regularly. As displayed in *Figure 1.16*, there might be inter- and intramolecular catalyze silane attachment and oligomers and polymers of silanes exist in the interior APTES layer. Some typical structures would be the physisorbed, hydrogen-bonded silane molecules (a) or electrostatically attached silane molecules (b), which are not stable. Besides, some molecules only react with surface silanol groups (c) and some are bonded with neighborhood molecules horizontally (d) and/or vertically (e). Moreover, some attach to the surface and form oligomeric (f), leading to the disorder layer.

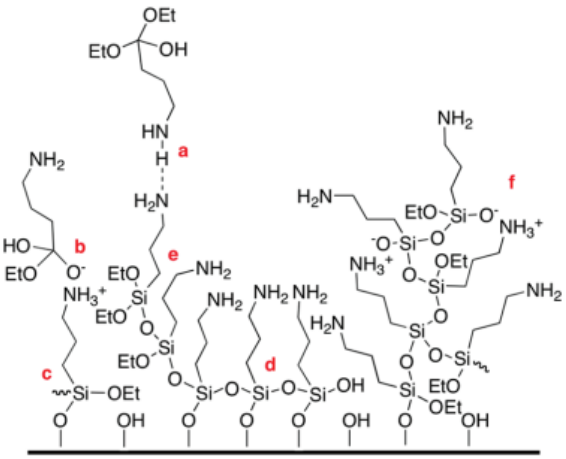

Figure 1.16 An APTES-derived layer with structural irregularities refer to the research of Zhu et al. Reprinted with permission from ref [72], Copyright 2012 American Chemical Society.

APTES SAMs has been investigated by many methods, including ellipsometry [73], UV–visible absorption [74] and X-ray photoelectron spectroscopy [75]. The structure at the interface and within the APTES SAMs is partial understood till present. Nevertheless, none of them could

support the accurate inner structure of APTES SAMs in detail. In chapter 2, the phase transition process and depth profile on APTES SAMs will be demonstrated by using SERS, to demonstrate the advantage of SERS and explore the unknown properties of APTES SAMs simultaneously.

1.2.2 Single layer Graphene (SLG)

As a crystalline allotrope of carbon with 2-dimensional system (*Figure 1.17*), the honeycomb lattice of graphene has given occasion to many interesting properties and potential to be used in Lithium batteries, solar cells, semi-conductor, etc. Graphene has many extraordinary properties: large theoretical specific surface area (2630 m^2g^{-1}); high thermal conductivity (5000 $Wm^{-1}K^{-1}$), intrinsic mobility (200 000 cm^2 v^{-1} s^{-1}), optical transmittance (97.7%) and good electrical conductivity. [76] Raman spectroscopy has been a useful tool to study graphene, including identifying edge orientation, thermal conductivity, doping concentration, structural properties, and so on.

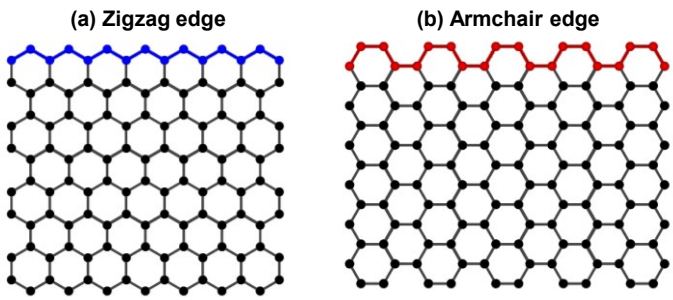

Figure 1.17 Structure of single layer graphene: (a) Zigzag edge; (b) Armchair edge

The defects in graphene can be induced by plasma treatment [77], electron beam irradiation [78], and so forth. It was reported that the nature of defects could be probed with the intensity of the D peak, since the breathing modes of sp^2 atoms originated from defects. Many studies [79-81] have quantified the number of point defects in SLG using the intensity ratios of the D and G peaks, I(D)/I(G). In addition, a decrease in the I(2D)/I(G) ratio can be an indicator of the increase in doping levels in graphene. In chapter 2, thermal stability and defect generation induced by confocal laser heating will be investigated by using Raman spectroscopy.

1.2.3 SEI film in Li-ion battery

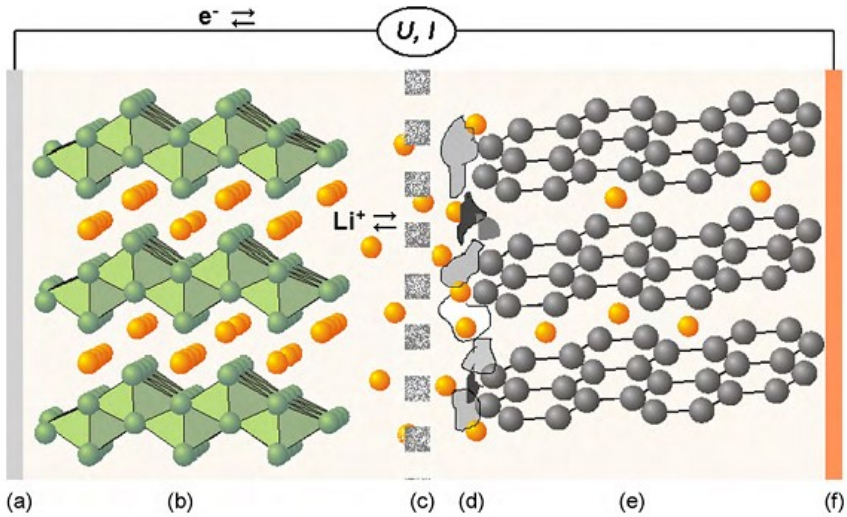

(a) aluminum current collector; (b) oxide active material; (c) porous separator soaked with liquid electrolyte; (d) inhomogeneous SEI film; (e) graphite active material and (f) copper current collector.

Figure 1.18 Schemetic of a typical Li-ion battery. Reprinted from ref [82], Copyright 2010, with permission from Elsevier.

Since Li-ion battery (LIB) was developed and applied in commercial device twenty years ago, it became indispensable in daily life. The merits of LIB are high energy density and slow loss of charge when not in use. However, it still has bottleneck problem and disadvantage, such as capacity, charging rate, energy density, cycle life, self-discharge and even safety issue. Most of these performances, no matter advantages or shortages, were partly dominated by the passivation layers formed at the solid-electrolyte interphase (SEI film). *Figure 1.18* is a schematic illustration of a typical LIB. Deeply understanding the reaction mechanism in LIB is significant to improve the performance of LIB. SEI film is considered as the most important but least understood component in LIB. It is significant because they are essentially responsible for the reversibility of Li^+-intercalation while cycling LIB. But it is difficult to characterize since its sensitive chemical nature, elusive manner of formation, and the lack of reliable in-situ characterization tools [83].

1.2.3.1 Basic theory in Li-ion battery

LIB is also called the “rocking chair” battery, because during the charging and discharging cycling, the participants in the electrochemical reactions are two electrodes with electrolyte for the Li^+ move in and out between cathode and anode. By far, the widely used active material in

anode is graphitic material. Besides, there are also plenty of other kinds of carbonaceous materials can been used. The most common used active material in cathode includes $LiCoO_2$, $LiMn_2O_4$, and $LiFePO_4$, and so forth. The electrolyte in LIB usually consists of Li salt ($LiPF_6$, $LiClO_4$, $LiBF_4$, and so on) and organic solvent (cyclic carbonate and acyclic carbonate). When a LIB is under charging cycle, the Li^+ ion moves from the cathode (lithium related compounds) and intercalates into the anode (usually C_6). When the cell is discharging, the deintercalation of Li^+ ion from anode to cathode occurs. When electrons flow through a closed cycling of charging and discharging, the reaction on two electrodes could be summarized as following reaction eq (2) and (3) [84]. The equations show the chemistry, taking $LiCoO_2$ as example.

The cathode half-reaction is:

$$Li_{1-x}CoO_2 + xLi^+ + xe^- \rightleftarrows LiCoO_2 \qquad \text{eq (2)}$$

The anode half-reaction is:

$$xLiC_6 \rightleftarrows xLi^+ + xe^- + xC_6 \qquad \text{eq (3)}$$

1.2.3.2 Chemistry of SEI film in Li-ion battery

During the first charging cycle in LIB the electrolyte undergoes reduction at the surface of graphite anode resulting in a passivation layer, named SEI film. An effective SEI film can prevents further electrolyte decomposition by insulating the electron transport passing through, while Li^+ ion is allowed to pass through the SEI film during cycling. SEI film is believed to comprise of inorganic and organic products, which are partial or complete reduced from the electrolyte components. The onset potential of the electrolyte reduction is not a fixed value. Plenty of literatures offer different values, but 0.8~1.0 V is the most widely adopted range [85]. Li-ion intercalation to disordered carbons may begin from 1.5 V and to ordered carbons begins at 0.25 V [86]. The thickness of the SEI film measured by various methods, vary from few Å to hundreds of Å [82].

1.2.3.3 Controversies in SEI film

Significant advances have been made till present as a variety of new methods and tools were developed. However, debates still persist on many issues, even the basic component of SEI film. Some of the main debates are discussed as follows.

Reaction mechanism of organic products−semicarbonates

According to many experimental methods and calculation results, the semi-carbonates would be generated as reduction products of carbonate electrolyte solvents via a single-electron reduction pathway. The possible reduction formula could be generally summarized from two perspectives: alkyl-oxygen cleavage (eq(4)) and acyl-oxygen cleavage (eq(5)), which may influence the gaseous products and semi-carbonates. Eqs (4) and (5) are the possible formulas that were re-organized by Xu [85], according to the two original paper [87, 88]. The alkyl-oxygen cleavage pathway was firstly proposed by Aurbach and co-workers [89]. As shown in Eq (4), it assums that nucleophilic attacks occur between two radical anions generated by initial electronation of the carbonate molecules [85, 87]. Along with the reduction process, a gaseous product, alkene, was formed as well. While Shkrob et al. claimed that the cyclic radicals were never observed according their research [85, 88], instead, a ring-opening reaction was proposed as eq (5), the acyl-oxygen cleavage. This alternative pathway involved carbonate radical anion and generate the different gaseous products from eq (4). Onuki et al. [90] believed that eq 4) and (5) coexisted in the reaction, which could explained the coexistence of alkoxides with semicarbonates and oxalates they detected.

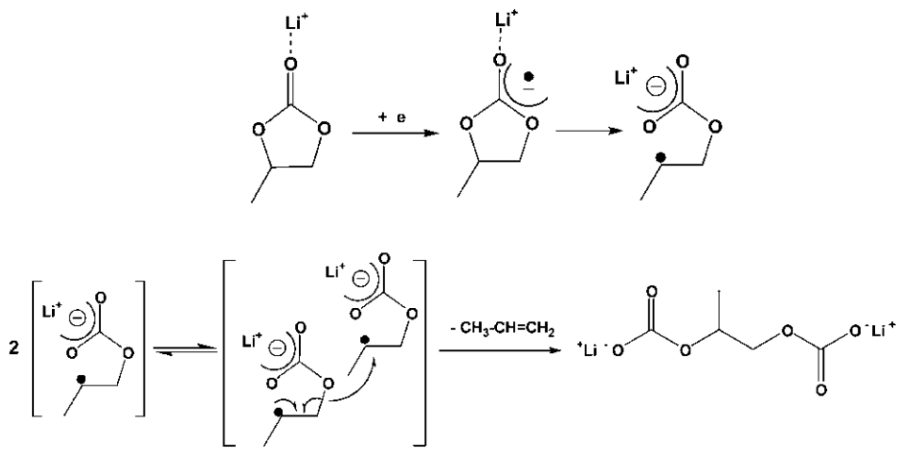

eq (4) [91, 92]

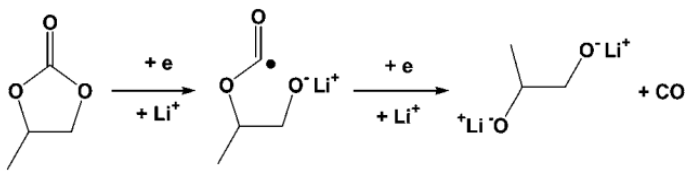

eq (5) [90, 91]

Presence of inorganic products−Li_2CO_3

When Aurbach and co-workers estimated the semi-carbonates as the main components of SEI film via the single-electron pathway as eq (4), the Li_2CO_3 was considered as an artificial product due to the poor moisture management, which could be understood as the Li_2CO_3 should not exist as a reduction product under the well moisture management. This was supported by many researches [93-99]. However, numerous researchers still described Li_2CO_3 as an SEI film component according to their research [100-109]. These researches report that the Li_2CO_3 could be observed on either first cycling graphite, or aged graphite surface, and consider the Li_2CO_3 product as one of the main components. The role of Li_2CO_3 in SEI film was reported in many ways, the component to constitute the innermost layer of SEI film [97, 110], the media for the Li^+ ion transportation [111, 112], and so on. The reaction mechanism of Li_2CO_3 formation is mostly believed to be a two-electron reduction pathway of electrolyte solvent, as shown in eq (6). In chapters 3 and 4, the formation and mechanism of the Li_2CO_3 product will be discussed by using SERS and Raman spectroscopy.

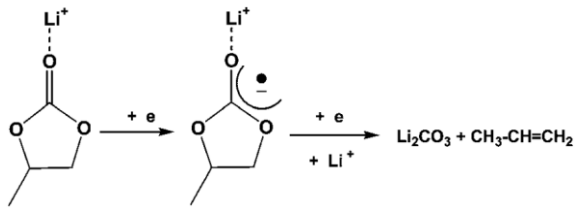

eq (6) [91, 113]

Interior structure of SEI film

In the first papers about the SEI film [114], its interior structure was suggested to consists of one or two layers. The innermost layer maybe a thin and compact film, and the outer layer maybe a porous layer. At present, it is well known that the SEI film on graphitic electrodes may consists of many components including LiF, Li_2CO_3, $LiCO_2$-R, Li_2O, lithium alkoxides, semi-carbonates, nonconductive polymers and more [82]. Peled et al. [115], Aurbach et al. [116], and Edström et al. [97] proposed that the SEI film should be a dense layer of inorganic components (LiF, Li_2CO_3, etc.) close to the carbon (innermost layer), and a porous polymeric organic layer (semi-carbonates etc.) close to the electrolyte (outer layer) as shown in *Figure 1.19* (a) (b). However, there were studies [99, 101] revealed new insights by using combined TEM and multinuclei NMR. It was suggested that SEI film may actually rather simple, comprising of semi-carbonates and LiF as shown in *Figure 1.19* (c). These studies strongly indicated that the layered structure of the SEI

film might not exist, at least not under the conditions they employed. The core debate seems to be the alignment of inorganic and organic components in SEI film, which will also be discussed in chapter 4.

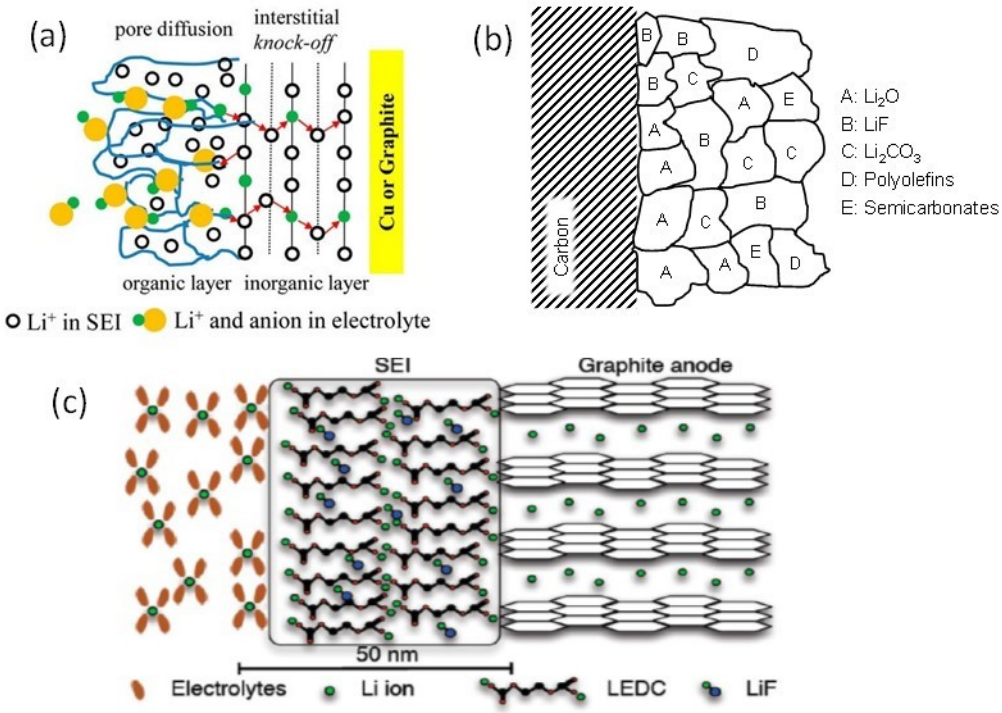

Figure 1.19 The schematics proposed by many literatures. Image (a) describes the two layers' structure, including organic layer at the outer layer and inorganic layer at the innermost layer of SEI film, reprinted with permission from ref [110]. Copyright 2012 American Chemical Society. Image (b) illustrates the multi-layer structure with various inorganic composition inside SEI film and organic composition at outer layer, proposed in the reference [115]. Image (c) estimate the SEI film with no separate inorganic and organic layer structure, with LiF as main inorganic component, reprinted with permission from ref [99]. Copyright 2013 American Chemical Society.

1.2.3.4 Characterization techniques

Many techniques have been employed to analyze the SEI film, including SEM, FTIR, XPS, TOF-SIMS, and so forth, many of which have been reviewed by Balbuena et al. [117] and Verma et al. [82]. FTIR could be used to identify electrolyte reduction products. XPS can identify surface deterioration as well decomposition compounds. Microscopies approaches allow the visualized

morphology of SEI film surface and cross section. TOF-SIMS can support the depth profile analysis of internal SEI film.

As introduced in section 1.1, SERS and Raman spectroscopy are expected to show well performance on the interfacial analysis in LIB, because of the merits of in-situ measurement, the kinetic monitoring, the depth profiling characterization and observing the molecular vibration. Publication items in each year of the studies on SEI film in LIB is displayed in *Figure 1.20* (left), which illustrate the dramatic increase in the studies on SEI film since 2011, especially the publication over 200 these three years. While among the research on SEI film, the study using Raman spectroscopy is rather few, despite the publication number is increasing. The SERS employed in SEI film would be even more rare, after all the SERS study on LIB is quite few (see the report in *Figure 1.10*). The limit application of SERS in the analysis of SEI film is affected by the confined SERS sensor. With effective SERS sensor, SERS could be expected to advance a deeper understanding of SEI film from many aspects.

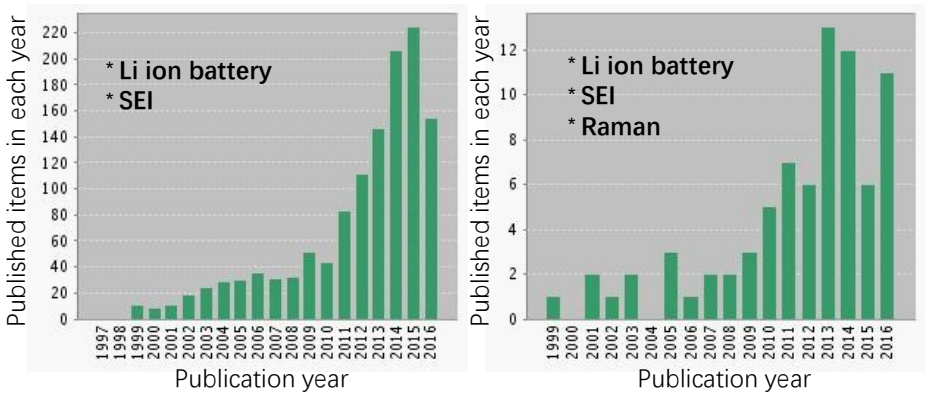

From Reuters, Web of knowledge

Figure 1.20 Published items in each year containing the search topic term "Li ion battery & SEI" (left) and "Li ion battery & SEI & Raman", from Thomson Reuters' Web of Knowledge, Web of Science (as of 5th Nov. 2016)

1.3 Strategy of this research

In this study, Raman spectroscopy and SERS were employed in the interfacial analysis on nano-film structures and kinetic variations. The studies were carried out in two parts: a demonstration and an application. *Demonstration*: time-resolved measurement and depth profiling measurement were conducted on two samples, APTES SAMs and SLG with well-known structure, so that the capability of SERS in analyzing Nano-film can be verified to be effective and also improved to a certain extent. *Application*: time-resolved measurement and depth profile were also realized on SEI film in LIB to explore the unknown reaction and mechanism.

For the demonstration of time-resolved measurement on the organic Nano-film APTES SAMs, the anti-stokes and stokes Raman spectroscopy and the real-time temperature calculation by using Ag NPs SERS sensor were conducted at temperature range lower than 120 ºC. For the kinetic investigation on inorganic Nano-film SLG, the temperature was calculated at the temperature range from 200 ºC to 600 ºC. Besides, the depth profile was realized on APTES SAMs in atomic level, by using SERS and a piezo field stage controller. The depth resolution was already explained and demonstrated to be 0.1 nm in section 1.1.4. It was also applied in the internal structure and interfacial junction of APTES SAMs with a step of 0.05 nm.

The application of SERS in SEI film was carried out with time-resolved measurement and depth profile, the same as the analysis in demonstration part. For the time-resolved measurement on SEI film, Ag NPs transmission sensor with Al_2O_3 coating was placed on graphite surface for observing SERS spectra. The SERS spectra were kinetically recorded to monitor the kinetic reaction at the graphite surface during the SEI film formation in the first charging cycle. For investigating the mechanism of Li_2CO_3 formation, depth profile in micrometer scale was applied in the interface of electrolyte solvent and graphite. For the depth profile of SEI film in LIB, Au NPs transmission sensor was used on SEI film to observe the SERS spectra.

References

[1] G. Keresztury, Raman Spectroscopy: Theory, in: Handbook of Vibrational Spectroscopy, John Wiley & Sons, Ltd, 2006.

[2] Raman spectroscopy. https://en.wikipedia.org/wiki/Raman_spectroscopy, Wikipedia, Retrieved on 30th Octorber 2016.

[3] M. Fleischmann, P.J. Hendra, A.J. McQuillan, Chemical Physics Letters, 26 (1974) 163-166.

[4] S. Nie, S.R. Emory, science, 275 (1997) 1102-1106.

[5] D.L. Jeanmaire, R.P. Van Duyne, Journal of Electroanalytical Chemistry and Interfacial Electrochemistry, 84 (1977) 1-20.

[6] C. Fang, G. Wu, Journal of Molecular Structure, 938 (2009) 336-340.

[7] M.G. Albrecht, J.A. Creighton, Journal of the American Chemical Society, 99 (1977) 5215-5217.

[8] Q. Zhou, X. Li, Q. Fan, X. Zhang, J. Zheng, Angewandte Chemie International Edition, 45 (2006) 3970-3973.

[9] S. Siddhanta, C. Narayana, Nanomaterials and Nanotechnology, 2 (2012) 2-1.

[10] A. Campion, J.E. Ivanecky, C.M. Child, M. Foster, Journal of the American Chemical Society, 117 (1995) 11807-11808.

[11] L. Yang, X. Jiang, W. Ruan, B. Zhao, W. Xu, J.R. Lombardi, The Journal of Physical Chemistry C, 112 (2008) 20095-20098.

[12] B. Sharma, R.R. Frontiera, A.-I. Henry, E. Ringe, R.P. Van Duyne, Materials Today, 15 (2012) 16-25.

[13] J.F. Li, Y.F. Huang, Y. Ding, Z.L. Yang, S.B. Li, X.S. Zhou, F.R. Fan, W. Zhang, Z.Y. Zhou, Y. WuDe, B. Ren, Z.L. Wang, Z.Q. Tian, Nature, 464 (2010) 392-395.

[14] J. Fang, S. Liu, Z. Li, Biomaterials, 32 (2011) 4877-4884.

[15] T. Vo-Dinh, TrAC Trends in Analytical Chemistry, 17 (1998) 557-582.

[16] S.-Y. Ding, J. Yi, J.-F. Li, B. Ren, D.-Y. Wu, R. Panneerselvam, Z.-Q. Tian, Nature Reviews Materials, 1 (2016) 16021.

[17] B. Hu, S.-B. Wang, K. Wang, M. Zhang, S.-H. Yu, The Journal of Physical Chemistry C, 112 (2008) 11169-11174.

[18] J. Zeng, H. Jia, J. An, X. Han, W. Xu, B. Zhao, Y. Ozaki, Journal of Raman Spectroscopy, 39 (2008) 1673-1678.

[19] C. Cheng, B. Yan, S.M. Wong, X. Li, W. Zhou, T. Yu, Z. Shen, H. Yu, H.J. Fan, ACS Applied Materials & Interfaces, 2 (2010) 1824-1828.

[20] J. Theiss, P. Pavaskar, P.M. Echternach, R.E. Muller, S.B. Cronin, Nano Letters, 10 (2010) 2749-2754.

[21] K. Qian, H. Liu, L. Yang, J. Liu, Analyst, 137 (2012) 4644-4646.

[22] L. Lu, G. Sun, H. Zhang, H. Wang, S. Xi, J. Hu, Z. Tian, R. Chen, Journal of Materials Chemistry, 14 (2004) 1005-1009.

[23] F. Bao, J.-L. Yao, R.-A. Gu, Langmuir, 25 (2009) 10782-10787.

[24] J.-W. Hu, Y. Zhang, J.-F. Li, Z. Liu, B. Ren, S.-G. Sun, Z.-Q. Tian, T. Lian, Chemical Physics Letters, 408 (2005) 354-359.

[25] J.F. Li, X.D. Tian, S.B. Li, J.R. Anema, Z.L. Yang, Y. Ding, Y.F. Wu, Y.M. Zeng, Q.Z. Chen, B. Ren, Z.L. Wang, Z.Q. Tian, Nat. Protocols, 8 (2013) 52-65.

[26] R.M. Jarvis, R. Goodacre, Analytical Chemistry, 76 (2004) 40-47.

[27] X. Zhang, M.A. Young, O. Lyandres, R.P. Van Duyne, Journal of the American Chemical Society, 127 (2005) 4484-4489.

[28] E. Van Elslande, S. Lecomte, A.-S. Le Hô, Journal of Raman Spectroscopy, 39 (2008) 1001-1006.

[29] K.-i. Ataka, T. Yotsuyanagi, M. Osawa, The Journal of Physical Chemistry, 100 (1996) 10664-10672.

[30] S.C. Sun, I. Bernard, R.L. Birke, J.R. Lombardi, Journal of Electroanalytical Chemistry and Interfacial Electrochemistry, 196 (1985) 359-374.

[31] K. Kneipp, Y. Wang, H. Kneipp, L.T. Perelman, I. Itzkan, R.R. Dasari, M.S. Feld, Physical Review Letters, 78 (1997) 1667-1670.

[32] S.L. Kleinman, E. Ringe, N. Valley, K.L. Wustholz, E. Phillips, K.A. Scheidt, G.C. Schatz, R.P. Van Duyne, Journal of the American Chemical Society, 133 (2011) 4115-4122.

[33] K. Kneipp, Y. Wang, H. Kneipp, L.T. Perelman, I. Itzkan, R.R. Dasari, M.S. Feld, Physical review letters, 78 (1997) 1667.

[34] G. Braun, S.J. Lee, M. Dante, T.-Q. Nguyen, M. Moskovits, N. Reich, Journal of the American Chemical Society, 129 (2007) 6378-6379.

[35] K. Kim, J.K. Yoon, The Journal of Physical Chemistry B, 109 (2005) 20731-20736.

[36] M. Baibarac, M. Cochet, M. Łapkowski, L. Mihut, S. Lefrant, I. Baltog, Synthetic Metals, 96 (1998) 63-70.

[37] H. Yang, Y. Liu, Z. Liu, Y. Yang, J. Jiang, Z. Zhang, G. Shen, R. Yu, The Journal of Physical Chemistry B, 109 (2005) 2739-2744.

[38] J. Kneipp, H. Kneipp, K. Kneipp, Chemical Society Reviews, 37 (2008) 1052-1060.

[39] R. Gessner, P. Rösch, R. Petry, M. Schmitt, M. Strehle, W. Kiefer, J. Popp, Analyst, 129

(2004) 1193-1199.

[40] Z.-B. Lin, J.-H. Tian, B.-G. Xie, Y.-A. Tang, J.-J. Sun, G.-N. Chen, B. Ren, B.-W. Mao, Z.-Q. Tian, The Journal of Physical Chemistry C, 113 (2009) 9224-9229.

[41] B. Bozzini, C. Mele, L. D'Urzo, V. Romanello, Journal of Applied Electrochemistry, 36 (2006) 973-981.

[42] X. Junliang, I.B. Cosmin, A. Pierre, F.D. Louis, Journal of Physics B: Atomic, Molecular and Optical Physics, 49 (2016) 112001.

[43] A.H. Zewail, Science, 328 (2010) 187-193.

[44] U.J. Lorenz, A.H. Zewail, Proceedings of the National Academy of Sciences, 110 (2013) 2822-2827.

[45] R. Ernstorfer, M. Harb, C.T. Hebeisen, G. Sciaini, T. Dartigalongue, R.J.D. Miller, Science, 323 (2009) 1033-1037.

[46] D.-S. Yang, O.F. Mohammed, A.H. Zewail, Proceedings of the National Academy of Sciences, 107 (2010) 14993-14998.

[47] W. Liang, S. Schäfer, A.H. Zewail, Chemical Physics Letters, 542 (2012) 1-7.

[48] X. Fontané, L. Calvo-Barrio, V. Izquierdo-Roca, E. Saucedo, A. Pérez-Rodriguez, J.R. Morante, D.M. Berg, P.J. Dale, S. Siebentritt, Applied Physics Letters, 98 (2011) 181905.

[49] A. Ghita, F.C. Pascut, V. Sottile, I. Notingher, Analyst, 139 (2014) 55-58.

[50] G.M. Greetham, P. Burgos, Q. Cao, I.P. Clark, P.S. Codd, R.C. Farrow, M.W. George, M. Kogimtzis, P. Matousek, A.W. Parker, M.R. Pollard, D.A. Robinson, Z.-J. Xin, M. Towrie, Applied Spectroscopy, 64 (2010) 1311-1319.

[51] H. Yan, D. Song, K.F. Mak, I. Chatzakis, J. Maultzsch, T.F. Heinz, Physical Review B, 80 (2009) 121403.

[52] J.M. Glownia, J. Cryan, J. Andreasson, A. Belkacem, N. Berrah, C.I. Blaga, C. Bostedt, J. Bozek, L.F. DiMauro, L. Fang, J. Frisch, O. Gessner, M. Gühr, J. Hajdu, M.P. Hertlein, M. Hoener, G. Huang, O. Kornilov, J.P. Marangos, A.M. March, B.K. McFarland, H. Merdji, V.S. Petrovic, C. Raman, D. Ray, D.A. Reis, M. Trigo, J.L. White, W. White, R. Wilcox, L. Young, R.N. Coffee, P.H. Bucksbaum, Opt. Express, 18 (2010) 17620-17630.

[53] S.K. Sahoo, S. Umapathy, A.W. Parker, Applied Spectroscopy, 65 (2011) 1087-1115.

[54] A.H. Zewail, The Journal of Physical Chemistry A, 104 (2000) 5660-5694.

[55] G.E. Jellison, D.H. Lowndes, R.F. Wood, Physical Review B, 28 (1983) 3272-3276.

[56] F. Magnotta, I.P. Herman, Applied Physics Letters, 48 (1986) 195-197.

[57] G.D. Pazionis, H. Tang, I.P. Herman, IEEE Journal of Quantum Electronics, 25 (1989) 976-988.

[58] I.P. Herman, Journal of Applied Physics, 109 (2011) 016103.

[59] Y.-L. Gan, L. Wang, X.-Q. Su, S.-W. Xu, X. Shen, R.-P. Wang, Journal of Raman Spectroscopy, 45 (2014) 377-382.

[60] H. Fujimori, M. Kakihana, K. Ioku, S. Goto, M. Yoshimura, Applied Physics Letters, 79 (2001) 937-939.

[61] T. Hiroya, O. Atsushi, K. Junji, S. Takuro, F. Yukio, Japanese Journal of Applied Physics, 47 (2008) 2171.

[62] W.R. Zhang, C. Lowe, R. Smith, Progress in Organic Coatings, 66 (2009) 141-148.

[63] O.S. Fleming, S.G. Kazarian, E. Bach, E. Schollmeyer, Polymer, 46 (2005) 2943-2949.

[64] W. Schrof, E. Beck, G. Etzrodt, H. Hintze-Brüning, U. Meisenburg, R. Schwalm, J. Warming, Progress in Organic Coatings, 43 (2001) 1-9.

[65] B. Jiang, T. Ouchi, N. Shimano, A. Otomo, M. Kunimoto, M. Yanagisawa, T. Homma, Electrochimica Acta, 100 (2013) 317-320.

[66] M. Yanagasawa, M. Saito, T. Homma, in: 224th ECS Meeting, 2013, pp. J1-2640.

[67] M. Yamaura, R.L. Camilo, L.C. Sampaio, M.A. Macêdo, M. Nakamura, H.E. Toma, Journal of Magnetism and Magnetic Materials, 279 (2004) 210-217.

[68] Z. Liu, Z. Li, H. Zhou, G. Wei, Y. Song, L. Wang, Journal of Microscopy, 218 (2005) 233-239.

[69] S.D. Conzone, C.G. Pantano, Materials Today, 7 (2004) 20-26.

[70] J. Doh, D.J. Irvine, Proceedings of the National Academy of Sciences, 103 (2006) 5700-5705.

[71] A. Taglietti, C.R. Arciola, A. D'Agostino, G. Dacarro, L. Montanaro, D. Campoccia, L. Cucca, M. Vercellino, A. Poggi, P. Pallavicini, L. Visai, Biomaterials, 35 (2014) 1779-1788.

[72] M. Zhu, M.Z. Lerum, W. Chen, Langmuir, 28 (2012) 416-423.

[73] V. Subramanian, W.J. van Ooij, CORROSION, 54 (1998) 204-215.

[74] J. Kim, J. Cho, P.M. Seidler, N.E. Kurland, V.K. Yadavalli, Langmuir, 26 (2010) 2599-2608.

[75] H.J. Martin, K.H. Schulz, J.D. Bumgardner, K.B. Walters, Langmuir, 23 (2007) 6645-6651.

[76] Y. Zhu, S. Murali, W. Cai, X. Li, J.W. Suk, J.R. Potts, R.S. Ruoff, Advanced Materials, 22 (2010) 3906-3924.

[77] A. Eckmann, A. Felten, A. Mishchenko, L. Britnell, R. Krupke, K.S. Novoselov, C. Casiraghi, Nano letters, 12 (2012) 3925-3930.

[78] D. Teweldebrhan, A.A. Balandin, Applied Physics Letters, 94 (2009) 013101.

[79] L.G. Cançado, A. Jorio, E.H.M. Ferreira, F. Stavale, C.A. Achete, R.B. Capaz, M.V.O. Moutinho, A. Lombardo, T.S. Kulmala, A.C. Ferrari, Nano Letters, 11 (2011) 3190-3196.

[80] A.J. Pollard, B. Brennan, H. Stec, B.J. Tyler, M.P. Seah, I.S. Gilmore, D. Roy, Applied

Physics Letters, 105 (2014) 253107.

[81] M.S. Dresselhaus, A. Jorio, A.G. Souza Filho, R. Saito, Philosophical Transactions of the Royal Society a-Mathematical Physical and Engineering Sciences, 368 (2010) 5355-5377.

[82] P. Verma, P. Maire, P. Novák, Electrochimica Acta, 55 (2010) 6332-6341.

[83] K. Xu, Chemical Reviews, 104 (2004) 4303-4418.

[84] Lithium-ion battery. https://en.wikipedia.org/wiki/Lithium-ion_battery, Wikipedia, Retrieved on 1st November 2016.

[85] K. Xu, Chemical Reviews, 114 (2014) 11503-11618.

[86] D. Aurbach, M.D. Levi, E. Levi, A. Schechter, The Journal of Physical Chemistry B, 101 (1997) 2195-2206.

[87] K. Xu, G.V. Zhuang, J.L. Allen, U. Lee, S.S. Zhang, P.N. Ross, T.R. Jow, The Journal of Physical Chemistry B, 110 (2006) 7708-7719.

[88] I.A. Shkrob, Y. Zhu, T.W. Marin, D. Abraham, The Journal of Physical Chemistry C, 117 (2013) 19255-19269.

[89] D. Aurbach, L.M. Daroux, W.P. Faguy, E. Yeager, J. Electrochem. Soc., 134 (1987) 1611-1620.

[90] M. Onuki, S. Kinoshita, Y. Sakata, M. Yanagidate, Y. Otake, M. Ue, M. Deguchi, Journal of The Electrochemical Society, 155 (2008) A794-A797.

[91] K. Xu, A. von Cresce, Journal of Materials Chemistry, 21 (2011) 9849-9864.

[92] D. Aurbach, M.L. Daroux, P.W. Faguy, E. Yeager, Journal of The Electrochemical Society, 134 (1987) 1611-1620.

[93] S.H. Kang, D.P. Abraham, A. Xiao, B.L. Lucht, Journal of Power Sources, 175 (2008) 526-532.

[94] A.M. Andersson, K. Edström, Journal of The Electrochemical Society, 148 (2001) A1100-A1109.

[95] E. Peled, D. Bar Tow, A. Merson, A. Gladkich, L. Burstein, D. Golodnitsky, Journal of Power Sources, 97–98 (2001) 52-57.

[96] G.V. Zhuang, P.N. Ross, Electrochemical and Solid-State Letters, 6 (2003) A136-A139.

[97] K. Edström, M. Herstedt, D.P. Abraham, Journal of Power Sources, 153 (2006) 380-384.

[98] S. Malmgren, K. Ciosek, M. Hahlin, T. Gustafsson, M. Gorgoi, H. Rensmo, K. Edström, Electrochimica Acta, 97 (2013) 23-32.

[99] M. Nie, D. Chalasani, D.P. Abraham, Y. Chen, A. Bose, B.L. Lucht, The Journal of Physical Chemistry C, 117 (2013) 1257-1267.

[100] H. Bryngelsson, M. Stjerndahl, T. Gustafsson, K. Edström, Journal of Power Sources, 174

(2007) 970-975.

[101] M. Nie, D.P. Abraham, Y. Chen, A. Bose, B.L. Lucht, The Journal of Physical Chemistry C, 117 (2013) 13403-13412.

[102] R. Dedryvère, S. Leroy, H. Martinez, F. Blanchard, D. Lemordant, D. Gonbeau, The Journal of Physical Chemistry B, 110 (2006) 12986-12992.

[103] G.V. Zhuang, H. Yang, B. Blizanac, P.N. Ross, Electrochemical and Solid-State Letters, 8 (2005) A441-A445.

[104] Z. Wang, Y. Sun, L. Chen, X. Huang, Journal of The Electrochemical Society, 151 (2004) A914-A921.

[105] Z. Wang, X. Huang, L. Chen Journal of The Electrochemical Society, 151 (2004) A1641-A1652.

[106] N. Liu, H. Li, Z. Wang, X. Huang, L. Chen, Electrochemical and Solid-State Letters, 9 (2006) A328-A331.

[107] Z. Wang, X. Huang, L. Chen Journal of The Electrochemical Society, 150 (2003) A199-A208.

[108] P. Lu, C. Li, E.W. Schneider, S.J. Harris, The Journal of Physical Chemistry C, 118 (2014) 896-903.

[109] R. Marom, O. Haik, D. Aurbach, I.C. Halalay, Journal of The Electrochemical Society, 157 (2010) A972-A983.

[110] S. Shi, P. Lu, Z. Liu, Y. Qi, L.G. Hector, H. Li, S.J. Harris, Journal of the American Chemical Society, 134 (2012) 15476-15487.

[111] S. Shi, Y. Qi, H. Li, L.G. Hector, The Journal of Physical Chemistry C, 117 (2013) 8579-8593.

[112] P. Lu, S.J. Harris, Electrochemistry Communications, 13 (2011) 1035-1037.

[113] A.N. Dey, B.P. Sullivan, Journal of The Electrochemical Society, 117 (1970) 222-224.

[114] E. Peled, Journal of The Electrochemical Society, 126 (1979) 2047-2051.

[115] E. Peled, D. Golodnitsky, G. Ardel, J. Electrochem. Soc., 144 (1997) L208-L210.

[116] D. Aurbach, Journal of Power Sources, 89 (2000) 206-218.

[117] P.B. Balbuena, Y. Wang, Lithium-ion batteries: Solid-Electrolyte Interphase, Imperial College Press, London, 2004.

Chapter 2: Analysis on Nano-film samples: depth profile and kinetic reaction

2.1 Introduction

As introduced in the chapter 1, Raman spectroscopy is a suitable method to be used in elucidating the in-situ kinetic reaction and the interfacial structure at the surface and interface of nano-film materials. However, it is not sensitive enough to scan all materials and thin films (such as monolayers). In the chapter 2, the study is focused on demonstrating that Raman spectroscopy and surface-enhanced Raman spectroscopy (SERS) could be an effective technique for characterizing the depth profile and kinetic reaction of nano-thin films.

The demonstration of the capacity of SERS and Raman spectroscopy is carried out via the observation on (3-Aminopropyl) triethoxysilane drived self-assembled monolayers (APTES SAMs) and single-layer Graphene (SLG). APTES SAMs and SLG are thin-film materials with the thickness in nanometer scale. The structure of APTES SAMs and SLG are generally understood by many researches, yet some properties have not been precisely studied. In this chapter, the observations not only demonstrate the capacity of SERS for the interfacial analysis, but also find some new properties of APTES SAMs and SLG. For more detail, APTES SAMs and SLG are both used for demonstrating the time-resolved measurement, which can support the observation on kinetic reaction of nano-film materials. Besides, APTES SAMs is also used for demonstrating the resolution of the depth profile and the interfacial analysis with SERS sensor. In the following sections 2.1.1, 2.1.2 and 2.1.3, the backgrounds and motivations of these observations are introduced separately.

2.1.1 Depth profile on APTES SAMs

Although the accuracy of the depth profiling using normal Raman spectroscopy is limited, it could be improved by some methods. SERS coupled with SERS sensor could overcome the low sensitivity and resolution of the common Raman spectroscopic technique. The SERS sensor is essential for obtaining enhanced Raman signals. Ag nanoparticles (Ag NPs) have often been used as a conventional sensor among all SERS sensors [1, 2], and also in this study. It has a great potential for observing the subtle signals of molecular vibrations even at atomic level. Moreover, a piezo electric stage installed on Raman spectroscopy can support accurate displacement movement with a step of 0.05nm and realize a depth profile at atomic level combing with SERS. Jiang et al. [3] have successfully characterized hydrazine adsorption on Cu surface at the

nanometer scale using a plasmonic antenna enhancing Raman scattering.

In the section 2.3.1, we attempt to carry out the depth profiling of APTES SAMs, in search of the accurate and distinct inner molecular information, by using SERS. The target sample APTES SAMs has been investigated by many methods, including ellipsometry [4], UV–visible absorption [5] and XPS [6], and so on. However, for a sample with such an extremely thin layer structure (several nanometers for mono-, bi-, or tri-layers), detailed analysis of the interior structural variation is fairly difficult to realize. There is no accurate depth profile on APTES SAMs by using any approach yet. Therefore, we attempted to investigate the internal variation in ultrathin APTES SAMs by using SERS. Some encouraging results were observed during this scanning, which are valuable of understanding APTES SAMs internal structure. The internal molecular structure was successfully measured and distinguished with atomic resolution. Moreover, these observations also identify the capacity of SERS for the accurate depth profiling.

2.1.2 Kinetic reaction of APTES SAMs

Time-resolved measurement mode is a significant technique for observing interfacial reaction. In this chapter, another function of Raman spectroscopy, kinetic observation together with temperature calculation by using anti-stokes and stokes Raman scattering, is demonstrated in the section 2.3.2 via the analysis of APTES SAMs and SLG.

APTES SAMs has been investigated by many methods, but there has been very little research on the phase transition process (from ordered to disordered structure) of APTES SAMs. The phase transition of its ordered structure is significant for its application because a disordered APTES SAMs could weaken the device property and performance. Regarding the phase transition temperature, the melting and boiling points of standard bulk APTES are −70 and 217 °C, respectively. However, after APTES self-assembled on a substrate, it can maintain the solid state even under an environmental temperature above the melting point of bulk APTES. Therefore, there must be a higher melting point and a specific phase transition process of APTES SAMs than the bulk APTES sample.

For a sample with such an extremely thin layer structure (several nanometers for mono-, bi-, or tri-layers), detailed analysis of the interior structural variation is fairly difficult to realize. In section 2.3.2.1, to gain insight into the mechanism of the phase transition process inside APTES SAMs and estimate the phase transition temperature, the anti-Stokes and Stokes surface-enhanced

Raman spectroscopy is employed. Ag NPs were adsorbed on the top of the APTES SAMs film to create localized Raman enhancement (SERS hotspots). Consequently, the anti-Stokes scattering could be observed together with enhanced Stokes scattering, so that the phase transition temperature for APTES SAMs could be calculated using the equation introduced in section 1.1.3.2, "$I_{as}/I_s = \exp(-h\nu/kT)$". Generally, anti-Stokes Raman scattering is rather weak, so it is hard to observe anti-Stokes Raman signals from materials with low Raman activity. Fortunately, Ag NPs deposited on an APTES SAMs can enhance the Raman signals of not only Stokes scattering but also anti-Stokes scattering. A time-resolved measurement mode was used to monitor the kinetic in-situ variation in the Raman spectra. The laser beam in this research was used not only to excite Raman spectra but also to heat the sample for generating phase transition. The phase transition of APTES SAMs from ordered to disordered structure under laser heating can be discussed and analyzed according to the variation in Raman peaks representing specific bonds.

2.1.3 Kinetic reaction of SLG

SLG is another sample for demonstrating the kinetic observation. The thermal stability of graphene has a close relationship with defect generation, thermal oxidation, which in turn have a significant bearing on its properties and applications [7, 8]. Graphene is sensitive to the environmental temperature [9, 10]. Therefore, it is necessary to study the thermal stability of graphene. The chemical properties are known to be different at the edge and basal plane [11]. It is possible that these differences could affected the heat-induced defects. Hence, the thermal stability of both the basal plane and the edge [12, 13] were studied. Raman spectroscopy is an effective tool for characterizing defects, disorder structures, and doping in single-layer graphene (SLG) [14-19]. It was reported that the nature of defects can be probed with the intensity of the D peak, since the breathing modes of sp2 atoms originate from defects. Many studies have quantified the number of point defects in SLG using the intensity ratios of the D and G peaks, I(D)/I(G) [20-22]. In addition, a decrease in the I(2D)/I(G) ratio can be an indicator of the increase in doping levels in graphene [7, 18, 19, 23, 24]. The anti-Stokes and Stokes Raman signals are effective for calculating dynamic temperature changes during the heating process. The relationship between temperature and ratio of anti-Stokes and Stokes Raman intensity (I_{as}/I_s) is given by $I_{as}/I_s = \exp(-h\nu/kT)$, as introduce in section 1.1.4. This relation may be used to analyze the variation of the kinetic anti-Stokes and Stokes Raman spectra of SLG with the temperature at each moment.

In previous literatures, the thermal stability of SLG edge has been demonstrated to be lower than that of basal plane [12] caused by thermal annealing, electron beam irradiation and proton irradiation, but none of research on laser beam irradiation. Besides, oxygen hole-doping was also found to increase with elevation in temperature [7]. Therefore, in section 2.3.2.2, the thermal stability was monitored at the SLG basal plane and edge using anti-Stokes and Stokes Raman spectroscopy, instead of other ex-situ methods. The confocal excitation laser was the thermal source used to heat the sample and excite Raman scattering simultaneously. More precise temperature variation could be calculated along with thermal treatment. In addition, how the point defects and accompanying oxygen bonded at SLG basal plane and edge can be also discussed from analysis of the kinetic Raman spectra.

The time-resolved measurement on APTES SAMs and SLG could demonstrate the ability of SERS and Raman spectroscopy for observing kinetic reaction.

2.2 Experimental section

2.2.1 Samples and materials

Making process of APTES SAMs mainly followed the previous literature [25]: APTES (99%, Sigma-Aldrich), toluene (99.5%, Kanto Kagaku), and ethanol (99.5%, Kanto Kagaku) were used. The substrate was TEMPAX® glass (20 × 20 × 1.0t mm^3, Musashino Fine Glass). The APTES SAMs sample used in this study was prepared as follows. First, a glass substrate was cleaned using a solution of sulfuric acid and hydrogen peroxide (H_2SO_4:H_2O_2 = 2:1) for 10 min. Next, the cleaned substrate was immersed in 10 mL of toluene solution containing 0.043 mmol of APTES at 60 °C for 10 min, during which the APTES SAMs film formed. The SAM was rinsed with ethanol under ultrasonication for 2 min to remove physisorbed APTES molecules. A film of nm-sized Ag NP was adsorbed on the amine-modified glass via evaporation (*Figure 2.1*) to enhance the Raman scattering. Finally, island-like Ag film was formed as a SERS plasmonic sensor due to aggregation process, with the average thickness of over 10 nm (*Figure 2.4*).

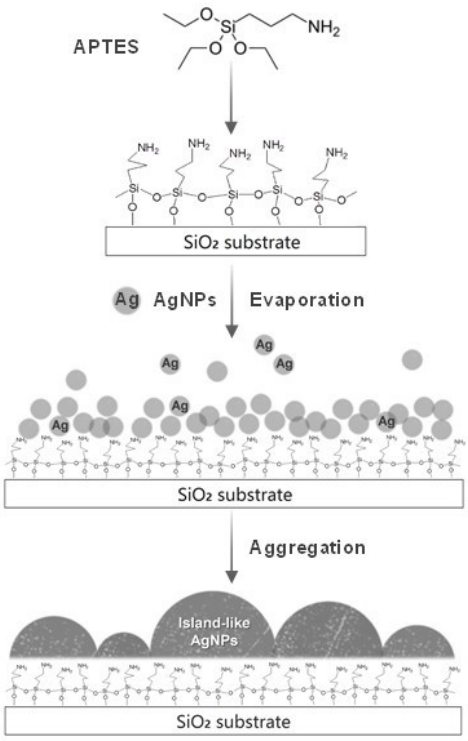

Figure 2.1 Schematic diagram of deposition process and estimated structure of APTES SAMs with Ag NPs.

Graphene: Single-layer graphene on SiO_2 substrate was purchased from Graphene Platform Corp. The SLG was transferred on quartz substrate via chemical vapor deposition (CVD) method.

2.2.2 Raman Spectroscopy and SERS

Microscopic confocal Raman spectroscopy (Tokyo Instrument Co.) was installed with excitation wavelengths of 785 nm and 532 nm, with the minimum resolution of 0.7 cm^{-1}. The SERS sensor for observing APTES SAMs is Ag NPs. Ag NPs were adsorbed on the APTES SAMs to enhance the Raman signal and obtain subtler structural information. There is no SERS sensor for the observation on graphene.

2.2.3 Atomic Force Microscopy (AFM)

AFM images of APTES SAMs were collected in tapping mode using a multimode scanning probe microscope produced by Veeco Instruments, Inc. The images in this thesis covered an area of 0.25 μm^2, which are the same size as the original images. The AFM images was processed using a third-order X–Y plane fit image.

2.2.4 Depth profile measurement on APTES SAMs using Raman spectroscopy and piezo electric stage

For the depth profile on APTES SAMs, Raman spectroscopy was employed with excitation wavelength of 785 nm (laser power of 1.38 mw to avoid the thermal damage) and resolution of 3.3 cm^{-1}. At first, the laser beam was irradiated to APTES SAM surface. And then the focus position was moved from surface to substrate by using the piezo electric stage, which was installed to support the accurate displacement movement with a step of 0.05 nm. The narrow focus range can achieve an accurate depth profile, which is due to the enhanced electric field. The schematic of using this tool in combination with SERS is displayed in *Figure 2.2*. Combined with this device, an accurate depth profiling, even of monolayers, could be realized by SERS.

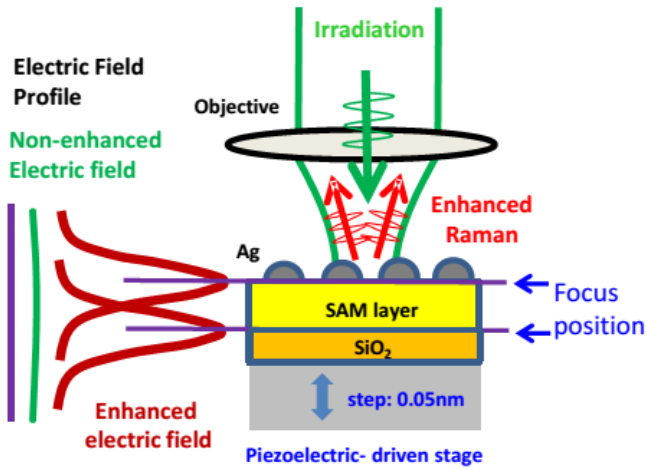

Figure 2.2 Schematic diagram of the depth-profiling measurement on APTES SAMs with SERS

2.2.5 Heating method and kinetic measurement on APTES SAMs and SLG using Raman machine

For kinetic measurement on APTES SAMs, Raman spectroscopy was employed to obtain anti-Stokes and Stokes Raman signals, with excitation wavelengths of 785 nm (the laser power was 13.8 mW) and a notch filter for recording anti-Stokes signals. The focused laser beam was used not only to excite Raman spectra but also to heat the sample. A time-resolved kinetic measurement mode was used, with an exposure time of 1 s and kinetic cycle time of 1.1 s. Ag NPs were adsorbed on the APTES SAMs samples to enhance the Raman signal and obtain subtler structural information.

To observe the thermal dynamics of SLG, Raman spectroscopy was employed to obtain anti-Stokes and Stokes Raman signals. Microscopic confocal Raman spectroscopy (Tokyo Instrument Co.) was used with excitation wavelengths of 532 nm (the laser power was 29.9 mW) and a notch filter for recording anti-Stokes signals. The confocal laser was not only used to excite Raman signals, but also to heat the SLG surface. With the laser beam heating, Raman spectra were recorded in kinetic cycle series using exposure time of 1s, grating of 200 G/mm and pinholes of 50 μm.

2.2.6 DFT calculation on the theoretical Raman frequencies of APTES

A density functional theory (DFT) calculation was performed to simulate the Raman frequencies of APTES SAMs. It was conducted using the Gaussian 09 package [26] to assign the experimental Raman peaks to appropriate vibrational modes. We optimized the geometry of the adsorption system containing the Ag particle and APTES molecule. The Ag particle was modeled as a tetrahedral cluster with 20 atoms because this cluster is applicable for full geometrical optimization. The APTES molecule was assumed to interact with the tip of the Ag cluster via $-NH_2$.

B3LYP was used as the exchange-correlation functional [27, 28]. As basis sets, 6-31G** was applied to H, C, and Si atoms, and 6-31+G** was applied to N and O atoms [29]. A different basis set was used for N and O because N and O are relatively electronegative and exhibit a strong tendency to accept electrons, so they require a larger basis set. For Ag, the effective core potential of Hay and Wadt [30] was selected as the substitute for the Ar core. Because the solvent environment was assumed to surround the adsorption system, a polarizable continuum model (IEFPCM) [31] having a dielectric constant of 78.35 was applied in the calculation.

2.3 Results and discussion

2.3.1 Depth profile and interfacial analysis on APTES SAMs by using SERS

2.3.1.1 Characterization of APTES SAMs by AFM

The sandwich-like sample Ag-APTES SAMs-SiO_2 was prepared according to the method in section 2.2.1. To characterize this sample, AFM was used to determine the morphology and roughness of each specimen on the APTES film. The AFM image was recorded in tapping mode and the representative morphology and sectional views with detailed height data are presented in *Figure 2.3* (without Ag deposited) and *Figure 2.4* (with Ag deposited). According to *Figure 2.3*, the roughness of APTES SAMs should be ~1.5 nm. This indicates that inhomogeneous multilayers (bi-layer or tri-layer) are partially formed in this APTES film (*Figure 2.3* a). It might be induced by the silanization method using hot toluene, which was also described by Zhu et al. (*Figure 1.16* in the chapter 1) [32]. From *Figure 2.4*, it can be found that the island-like Ag layer was formed due to the evaporation process, with the thickness of over 20 nm.

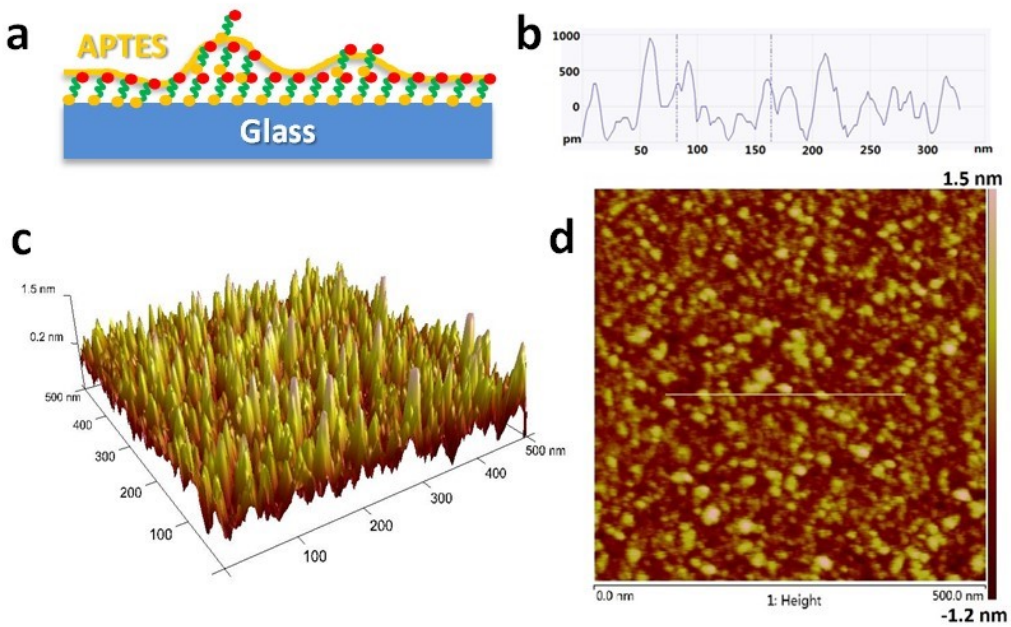

Figure 2.3 a: schematic of hypothetical APTES SAMs structure with multi-layer without Ag NPs; b, c, d: AFM image of the morphology of APTES SAMs without Ag NPs

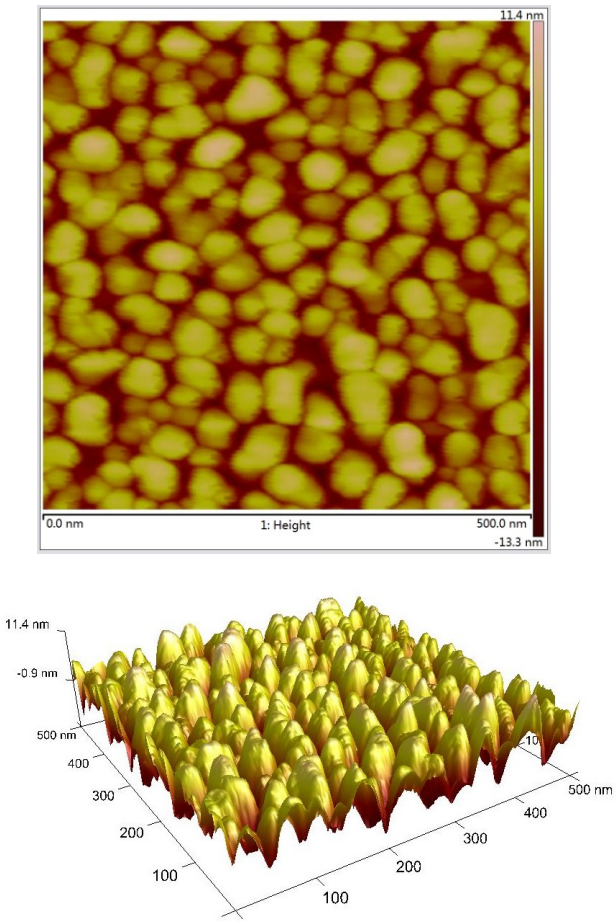

Figure 2.4 2D (above) and 3D (below) morphology of Ag NPs deposited APTES SAMs sample observed by AFM. An island-like Ag NPs film with a thickness of several tens nm was observed.

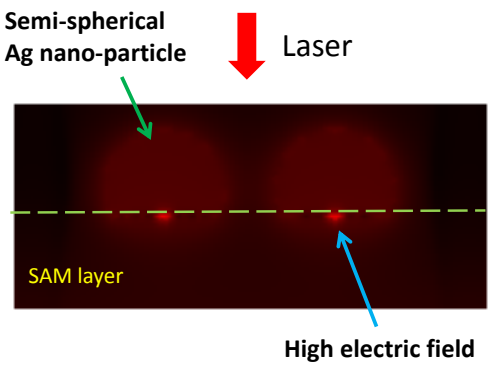

Figure 2.5 Calculated electric field image by Finite Difference Time Domain (FDTD). The evaporated Ag NPs film would be a semi-spherical island film. A High electric field could be generated around the center of semi-sphere.

Based on the observed AFM images of APTES SAMs and Ag layer, the estimated electric field generated by semi-sphere Ag NPs was calculated by Finite-difference time-domain (FDTD) and presented in *Figure 2.5*. The calculation result in *Figure 2.5* illustrate that the high electric field that support SERS enhancement could be generated around the center of semi-sphere Ag NPs. According to the morphology and FDTD calculation, the speculated schematic of the APTES SAMs and the Ag NPs deposited at the interface was draw in *Figure 2.6* a to describe the inhomogeneous APTES SAMs structure, the deposited Ag NPs film and the electric field distribution. Since this schematic shows the structure in the sub-nanometer scale, Ag NPs at the very interface were considered to be single particles one by one, but not the island-like Ag layer with the thickness of 20 nm.

2.3.1.2 Surface-Enhanced Raman Spectra of APTES SAMs

To analyze the internal structural inside APTES SAMs, the primary task is obtaining Raman signals and making all the necessary assignments to certain bands. However, for such an ultrathin sample, investigation of the internal structure using ordinary Raman measurement mode is very difficult. *Figure 2.6* b (black) depicts the normal Raman spectrum of APTES SAMs without Ag NP deposits; almost no peaks appeared. Consequently, SERS is necessary to obtain Raman signals for investigating internal structure (further analysis will be explained in section 2.3.1.3 and 2.3.1.4).

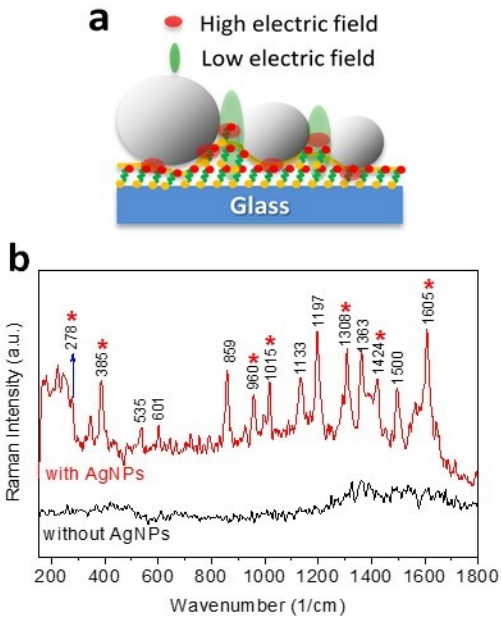

Figure 2.6 a: schematic of hypothetical APTES SAMs deposit with Ag NPs; b: SERS spectra of APTES SAMs

Figure 2.6 b (red) shows the entire enhanced Raman peaks at wavenumbers smaller than 1800 cm^{-1}. As mentioned in the experimental section, a thin nano-metal film consisting of Ag NPs with a thickness of 20 nm was evaporated on the surface of the APTES SAMs and acted as SERS sensor. An electric field created by SERS sensor at the interface between island-like AgNP and sample's surface was simulated by the FDTD calculation in *Figure 2.5*. We can speculate that a high electric field could be generated around the center point of semi-sphere. As expected, in the experimental results of SERS spectra (*Figure 2.6* b), it could indeed enhance weak Raman signals so that we can record the Raman scattering due to bond vibration in APTES SAMs.

Table 1 lists the assignments of these vibrations and the sources to refer. These assignments were made using the theoretically calculated results and information from the literatures [33, 34]. The Raman bands at 383 and 1129 cm^{-1} are due to the bond-bending vibration of O–Si–O and Si–O–Si, respectively. The band at 854 cm^{-1} can probably be assigned to carbon chain vibration modes. The band at 1069 cm^{-1} comes from the stretching vibration of C–C, which is near the Si atom in the carbon chain. The band at 1402 cm^{-1} could be assigned to the bending vibration of CH_2, which is bonded to the Si atom. The band at 1604 cm^{-1} could be attributed to the bending vibration mode of NH_2.

Table 2.1 Frequencies and band assignments for APTES SAMs

Frequency	Assignments	References
278 cm^{-1}	Ag-N	DFT Calculation
385 cm^{-1}	O-Si-O & Si-O-Si	DFT Calculation
859 cm^{-1}	Carbon chain	DFT calculation
960 cm^{-1}	CH_2 & NH_2	DFT Calculation
1015 cm^{-1}	Skeletal stretch	DFT Calculation
1308 cm^{-1}	CH_2	DFT Calculation & References [33, 34]
1424 cm^{-1}	Si-$\underline{CH_2}$	DFT Calculation & References [33, 34]
1605 cm^{-1}	NH_2	DFT Calculation & References [33, 34]

2.3.1.3 Vertical structure of internal APTES SAMs

APTES SAMs assembled on silica surface contain various atomic bands in the vertical direction. *Figure 2.7* displays depth profiling at five specific vibrations on intensity and full-width at half-maximum (FWHM) at partial frequencies in Table 1, 278, 385, 1605, 960, and 1424 cm^{-1}. The grey area signifies the speculated area of the APTES SAMs. X-axis shows each vertical position, from the initial displacement toward substrate for the depth scanning. "0" stands for the Ag NPs side, and "10" stands for the glass substrate side. The laser scans from "0" to "10". To clearly describe every band in the molecule discussed in *Figure 2.7*, schematic of each vibration is displayed in *Figure 2.8*.

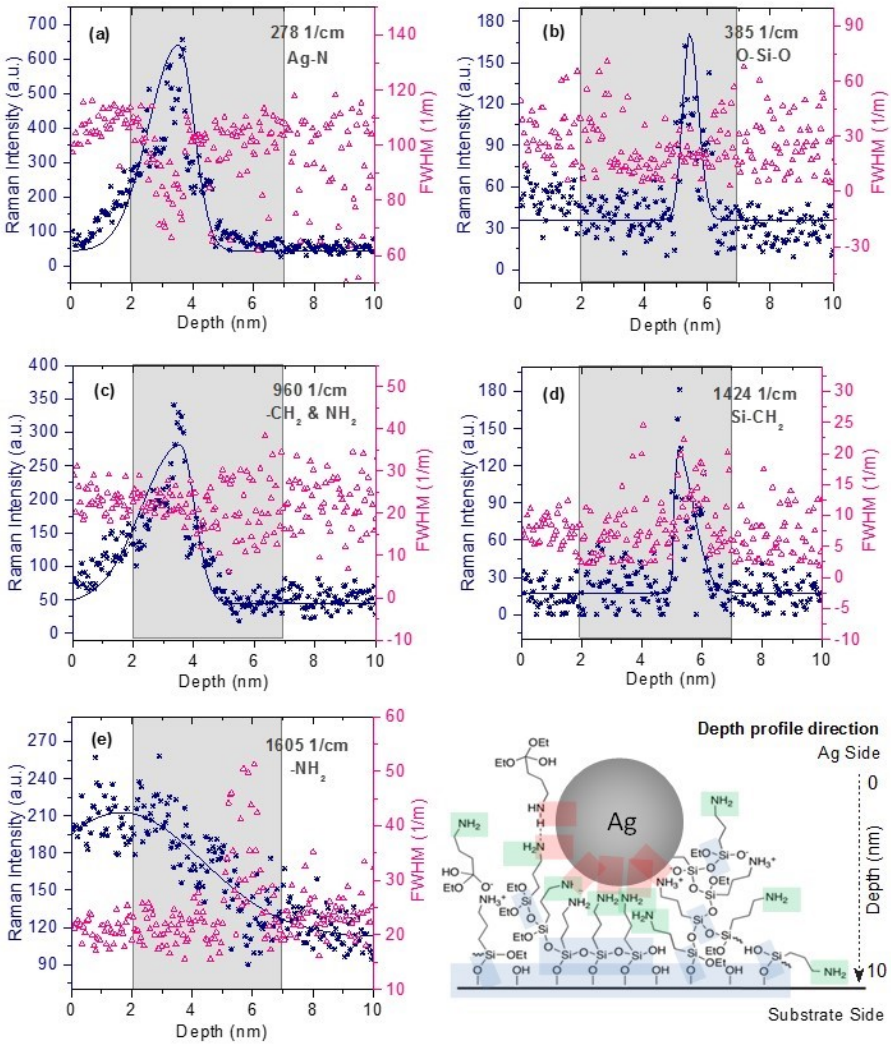

Figure 2.7 Depth profile (Raman intensity and FWHM) of APTES SAMs at 278, 385, 960, 1424, and 1605 cm^{-1}

There are five Raman assignments shown in *Figure 2.8*, attributed to Ag–N, O–Si–O, $–NH_2$, $–CH_2$ and Si–$\underline{CH_2}$ band vibrations. Obviously, at the grey area in depth profiling graph, the intensity of the Ag–N vibration decreases rapidly, the Si–O vibration appears and increases abruptly, and the $–NH_2$ group vibration decreases gradually. The intensity variation on $–CH_2$ group and Si–$\underline{CH_2}$ band, being similar to Ag–N and Si–O, rapidly decrease and suddenly appear, respectively. Comparing with the internal molecular structure and vibration assignments in *Figure 2.8*, one can easily infer that the intensity variations of these peaks could correspond to the chemical structure (Figure 1.16) sequence of APTES SAMs, to a certain extent. The wide range of amino group is caused by the bend structure and accumulation of APTES moieties, which allow amino group exist at the whole depth displacement. The sharp depth profile of Si-O vibration relies on the high orientation of Si-O at the surface of silica substrate, which show much higher Raman signals than the vibration in the disorder structure. Moreover, regarding the FWHM variation, vibrations at 278 and 1605 cm^{-1} show the narrowest FWHM when strongest intensities were observed. For vibrations at 385, 960, and 1424 cm^{-1}, FWHM distribution was scattered at the vertical positions where only weak Raman signals could be found and was concentrated when the Raman signals were strongest.

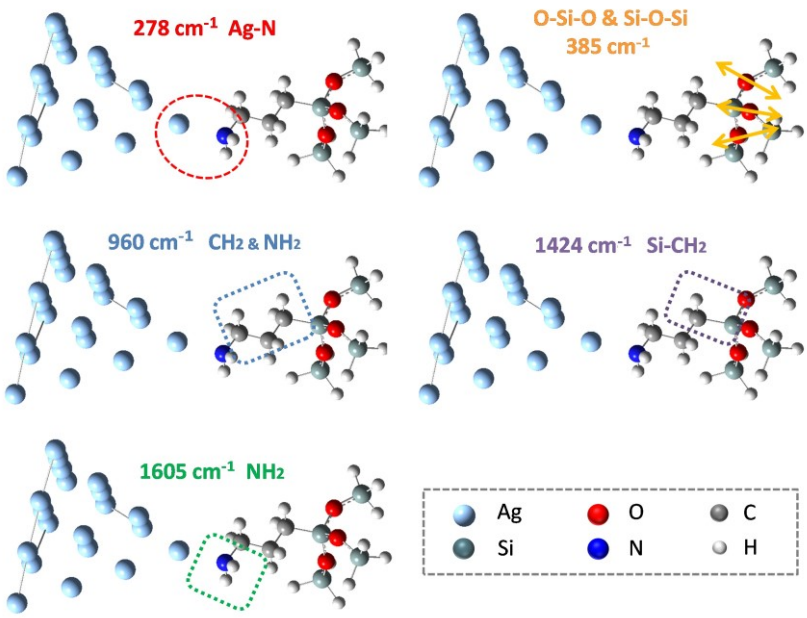

Figure 2.8 Vibration modes at 278, 385, 960, 1424, and 1605 cm^{-1}

The depth profile shows the vertical structure of monolayer APTES, which does not correspond with the formation of multilayers we discussed in the section 1.2.1 of chapter 1. At this moment, the multilayer structure cannot be distinguished. On one hand, as mentioned in *Figure 1.16* in chapter 1, Zhu et al. [32] discussed the irregular structure of APTES-derived layer. Upon the lowest layer, there might be almost no APTES molecules orientated vertically and regularly which lead to the difficulty in depth profiling the upper layers. On the other hand, the signals of the peaks at each depth displacement were collected from average vibration. The vibrations from the highly orientated molecules would dominate the detectable signals, comparing with that from the irregular molecules.

Besides, the speculated APTES SAMs shows a thickness of 5 nm, which is larger than APTES monolayer (0.7 nm [35]). This is the unavoidable error, due to the molecular vibration and the scattering resolution. Moreover, not every vibration was distinguished by depth profile, because of the unsure complicated orientation of the APTES moieties in the APTES SAMs. But at least, these results demonstrate that SERS could be employed to distinguish some significant vibrations of the internal molecular structure of the APTES SAMs in nanometer scale.

2.3.1.4 Frequency shift at interfaces

Beyond the identification of inner molecular bands and groups, more information can be obtained, analyzed, and deduced from this depth profiling. According to a general theory of frequency (or wavenumber) shift (*Figure 2.9*), when a molecule "A-B-C" is adsorbed on a substrate as "substrate-A-B-C", the Raman frequency of the bonded band "A-B" is shifted to lower frequency than the free band "A-B". Based on this theory, similar adsorption phenomenon at the Ag NPs–APTES SAMs and APTES SAMs–substrate interfaces could be further analyzed and discussed to elucidate the adsorption behavior.

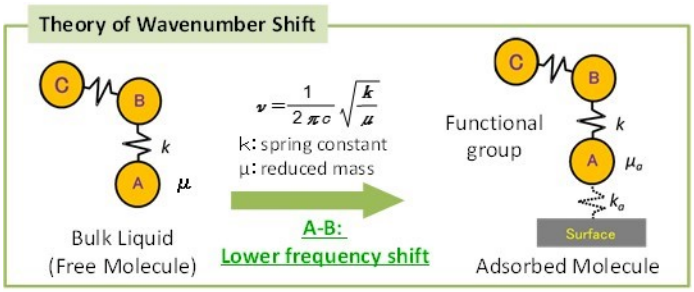

Figure 2.9 The theory of wavenumber shift when a molecule is adsorbed on a substrate

According to the previous studies, the bond between an APTES SAMs and silica substrate should be Si–O. In *Figure 2.10*, the left-hand-side graph shows the depth profile of the Raman intensity of Si–O vibration at slash shadow area (depth position from 5.0 to 6.2 nm). Same as *Figure 2.7*, the depth value "0" stands for the Ag NPs side, and "10" stands for the glass substrate side. The right-hand-side graph shows the variation in Raman frequencies at each depth position within this slash area. *Figure 2.10* (right) shows that the wavenumber gradually shifted from 396 toward 385 cm^{-1}, with the laser moving from surface side to substrate side.

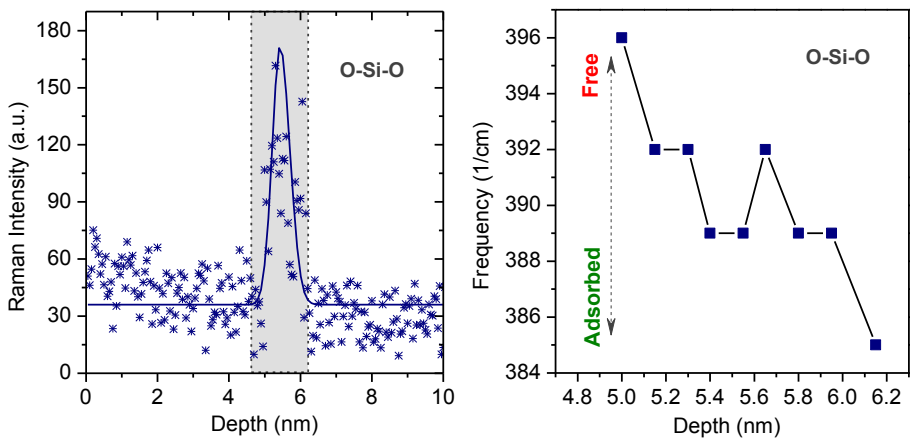

Figure 2.10 Frequency at Si–O band shifted dependent on vertical position (Left: Depth profiling of band Si–O; Right: Frequency shift at vertical direction of band Si–O)

According to the general theory of frequency shift, the decrease in Raman frequency in the right-hand-side graph may represent different kinds of Si–O vibrations. The higher frequencies (396–392 cm^{-1}) at upper depth position arise from free Si–O band and the lower frequencies (389–385 cm^{-1}) at the substrate side could be attributed to the substrate-bonded Si–O band. To describe these bands clearly, the schematic of the frequency shift at Si–O band is shown in *Figure 2.11*. The higher frequency at upper position stands for the free Si–O vibration, which may be induced by some unbounded APTES moieties. The lower frequency stands for the bonded Si–O vibration, caused by the adsorption of APTES moieties on the glass substrate. For this APTES SAMs sample, it could be speculated that not all APTES moieties are bonded with each other, and that free and bonded Si–O band existed at the same time. This conclusion also corresponds to the proposed structure in *Figure 1.16* (Chapter 1).

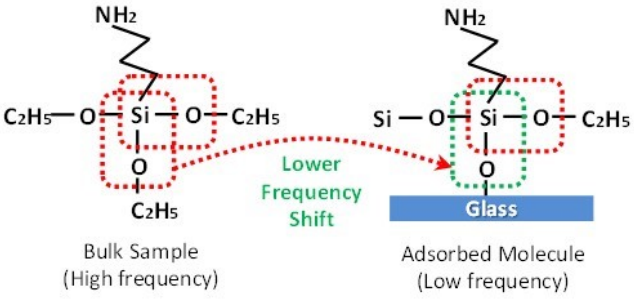

Figure 2.11 Schematic of the shift occurred in the frequency at Si–O band

Apart from the substrate-bonded Si–O band, there is another interface, the Ag–APTES SAMs interface. With the adsorbed group $–NH_2$ group. The depth profile of the $–NH_2$ group is shown in *Figure 2.12* (left). Same as earlier, the depth value "0" stands for the Ag NPs side, and "10" stands for the glass substrate side. The right-hand-side graph in *Figure 2.12* shows the variation in the Raman frequencies at each depth displacement from 0 to 10. The wavenumber shifted from 1611 to 1605 cm^{-1} as the laser moves from the surface side to the substrate side.

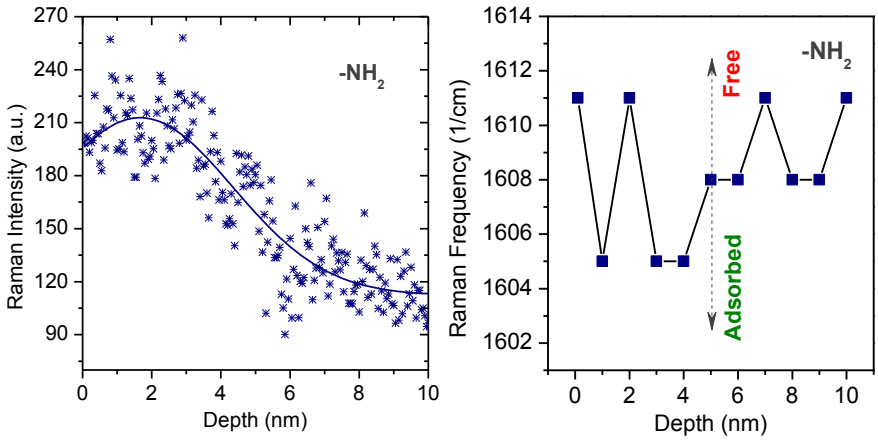

Figure 2.12 Frequency at $–NH_2$ group shifted depending on vertical position (Left: depth profiling of amino group; Right: frequency shift in vertical direction of amino group)

To discuss the bonded band and free band at the Ag-APTES SAMs interface, a schematic is shown in *Figure 2.13* (a). The higher frequencies stand for the free $–NH_2$ vibration, which may be induced by non-bonded APTES moieties, and the lower frequencies stand for the bonded –

NH_2 vibration, caused by the adsorption of APTES moieties on Ag layer. This schematic shows that the frequency before the depth position 4 nm comprises both high and low frequencies, indicating that both free amino and adsorbed amino groups existed at the Ag-side interface. The frequencies after 4 nm were shifted to higher wavenumbers, which means that a lot of free amino groups in the region of inside APTES SAMs and substrate-side interface (*Figure 2.13* (b)). This conclusion agrees with some previous studies, which state that some hydrogen bonds maybe formed on amines at the substrate surface. It is possible that some of the molecules aligned towards the substrate surface with the head and tail groups because of the bent molecules. [36]

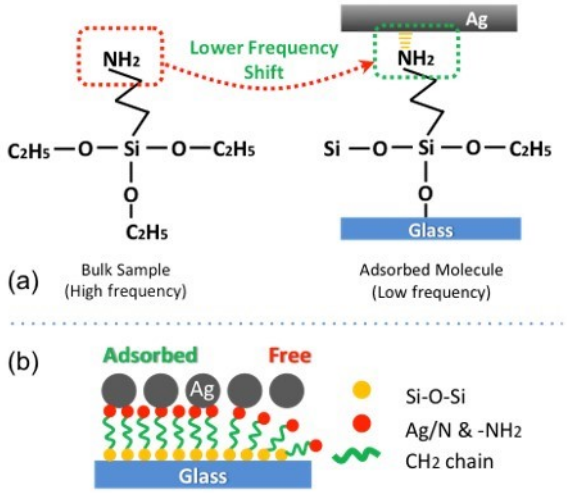

Figure 2.13 Schematic diagram of the (a) shift occurred in the frequency at amino group and (b) various orientation of APTES molecule.

From all the analyses discussed above, the vertical structure of thin layer APTES was distinguished, by using SERS combining with piezo electric stage. SERS is demonstrated to show high sensitivity and resolution to the depth profiling of nano structure and interface.

2.3.2 Kinetic reaction of APTES SAMs and SLG observed by using SERS and Raman spectroscopy

The in-situ kinetic observation on the real-time reaction is another significant aspect for the interfacial analysis. In the section 2.3.2, the capacity of SERS and Raman spectroscopy in the time-resolved measurement is demonstrated using the nano-film samples APTES SAMs (section 2.3.2.1) and SLG (section 2.3.2.2).

2.3.2.1 In-situ kinetic anti-Stokes and Stokes Raman spectra observed on APTES SAMs

Using the method described in the experimental section, the temperature variation of the APTES SAMs was monitored under laser heating to estimate the phase transition temperature. The same as the section 2.3.1, the APTES SAMs was prepared on a silica surface, and Ag NPs were deposited on it using an evaporation method to enhance the Raman signals. Under laser beam heating, Raman spectra were recorded in a kinetic cycle series (exposure time, 1 s; kinetic cycle time, 1.1 s). *Figure 2.14* shows the in-situ anti-Stokes and Stokes Raman spectra of APTES SAMs for durations of 1.1 to 77 s (a–j).

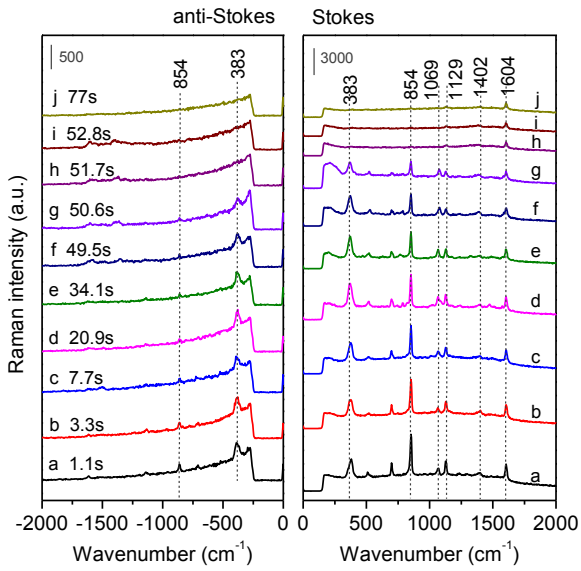

Figure 2.14 In-situ anti-Stokes and Stokes Raman spectra of APTES SAMs for kinetic heating times of 1.1 s to 77 s.

The curves in *Figure 2.14* clearly show that the Raman signals varied with the laser heating (temperature changing). The intensities of these sharp Raman peaks became weaker with increasing duration and temperature (curves a to g). Most of the Raman signals then suddenly became extremely weak and were difficult to observe and distinguish. Furthermore, regarding the full width at half-maximum (FWHM) of these peaks, *Figure 2.17* (blue curve) show a broadening trend, especially the FWHM of these peaks after 50.6 s. This broadening peaks could indicate a phase transition toward disorder. Accordingly, the moment, at which the APTES peaks quenched between curves g and h, should be defined as the phase transition moments from ordered monolayer structure to disordered structure.

Meanwhile, in *Figure 2.14*, two anti-Stokes peaks were recorded together with Stokes peaks, at minus wavenumber 383 cm^{-1} (O-Si-O) and 854 cm^{-1} (Carbon chain). Considering that the behavior of carbon chain could represent for the phase transition behavior of APTES moieties, the intensity of carbon chain peak (854 cm^{-1}) could be used to estimate the phase transition temperature. Therefore, using the equation "Ias/Is = exp(−hv/kT)" in the section 1.1.3.2, the temperature for each curve (a–g) were calculated from peak 854 cm^{-1} as shown in *Figure 2.15*. According to the temperature calculation curve (red), the temperature dropped briefly owing to an endothermic reaction caused by the beginning of molecular disorder and gradually rose back toward 118 °C while the phase transition process clearly occurred. These calculated temperatures provide an estimated phase transition temperature 118 °C for APTES SAMs, and give an information that the actual application of crystalline APTES SAMs should be controlled under phase transition temperature to maintain the stable oriented structure. A schematic diagram of the phase change process is shown in the right panel of *Figure 2.15* [33, 37]. (The details on the variation in the structure will be discussed in *Figure 2.17*)

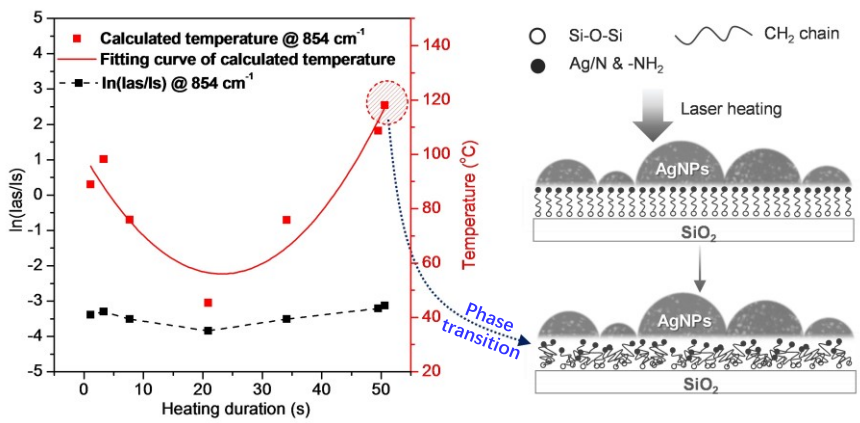

Figure 2.15 Calculated temperature variation during heating (left) and schematic diagram of phase change process (right) of APTES SAMs.

Each temperature was also calculated from the peak at 383 cm^{-1} in *Figure 2.16* and the calculated temperature (solid black line in *Figure 2.16* left) was lower than temperature calculated from peak 854 cm^{-1} (dash black line in *Figure 2.15* left). The explanation is described as follows. In *Figure 2.16*, the right hand side is a model of the temperature distribution when the phase transition process occurred. Owing to the different thermal conductivity (k) of Ag, APTES and SiO_2 (Glass with a thickness of 1 mm), there should be a temperature gradient inside APTES SAMs during such short heating time (shorter than 1 min). In this model, the Ag could store the thermal energy from laser beam and transfer energy to APTES SAMs as a role of heating source. However, comparing with the thermal conductivity of Ag, the SiO_2 have the nature of extremely low thermal conductive which would lead to the uneven temperature distribution until the thermal energy in Ag is saturated. It is the reason why the temperature calculated from 383 cm^{-1} (O-Si-O band) was lower than that calculated by using 854 cm^{-1} (Carbon chain).

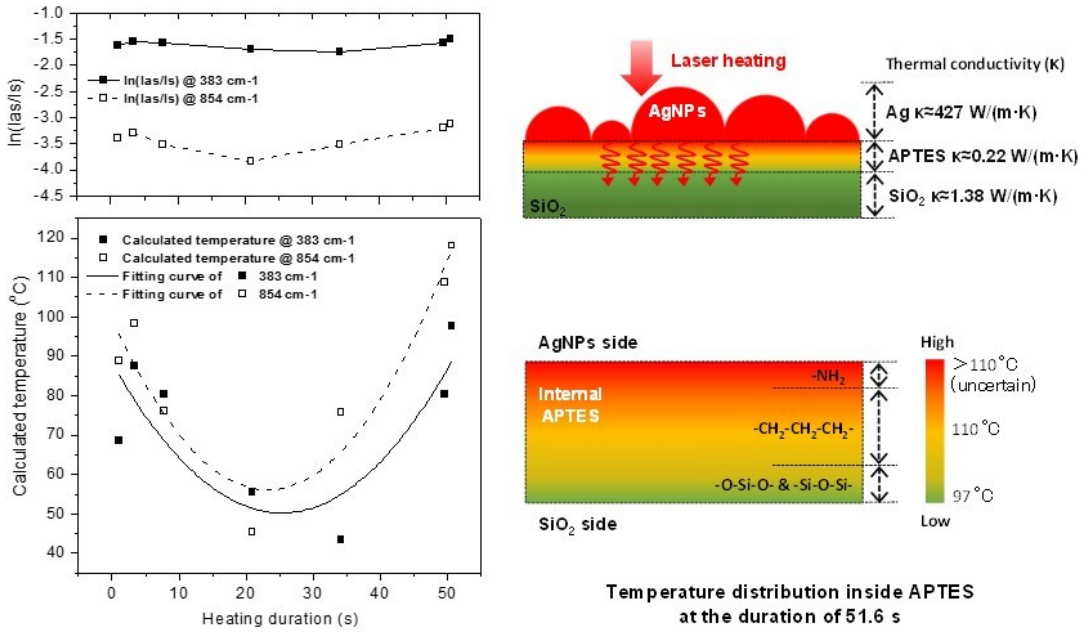

Figure 2.16 Left: The calculated temperature variation along with laser beam heating from peaks at 383 cm^{-1} and 854 cm^{-1}. Right: The estimated temperature distribution inside APTES SAMs when the duration is 51.6 s (phase transition temperature) caused by different the thermal conductivity at two interfaces.

In addition to providing an estimate of the phase transition temperature, the results also support the assumption regarding the structural change from ordered to disordered. The intensities and FWHM variations for each vibration are shown in *Figure 2.17*. In combination with the assignments (Table 2.1 in the section 2.3.1.2), these variations could be analyzed and summarized as follows: (1) Most of the Raman peaks' intensities were reduced to several tens of arbitrary units after the phase transition temperature, especially the O–Si–O (383 cm^{-1}), carbon chain (854 cm^{-1}), and C–C (1069 cm^{-1}) vibrations, which could imply that thermal damage to the ordered structure occurred via the transition and variations in the vibration and direction of the O–Si–O and Si–C–C bands. It could be speculated that this transition from disordered structure could affect the SERS sensitivity of Ag NP–APTES SAMs system. Moreover, it could also be possible that some vibrations were hidden by disordered and overlapping molecules. (2) For curves a to g, the Raman peaks at 383 and 1069 cm^{-1} show variation trends unlike those of the other Raman peaks. The intensities at 383 cm^{-1} (O–Si–O) and 1069 cm^{-1} (Si–C–C) show nearly no change before the phase change point, whereas the intensity of the other peaks obviously decreased. It could be speculated that the stretching vibration of C–C near Si and O–Si–O were nearly unaffected before the phase change, and the strong SERS signal of this highly Raman-sensitive stretching vibration could be easily found and recorded during heating. (3) The intensities at 1129 cm^{-1} (Si–O–Si), 1402 cm^{-1} (Si–CH_2), and 1604 cm^{-1} (NH_2) decreased after the phase change point, but the peaks did not disappear. These three peaks still appeared in curves h and i, and remained stable after 77 s (curve j). The reason why these peaks did not disappear may be that part of the asymmetric vibration of Si–O–Si and the bending vibration at Si–CH_2 and the NH_2 group were not affected by heat, and these vibrations were too strong to be totally hidden by disordered molecules. Further, considering the high intensity at 1604 cm^{-1} after the phase transition, some amino groups might have remained adsorbed on Ag NPs after the structure changed from ordered to disordered. (4) According to the FWHM in *Figure 2.17* (blue curve), the broadened peaks at 383, 854, 1069, 1129, and 1402 cm^{-1} imply increased intermolecular vibration and disorder inside the monolayer structure. Meanwhile, the FWHM of the 1604 cm^{-1} (NH_2) peak shows no obvious broadening, from which it suggests that the phase transition process did not dramatically affect the majority of amino groups.

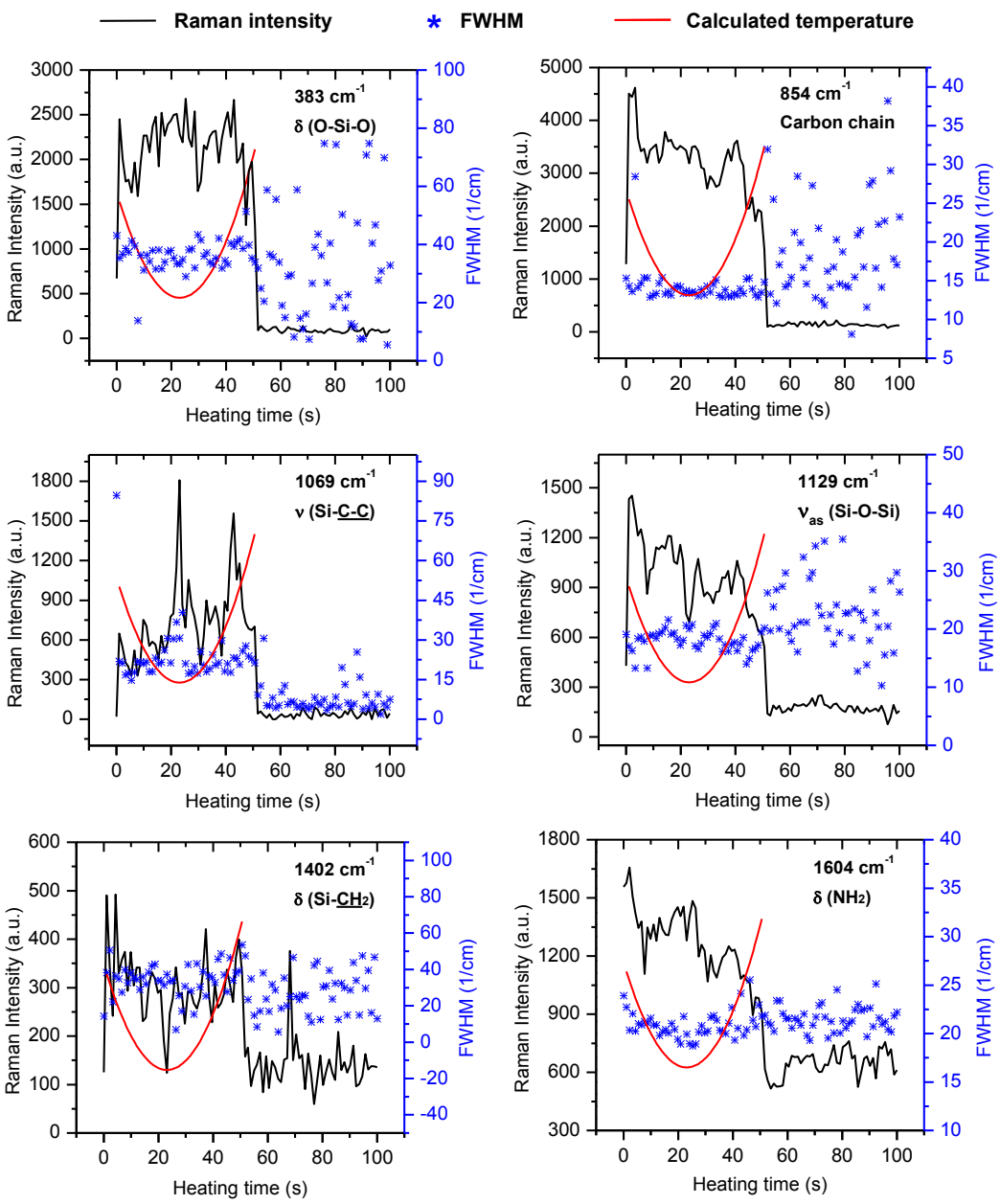

Figure 2.17 Intensity (black) and FWHM (blue) variation at 383, 854, 1069, 1129, 1402, and 1604 cm^{-1} under laser heating. Red curves represent the temperatures' variation along with laser heating, which were calculated by anti-Stokes and Stokes peaks at 854 cm^{-1} in Figure 2.15.

2.3.2.2 In-situ kinetic anti-Stokes and Stokes Raman scattering observation on SLG

The kinetic reactions on SLG basal plane and edge under laser heating are investigated, respectively. *Figure 2.18* (a) and (b) depict the Raman spectrum of the SLG basal plane before and after heating respectively. To gain insight into the dynamic temperature and structure variation along with heating, the anti-Stokes and Stokes Raman spectra of SLG basal plane and the edge were recorded in situ during the heating process. The Raman spectrum shown in curve (a) was measured on a pristine SLG basal plane. Clear G and 2D peaks can be seen at 1595 cm^{-1} at 2700 cm^{-1} respectively. In comparison with curve (a), the curve (b) shows some decrease in the I(2D) peak, most of which may be attributed to heat-induced hole-doping, caused by O2 molecules with a minor contribution from lattice compression. [38]. Another obvious difference between the curves is the increased background between 1100 cm^{-1} and 1600 cm^{-1}. The spectrum in this range can be divided into a G peak and a broad D peak (1380 cm^{-1}). The appearance of a broad D peak is due to the breathing modes of sp2 atoms originated from defects, and an increased I(D)/I(G) ratio reflects an increase in the defect degree. In *Figure 2.18* (c), the black curve represents the ratio, I(D)/I(G), which is a measure of defect generation in SLG. Thus, one may deduce from *Figures 2.18* (a) and (b) that defects on the SLG basal plane were generated by laser heating.

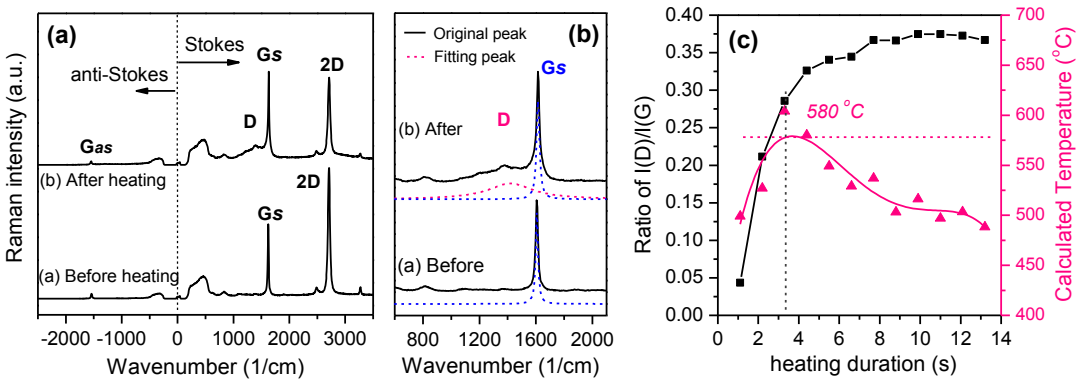

Figure 2.18 (a): Raman spectrum of pristine SLG basal plane; (b) Raman spectrum of SLG basal plane after heating;(c) variation on calculated temperature (red) along with intensity of D peak (black). Gs: Stokes scattering of G peak; Gas: anti-Stokes scattering of G peak.

Furthermore, the same as the section 2.3.2.1, the intensity ratio of anti-Stokes and Stokes Raman scattering is related to the temperature, as described by the equation, "Ias/Is = exp(−hv/kT)". The temperature reached during each heating duration was calculated using this

equation, and the intensity of Gas and Gs peak. The dependence of temperature on the duration of heating was plotted in *Figure 2.18* (c), together with the associated variation in I(D)/I(G). It can be seen that as the heating continued, the temperature rose to 580°C, with a simultaneous increase in I(D)/I(G), which suggests that the defects might have appeared as a result of this heating.

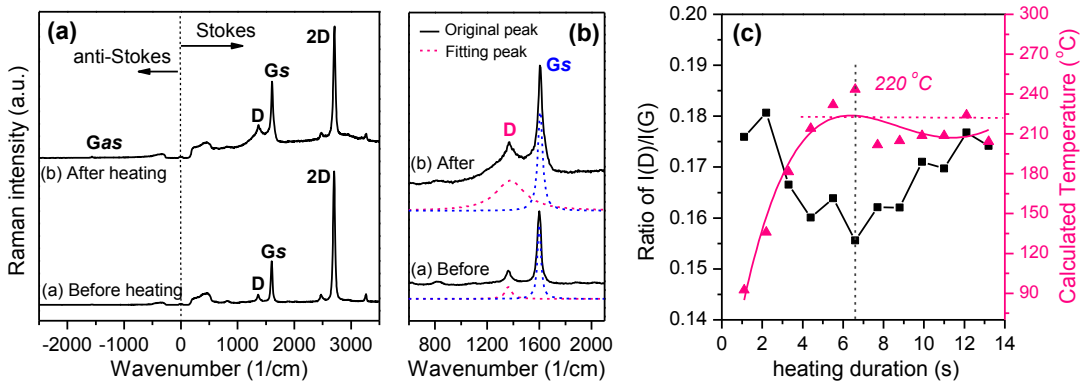

Figure 2.19 (a): Raman spectrum of pristine SLG edge plane; (b) Raman spectrum of SLG edge plane after heating;(c) variation on calculated temperature (red) along with intensity of D peak (black)

The thermal stability of SLG edge plane similarly analyzed based on the results presented in *Figure 2.19*. The defects already present in the unheated pristine SLG edge are indicated by the obvious D peak (*Figure 2.19* (a)). After laser heating, the increase in I(D) and broadening of the peak demonstrate that further defect generation and oxidation had occurred at the SLG edge. The precise D and G peaks were fitted in *Figure 2.19* (b). In the same way as described above for the SLG basal planes, the temperatures were calculated according to the ratio of anti-Stokes and Stokes Raman intensity near the G peak. The variation of temperature and the ratio I(D)/I(G) with the time of heating is shown in *Figure 2.19* (c). Based on the variation of I(D)/I(G) and the temperature on the heating duration dependence, it suggests that further oxidation and defect generation occurred around 220 °C. (The dropping I(D)/I(G) at a lower temperature will be discussed later.) This temperature is much lower than that in the case of the basal plane because of the thermal instability of the SLG edge defects. The difference in the thermal stability of the SLG basal edge and edge has been discussed in previous literature. Nan et al. [9] reported that single-layer graphene showed defects on heating above 500°C in air, indicated by the appearance of a disorder-induced Raman D peak. In addition, Shen et al. [12] showed that graphene edges

are unstable even at temperatures as low as 200°C under annealing in vacuum. Although their results focused on the thermal stability under annealing treatment, while the heating in this study was induced by laser, the thermal effects are similar to each other. It concludes that, in the case of laser induced heating, defects on the SLG basal plane could appear at a temperature over 500°C, but edge plane would show defects at temperatures as low as 200°C.

The detailed variation in the G peak and D peak at SLG basal is further discussed in *Figure 2.20*. As shown in *Figure 2.20*, the elevation in the intensity of G peak (I(G)) and the upshifting of the frequency of G peak (Fre(G)) were observed due to the increase in the amount of sp^2-rich amorphous carbon [39] caused by the heating. The broadening of the FWHM(G) and the simultaneous increase in the I(D) are signals of structural disorder, which was caused by the thermal induced defects [24, 40]. In addition, it was reported that oxygen can bond to SLG point defects even at ambient temperatures in air and would be much easier on heating [41-43]. The oxygen source maybe the polymeric residue of poly(methyl methacrylate) from CVD process and the O_2 from the ambient air. The blue-shifted Fre(G) may be expected to behave identically for the oxygen bond. It implies that the structural disorder was induced by not only the thermal induced defects but also by bonded oxygen.

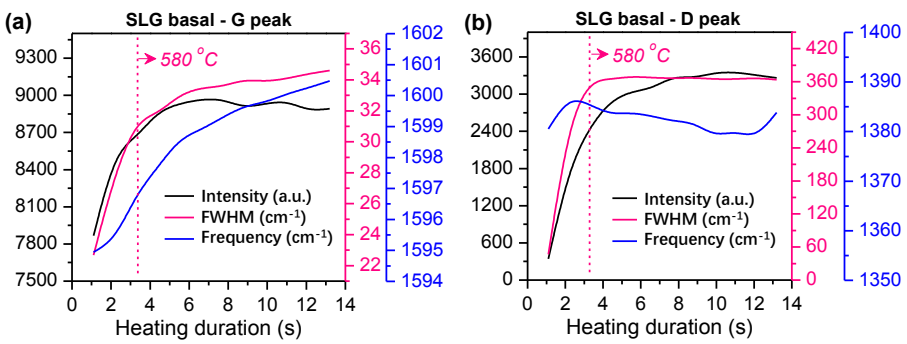

Figure 2.20 Heating duration dependence on the peaks variation at SLG basal plane. (a) G peak (b) D peak

Moreover, the oxygen density could be monitored by considering the inverse relation of I(2D)/I(G) [24]. In accordance with these two hypotheses, the results in *Figure 2.21* (a) indicate that the ratio I(2D)/I(G) reduced from 1.9 to 1.0 as a result of more oxygen and an increase in defects. Consequently, when the SLG basal plane was heated by excitation laser, it caused generation of more and more defects along with oxygen bonded (*Figure 2.21* (b)).

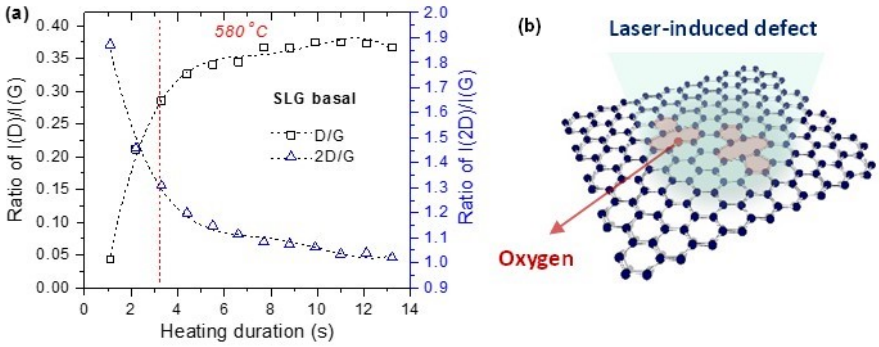

Figure 2.21 Heating duration dependence on the peaks variation at SLG basal plane. (a) ratio of I(D)/I(G) and I(2D)/I(G) (b) Schematic illustration of the defect generation

The dynamic variation of the edge structure was analyzed in the same way. The pristine edge of SLG was identified by the obvious D peak in *Figure 2.19*. The edge of SLG mainly consisted of the Raman active Armchair-edge (A-edge) and the Raman inactive Zigzag-edge (Z-edge). [44-46] The thermal stability of these edges has been demonstrated that the Z-edge is able to endure temperatures of at least 200 °C, and A-edge is more thermally stable than that.

Along with laser heating, the kinetic variation of G peak and D peak was displayed in *Figures 2.22* and *2.23*. At the beginning of the laser heating, the reduced FWHM(G) in *Figure 2.22* (indicating the decreased structural disorder degree) and the reduced I(D)/I(G) in *Figure 2.23* (indicating the decreased defect degree) suggested that the defect density became lower before the temperature reached 220 °C. Since both of A-edge and Z-edge are stable to the temperature of at least 200 °C, the reduced defect density would not be caused by the damage of them. Except for A-edge and Z-edge, there could be many point defects at the pristine edge, since the edge of SLG is chemical active to bond with some oxygen moieties during CVD process. Therefore, the initial point defects, which existed at pristine edge, maybe partially damaged at the low temperature, which resulted in the decreased defect density. Moreover, in *Figure 2.23*, the slight increase in I(2D)/I(G) at the beginning of laser heating also demonstrated the removal of bonded oxygen together with the disappearance of point defects. As the heating duration became longer, all the peaks' profile presented a trend similar to that of the basal plane, that of more defects and oxygen at higher temperatures.

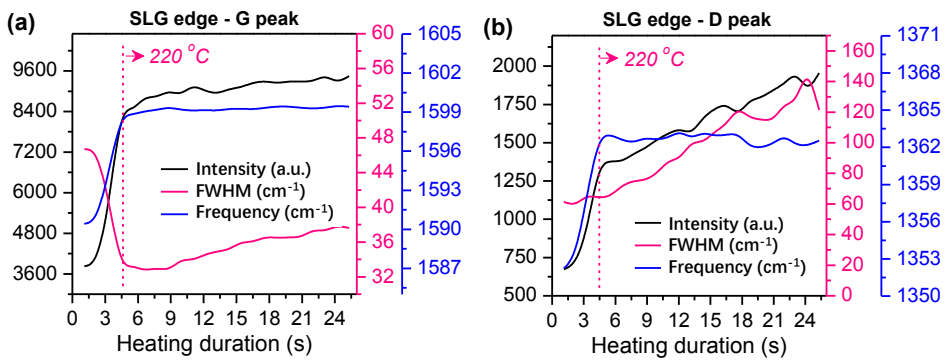

Figure 2.22 Heating duration dependence on the peaks variation at SLG edge plane. (a) G peak (b) D peak

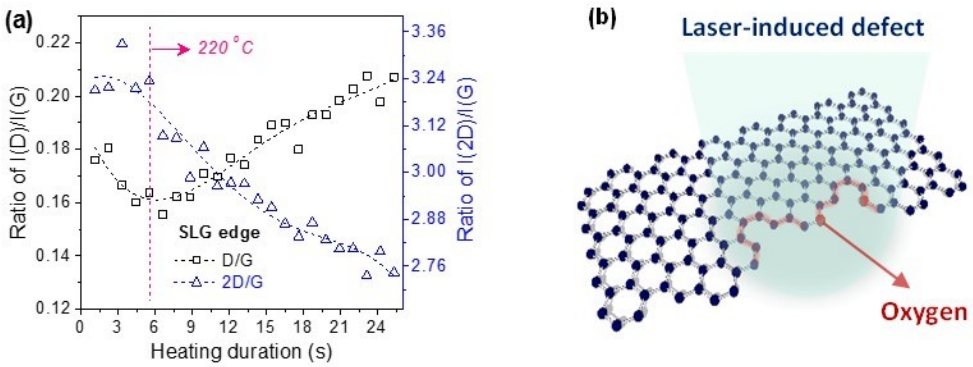

Figure 2.23 Heating duration dependence on peaks variation at SLG edge plane. (a) ratio of I(D)/I(G) and I(2D)/I(G) (b) Schematic illustration of the defect generation

The thermal stability of SLG edge can be summarized as follows: The point defect at edge is more thermally unstable than other defects at the temperatures lower than 220 °C. As the temperature keep increasing, more defects would be formed again due to the thermal instability of edge at high temperatures. According to these results, the thermal damage of edge plane caused by laser irradiation display the similar behavior as the thermal damage by other methods.

This study examined the thermal stability of SLG basal and edge plane under laser irradiation. The thermal dynamics of defect is significant to understand and control the defect density, which is important to the industrial application. Simultaneously, it demonstrates the ability of the time-resolved observation on nano-film by using anti-Stokes and Stokes Raman spectroscopy.

2.4 Summary and conclusion

This chapter successfully demonstrate the ability of SERS for realizing the accurate depth profile at atomic level with a piezo field gradient device, and analyzing the kinetical observation on nano-film materials APTES SAMs and SLG.

Firstly, the precise depth profile on APTES SAMs was realized. The AFM images demonstrate the nano-film structure of APTES SAMs layers with thickness around 20 nm (with Ag NPs deposited) and 1.5 nm (without Ag NPs deposited). Raman measurement results show that the normal Raman peaks could not be observed in such a thin layer structure. Fortunately, combining with the Ag NPs SERS sensor, the enhanced Raman signals could be recorded clearly, which illustrated that SERS would be significant technique for further analyzing the internal structure of nano-film materials. Moreover, SERS was employed to vertically distinguish some significant vibrations of the internal molecular structure of APTES SAMs, such as Ag–N, CH_2, Si–O, and so on. The depth profiling results demonstrate that the prepared APTES SAMs sample comprised multilayers and that this APTES SAMs was inhomogeneous. Furthermore, some frequency shifts occurred during depth profiling and could be analyzed to discuss bonded behaviors at the interfaces. The observed results suggest that not every APTES moiety was bonded with each other, free and bonded Si–O band existed at the same time. Some hydrogen bonds maybe formed on amines at the substrate surface and/or some of the molecules aligned towards the substrate surface with the head and tail groups because of the bent moieties. In conclusion, SERS was used for obtaining accurate depth profile and elucidating the distinction of molecular structure inside APTES SAMs, to the atomic level.

Besides, the kinetic phase transition under laser heating was studied by using surface-enhanced anti-Stokes and Stokes Raman scattering. The phase transition process of APTES SAMs was monitored kinetically. From the relationship between Ias/Is and temperature, the dynamic temperature as a result of laser heating was calculated. It suggests that the structure of APTES SAMs changed from ordered crystalline to disordered at around 118 °C. Furthermore, the results reveal the phase transition process in detail. The thermal damage may be primarily responsible for the variation in the O–Si–O, Si–C–C and carbon chain, and the Si–O–Si bands, the bending vibration at Si–CH_2. The NH_2 group still showed high SERS sensitivity after the phase transition.

Finally, the kinetic surface reaction was investigated on SLG basal plane and edge plane under excitation laser heating. By using anti-Stokes and Stokes Raman spectroscopy, the kinetic

Raman spectra were obtained along with laser heating. It demonstrates that point defects and oxygen bond on SLG basal plane would appear above 500 ºC, but that the edge plane shows thermal instability at temperatures as low as 220 ºC. This phenomenon is similar to the defect generated by annealing treatment. In addition, defect evolution and oxygen bond at SLG basal and edge plane was considered and compared as well. At SLG basal plane, the oxygen bond increased in pace with defect increasing. However, at SLG edge plane, point defects were eliminated at low temperature.

In conclusion, these result indicate the high sensitivity of SERS and Raman spectroscopy for analyzing the thin-film materials. Using an appropriate SERS sensor, the depth profile on internal layer structure can be measured at atomic level, and the kinetic reaction of ultra-thin layer can be precisely monitored. It suggests that SERS has high potential to be used in the interfacial analysis, with a well-designed SERS sensor. For application, the interfacial analysis on SEI formation in Li-ion battery is carried out using SERS and explained in following chapters 3 and 4.

References

[1] C. D'Andrea, F. Neri, P.M. Ossi, N. Santo, S. Trusso, Nanotechnology, 20 (2009) 245606.

[2] S. Nie, S.R. Emory, Science, 275 (1997) 1102-1106.

[3] B. Jiang, T. Ouchi, N. Shimano, A. Otomo, M. Kunimoto, M. Yanagisawa, T. Homma, Electrochimica Acta, 100 (2013) 317-320.

[4] V. Subramanian, W.J. van Ooij, CORROSION, 54 (1998) 204-215.

[5] J. Kim, J. Cho, P.M. Seidler, N.E. Kurland, V.K. Yadavalli, Langmuir, 26 (2010) 2599-2608.

[6] H.J. Martin, K.H. Schulz, J.D. Bumgardner, K.B. Walters, Langmuir, 23 (2007) 6645-6651.

[7] Z. Haiqing, Q. Caiyu, Y. Fang, Y. Huaichao, C. Minjiang, H. Lijun, G. Yanjun, S. Lianfeng, Journal of Physics D: Applied Physics, 44 (2011) 185404.

[8] S. Ryu, L. Liu, S. Berciaud, Y.-J. Yu, H. Liu, P. Kim, G.W. Flynn, L.E. Brus, Nano Letters, 10 (2010) 4944-4951.

[9] H.Y. Nan, Z.Y. Ni, J. Wang, Z. Zafar, Z.X. Shi, Y.Y. Wang, Journal of Raman spectroscopy, 44 (2013) 1018-1021.

[10] D. Abdula, T. Ozel, K. Kang, D.G. Cahill, M. Shim, The Journal of Physical Chemistry C, 112 (2008) 20131-20134.

[11] P.A. Denis, F. Iribarne, The Journal of Physical Chemistry C, 117 (2013) 19048-19055.

[12] Y.N. Xu, D. Zhan, L. Liu, H. Suo, Z.H. Ni, T.T. Nguyen, C. Zhao, Z.X. Shen, ACS Nano, 5 (2011) 147-152.

[13] D. Zhan, L. Liu, Y.N. Xu, Z.H. Ni, J.X. Yan, C. Zhao, Z.X. Shen, Scientific reports, 1 (2011) 12.

[14] L.M. Malard, M.A. Pimenta, G. Dresselhaus, M.S. Dresselhaus, Physics Reports, 473 (2009) 51-87.

[15] D. Graf, F. Molitor, K. Ensslin, C. Stampfer, A. Jungen, C. Hierold, L. Wirtz, Solid State Communications, 143 (2007) 44-46.

[16] X. Jia, J. Campos-Delgado, M. Terrones, V. Meunier, M.S. Dresselhaus, Nanoscale, 3 (2011) 86-95.

[17] A.C. Ferrari, D.M. Basko, Nature Nanotechnology, 8 (2013) 235-246.

[18] B. Tang, G. Hu, H. Gao, Applied Spectroscopy Reviews, 45 (2010) 369-407.

[19] A.C. Ferrari, Solid State Communications, 143 (2007) 47-57.

[20] L.G. Cançado, A. Jorio, E.H.M. Ferreira, F. Stavale, C.A. Achete, R.B. Capaz, M.V.O. Moutinho, A. Lombardo, T.S. Kulmala, A.C. Ferrari, Nano Letters, 11 (2011) 3190-3196.

[21] A.J. Pollard, B. Brennan, H. Stec, B.J. Tyler, M.P. Seah, I.S. Gilmore, D. Roy, Applied

Physics Letters, 105 (2014) 253107.

[22] M.S. Dresselhaus, A. Jorio, A.G. Souza Filho, R. Saito, Philosophical Transactions of the Royal Society a-Mathematical Physical and Engineering Sciences, 368 (2010) 5355-5377.

[23] M. Kalbac, A. Reina-Cecco, H. Farhat, J. Kong, L. Kavan, M.S. Dresselhaus, ACS Nano, 4 (2010) 6055-6063.

[24] C. Casiraghi, S. Pisana, K.S. Novoselov, A.K. Geim, A.C. Ferrari, Applied Physics Letters, 91 (2007) 233108.

[25] A. Taglietti, C.R. Arciola, A. D'Agostino, G. Dacarro, L. Montanaro, D. Campoccia, L. Cucca, M. Vercellino, A. Poggi, P. Pallavicini, L. Visai, Biomaterials, 35 (2014) 1779-1788.

[26] M. Frisch, G. Trucks, H.B. Schlegel, G. Scuseria, M. Robb, J. Cheeseman, G. Scalmani, V. Barone, B. Mennucci, G. Petersson, Inc., Wallingford, CT, 200 (2009).

[27] C. Lee, W. Yang, R.G. Parr, Physical Review B, 37 (1988) 785-789.

[28] A.D. Becke, The Journal of Chemical Physics, 98 (1993) 5648-5652.

[29] W.J. Hehre, Ab initio molecular orbital theory, Wiley-Interscience, 1986.

[30] P.J. Hay, W.R. Wadt, The Journal of Chemical Physics, 82 (1985) 299-310.

[31] J. Tomasi, B. Mennucci, R. Cammi, Chemical reviews, 105 (2005) 2999-3094.

[32] M. Zhu, M.Z. Lerum, W. Chen, Langmuir, 28 (2012) 416-423.

[33] C.-H. Chiang, H. Ishida, J.L. Koenig, Journal of Colloid and Interface Science, 74 (1980) 396-404.

[34] C.B. Samantaray, J.T. Hastings, Journal of Vacuum Science & Technology B, 29 (2011) 041603.

[35] J.A. Howarter, J.P. Youngblood, Langmuir, 22 (2006) 11142-11147.

[36] T.V. Elaine, B. Lars, L. Bo, U. Kajsa, E. Ragnar, E. Hans, L. Ingemar, J. Colloid Interface Sci. , 147 (1991) 103-118.

[37] J. Kim, P. Seidler, L.S. Wan, C. Fill, Journal of Colloid and Interface Science, 329 (2009) 114-119.

[38] J. Hong, M.K. Park, E.J. Lee, D. Lee, D.S. Hwang, S. Ryu, arXiv preprint arXiv:1310.8039, (2013).

[39] D.L. Baptista, F.C. Zawislak, Diamond and Related Materials, 13 (2004) 1791-1801.

[40] A.C. Ferrari, Solid State Communications, 143 (2007) 47-57.

[41] F. Mehmood, R. Pachter, W. Lu, J.J. Boeckl, The Journal of Physical Chemistry C, 117 (2013) 10366-10374.

[42] A. Cagliani, N. Lindvall, M.B.B.S. Larsen, D.M.A. Mackenzie, B.S. Jessen, T.J. Booth, P. Boggild, Nanoscale, 7 (2015) 6271-6277.

[43] L. Liu, S. Ryu, M.R. Tomasik, E. Stolyarova, N. Jung, M.S. Hybertsen, M.L. Steigerwald, L.E. Brus, G.W. Flynn, Nano Letters, 8 (2008) 1965-1970.

[44] R. Saito, A. Jorio, A.G. Souza Filho, G. Dresselhaus, M.S. Dresselhaus, M.A. Pimenta, Physical Review Letters, 88 (2001) 027401.

[45] C. Thomsen, S. Reich, Physical Review Letters, 85 (2000) 5214-5217.

[46] M.A. Pimenta, G. Dresselhaus, M.S. Dresselhaus, L.G. Cancado, A. Jorio, R. Saito, Physical Chemistry Chemical Physics, 9 (2007) 1276-1290.

Chapter 3: Kinetic observation on SEI formation in Li-ion battery

3.1 Introduction

Chapters 3 and 4 describe the interfacial analysis of LIB by using SERS. The target is to observe the crucial but unclear structure in LIB, the solid-electrolyte interface (SEI). To the present, many approaches have been employed to investigate the chemical, electrochemical and structural properties of the SEI film, including scanning electron microscopy (SEM), X-ray photoelectron spectroscopy (XPS), Fourier transform infrared spectroscopy (FTIR), time-of-flight secondary ion mass spectroscopy (TOF-SIMS) and electrochemical impendence spectroscopy (EIS), many of which have been reviewed by Balbuena et al. [1] and Verma et al. [2]. However, SEI film is still not deeply understood and plenty of controversies exist among the diverse researches. SERS has been demonstrated to be a powerful technique for the interfacial analysis. It can provide the information of molecular vibration, which is different from other approaches. Therefore, in this chapter, to supply more comprehensive view of the SEI film, the in-situ kinetic formation of SEI film is investigated by using SERS.

From many experimental investigations and theoretical calculations, the possible reduction pathway of electrolyte could be generally summarized as the decomposition of cyclic carbonate solvent, including alkyl-oxygen cleavage [3] and acyl-oxygen cleavage [4]. No matter in which hypothesis, electrolyte solvent was always considered to play an important role in the interfacial reaction.

Cyclic carbonates (such as Propylene carbonate (PC), Ethylene carbonate (EC)) and acyclic carbonates (such as Ethyl methyl carbonate (EMC), Dimethyl carbonate (DMC)) are fundamental components of electrolyte solvent. Cyclic carbonates were usually used to dissolve the lithium salt (such as $LiPF_6$, $LiClO_4$) because of their polarity. Acyclic carbonates cannot be omitted to be a co-solvent owing to their low viscosity for diluting the high-viscous cyclic carbonates and elevating the Li^+ ion conductivity. During the electrochemical reduction process (SEI formation process), there might be an unequal opportunity for these two types of solvents to react on the anode surface. Tasaki et al. [5] studied DFT calculations of solvent decomposition in solution and Molecular dynamics (MD) simulations of the decomposition compounds, and listed the ease of one-electron reduction as follows: EC > PC > VC > DMC > EMC > DEC, with EC and PC being the more likely reduced than acyclic carbonates. The preferential reduction was also reported by some experimental studies. Zhuang et al. [6], Xu et al [7] and Vatanamu et al. [8] investigated the preferential reduction of cyclic carbonates and acyclic carbonates by using FTIR, Nuclear magnetic resonance (NMR) and (MD) simulations. It was demonstrated that the SEI film formed

on Graphite anode surface was dominated by the reduction of cyclic carbonates even when the cyclic carbonates proportion was at low level. Consequently, the cyclic carbonates are the significant component during the formation of the SEI film.

In this chapter, to investigate the kinetic formation of SEI film, the studies are focused on the comparison of EC and PC, because PC was demonstrated to form the SEI film with bad performance. The investigation of the difference between EC and PC may lead to a new insight into understanding the interfacial reaction for SEI formation.

Raman spectroscopy and Surface-enhanced Raman spectroscopy (SERS) are appropriate to observe the interfacial reaction, owing to the merits of in-situ measurement and observing the molecular vibration. Moreover, SERS can provide the molecular vibration at the range of wavenumber from 100 ~ 4000cm^{-1} that hardly observed by other methods. However, there are very few SERS studies on SEI film till present. In order to observe the trace products in the SEI film, the SERS sensors were specially designed for the measurement on liquid-solid interface. To realize the in-situ kinetic measurement, an electrochemical cell was set up. For the kinetic area monitoring, a Raman spectroscopy installed with multi-laser spots was employed. Taking advantage of these techniques, the kinetic monitoring of SEI formation was investigated.

3.2 Experimental section

3.2.1 Samples and materials

Graphite anode: Mesocarbon microbeads (MCMB) graphite powder was coated on a Copper foil, purchased from MTI Corporation; Cathode: $LiCoO_2$ thin film was deposited on the flat surface of a silver foil, purchased from MTI Corporation.

For analyzing the formation of SEI film, 1M $LiPF_6$ was dissolved in PC-EMC (1:1 v/v) mixed solvent and EC-EMC (1:1 v/v) mixed solvent, respectively, to prepare the electrolyte solution. In following expression, the electrolyte solution with 1M LiPF6 dissolved will be designated as Li-PC-EMC and Li-EC-EMC.

For distinguishing the kinetic reaction on the basal and edge of graphite, HOPG (Highly oriented pyrolytic graphite) was chosen to be anode, which was purchased from ALLIANCE Biosystems, Inc. The distinguishable structure of the basal and edge plane allows comparing the different reaction on these two structures, during the formation of SEI film.

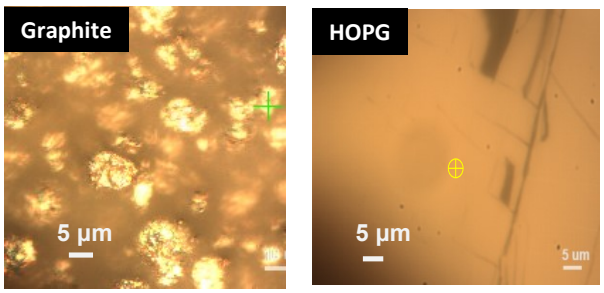

Figure 3.1 Optical image of the morphology of graphite and HOPG

3.2.2 Raman spectroscopy

Single laser spot

In order to determine the composition of SEI film during the formation process, SERS studies were conducted. A confocal Raman spectroscopy with a laser of 532 nm was used for the in-situ measurement and SERS. The Raman spectra of standard samples, SERS spectra of SEI film thermal stability of SEI film and kinetic observation during SEI film formation were

measured using single-laser spot.

Multi laser spots

The real-time area monitoring was also investigated during SEI film formation by the Raman spectroscopy that installed with multi-laser spot. As shown in *Figure 3.2*, the multi-laser spots support the simultaneous monitoring on a square area of sample surface and recording 121 Raman spectra in single measurement, by 11 x 11 laser spots matrix. The diameter of each laser spot was aound 1 - 2 μm. The laser power of each spot was about 3 mW to avoid the affection on the interfacial reaction by the heat energy.

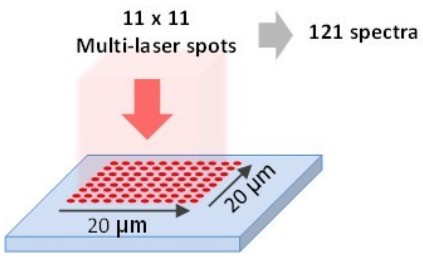

Figure 3.2 Schematic illustration of area monitoring with multi-laser spots

3.2.3 SERS sensor

As introduced in section 1.1.2.2 and *Figure 1.4*, Ag NPs was considered to be SERS sensor in this chapter, since the excitation laser was 532 nm. SERS sensors with various structures were fabricated to be the candidates for observing SEI film. The schematics of these sensors are shown in *Figure 3.3*, (a) Ag NPs deposited on micro lens array structure with pyramid-like substrate, designated as MLA sensor; (b) Ag NPs deposited on flat substrate, designated as Flat sensor; (c) Ag NPs deposited on convex substrate with Al_2O_3 coating film, designated as Convex sensor. The MLA sensor was fabricated and supplied by Master Nakamura, with the substrate of Polydimethylsiloxane (PDMS) and pyramid-pattern of 30 μm. The Flat sensor was provided by Kyodo International Inc., with Ag film thickness of 5 nm. The structure and fabrication of sensor (c) was the same as that reported by Yanagisawa et al. [9]. The substrate is convex lens (quartz) with the diameter of 2 mm and the thickness of 0.8 mm. The Ag NPs Nanoparticles were sputtered on the convex surface with the diameter of 50 nm and then an Al_2O_3 film with the thickness of 1nm was deposited on the surface of Ag NPs, to protect the corrosion of Ag NPs from electrolyte solution. These three sensors were tested on HOPG surface to identify the best SERS enhancement.

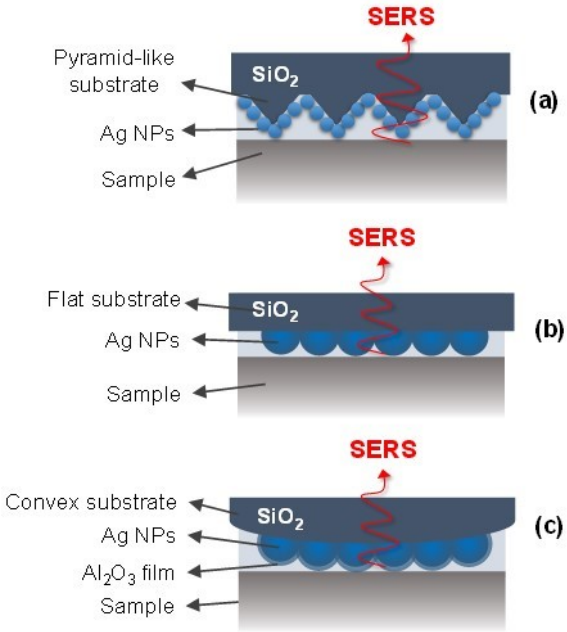

Figure 3.3 The structure of three SERS sensors. (a) Ag NPs deposited on micro lens array structure with pyramid-like substrate, designated as MLA sensor; (b) Ag NPs deposited on flat substrate, designated as Flat sensor; (c) Ag NPs deposited on convex substrate with Al_2O_3 coating film, designated as Convex sensor.

3.2.4 Cell set up for the in-situ SERS measurement and electrochemical reaction

An electrochemical cell was designed for the in-situ observations. The cell was assembled and sealed in Ar-filled glove box with graphite as the working electrode (W.E.) and $LiCoO_2$ as the counter electrode (C.E.) and reference electrode (R.E.). See the *Figure 3.4* for the schematic of the cell structure. Two electrodes were located on the two Cu current collectors which were connected with electricity. Electrolyte solution was flowed into LIB model cell through electrolyte inlet and outlet. After filling the space inside cell, the cell was well sealed by a glass cap, PMP cover window and two screwcaps on electrolyte inlet and outlet. There was a short space between electrode and PMP cover window. The flexible PMP film can press the SERS sensor to contact electrode surface, which would be crucial for generating SERS hotspot. This PMP window was tested and demonstrated that it would not influence the Raman signals from inside electrolyte and electrode via the depth profiling in *Figure 3.5*. This cell would be useful to simulating and observing the kinetic reaction that is difficulty to be measured from industrial LIB.

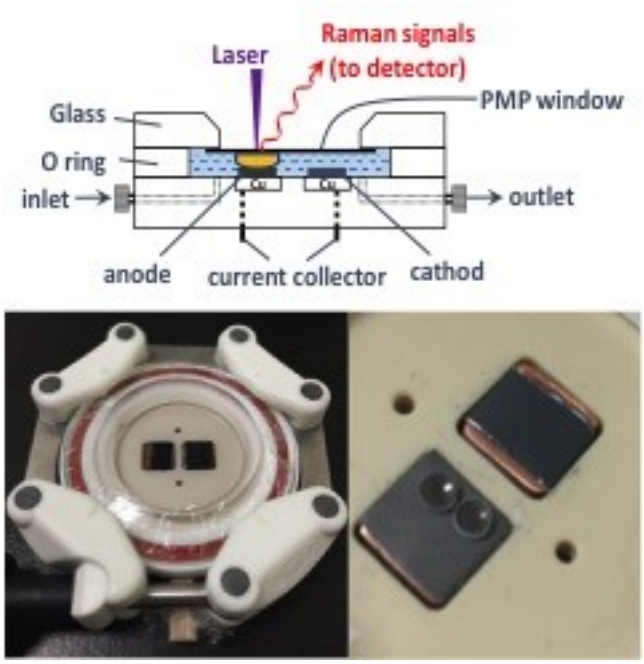

Figure 3.4 Schematic of LIB model cell (above); the photographs of LIB model cell and the SERS sensor placed on graphite anode (below)

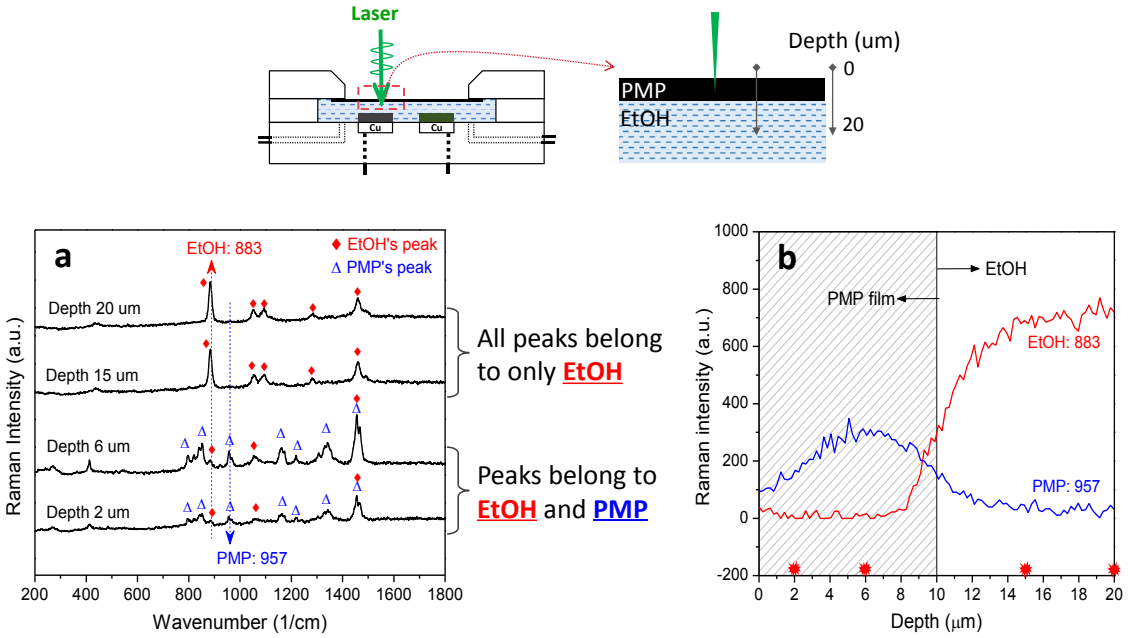

Figure 3.5 Examine the influence of PMP film on detecting internal electrolyte. a. Raman spectra at four vertical positions; b. Depth profile on the interface of PMP film and internal ethanol at 883 and 957 cm^{-1}

3.2.5 Formation of SEI film

Cyclic voltammetry (CV) was conducted for SEI film formation, with the voltage range from -3.0 V to 3.0 V and the scan rate of 0.5 mV/s. Two electrode system was chosen, graphite as working electrode (W.E.) and $LiCoO_2$ as counter electrode (C.E.) and reference electrode (R.E.). There was no special reference electrode because the traditional Li metal reference electrode has difficulty to be used in our electrochemical cell, and the accurate monitoring of the electrochemical reaction is not necessary in this study.

3.3 Results and discussion

3.3.1 Raman spectra of standard samples and frequency assignment

First of all, the Raman spectra of standard electrolyte solvents were detected and the various assignments were figured out according to the reference studies [10] and DFT calculation. The spectra are displayed in *Figure 3.6* and *Figure 3.7*. The assignments are listed in *Table 3.1*. The assignments will support the peak analysis in chapters 3 and 4.

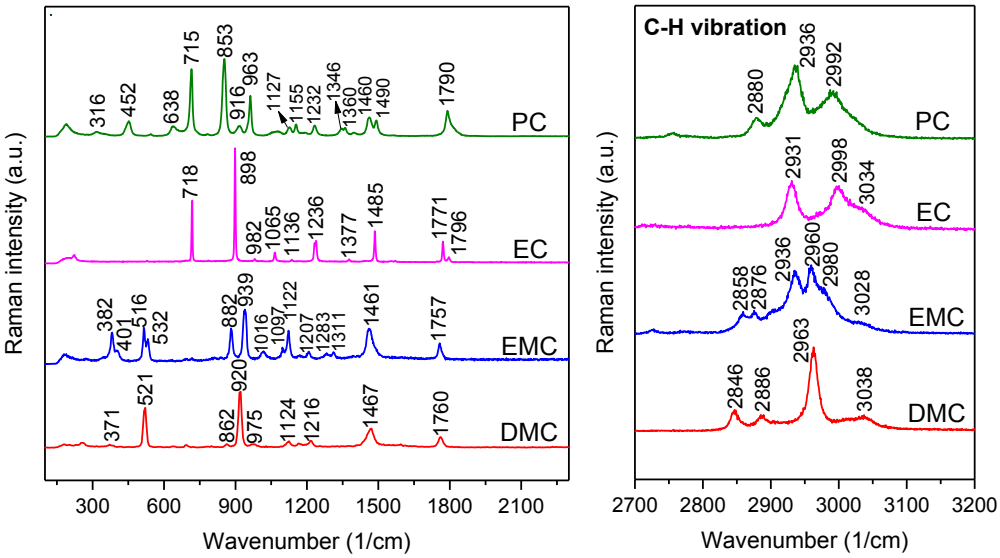

Figure 3.6 Raman spectra of pure PC, EC, EMC and DMC

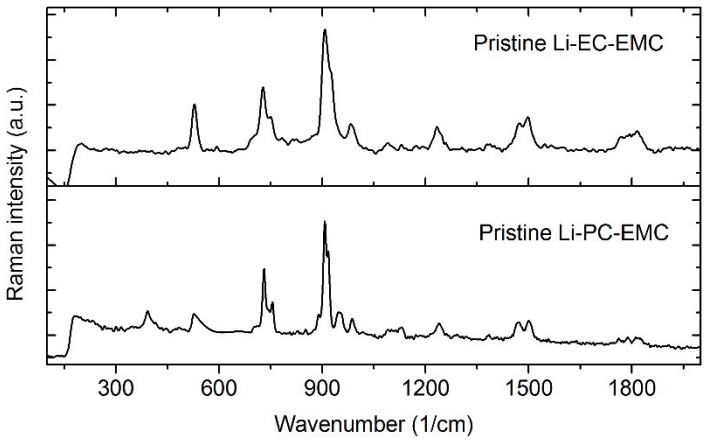

Figure 3.7 Raman spectra of pristine Li-PC-EMC and Li-EC-EMC

Table 3.1 Frequencies and assignments of pure EC, PC, EMC and DMC

Frequencies (cm^{-1})			**Assignments** (DFT calculation)
EC	PC	EMC	
	316		CH_3
		382	CH_2-CH_3
		403	CH_2-CH_3
	452		C-C-C
		515	O-C-O scissoring
	638		C-C
			Skeleton deformation
718	715		C-O scissoring
898	853		Ring breathing
		883	C-O stretching, C-H wagging
	916	939	O-C-O, CH_3, CH_2, C-C
982	963		CH_3-CH_3 stretching
			O-CH_3 stretching
		1018	O-C-C asymmetry stretching
1065			Ring in-plane stretching
		1122	C-H wagging
			O-CH_3 stretching, O-C-O scissoring
1136	1127		Ring in-plane deformation
	1155		C-H wagging
1236	1232	1207	C-H twisting
	1346		C-H wagging
1377	1360		C-H wagging
	1460	1461	C-H scissoring
1485	1490		C-H scissoring
1771		1757	C=O stretching
1796	1790		C=O stretching

3.3.2 Formation of SEI film

3.3.2.1 Cyclic voltammetry

The voltammetric behaviors of graphite anode vs $LiCoO_2$ cathode in Li-PC-EMC and Li-EC-EMC over voltage window -3.0 to 3.0 V are shown in *Figure 3.8.* SEI film could be formed mostly during the first charging cycle. After the second cycle, the SEI film is tending toward stability. The voltammetric behavior of graphite electrodes in Li-PC-EMC and Li-EC-EMC containing lithium salts has already been studied and discussed extensively in half-cell models [6, 7, 11]. In general, the onset potential of electrolyte reduction on graphite electrodes (vs Li metal electrode) is most widely adopted at 0.8~1.0 V, which is also shown in the cyclic voltammetry of this study in *Figure 3.8*. The electrochemical measurement was conducted in full-cell model, using the two electrode system, because the in-situ cell is not sufficient to allow using the Li metal reference electrode in air atmosphere. Therefore, the potential was not precisely controlled due to the polarity of counter electrode $LiCoO_2$. Although PC has been used as traditional polar solvent in LIB years ago, it is agreed to be not as good as EC does on forming stable SEI film with some controversial reasons expressed in Chapter 1. A kinetic observation on the formation of SEI film is meaningful to find the difference between EC-based electrolyte and PC-based electrolyte.

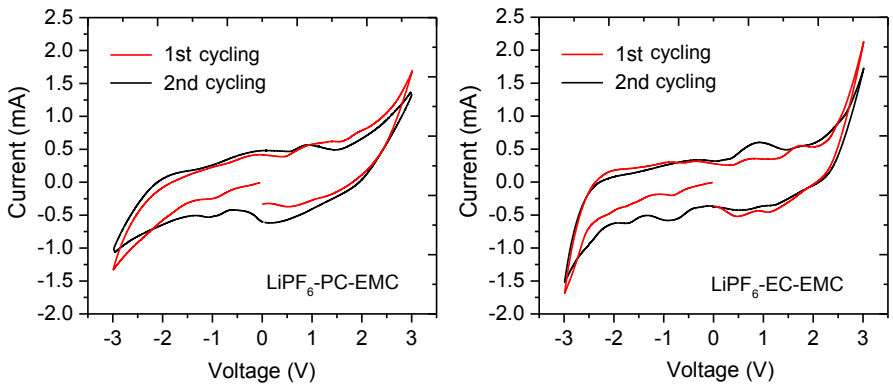

Figure 3.8 First and second consecutive cyclic voltammograms for graphite electrodes vs $LiCoO_2$ cathode in 1 M $LiPF_6$ solutions with EC-EMC and PC-EMC. The voltammograms were recorded at room temperature 24°C with a scan rate of 0.5 mV/s.

3.3.2.2 Stability of SEI under laser heating

Thermal stability can also indicate the performance of SEI film. Theoretically, a compact SEI film should show higher stability than a loose SEI film. In this study, SEI films were measured in Li-PC-EMC and Li-EC-EMC after four charging cycles. With laser (laser power of 30 mW) continuously irradiated on the SEI films, the in-situ kinetic Raman spectra were measured on these SEI film, respectively. The measurement was carried out without using SERS sensor to avoid the thermal damage to the nanoparticle structure on the surface of sensor, which may further influence the detected Raman peaks. The series of Raman spectra are shown in *Figure 3.9*, with the dash lines marking the peaks from graphite and the grey areas highlighting the peaks from SEI film. In graph (a), the peaks of the SEI film formed from Li-PC-EMC are eliminated no longer than 5s, due to the thermal damage by laser irradiation. Simultaneously, peaks of graphite are rather weak at the initial stage of SEI film, which may be caused by a certain exfoliation from PC. Relatively. in graph (b), the SEI film formed from Li-EC-EMC can endure the laser heating at least 2000s. It also supports that EC-based electrolyte can form better SEI film than PC-based electrolyte, which corresponds to the previous research.

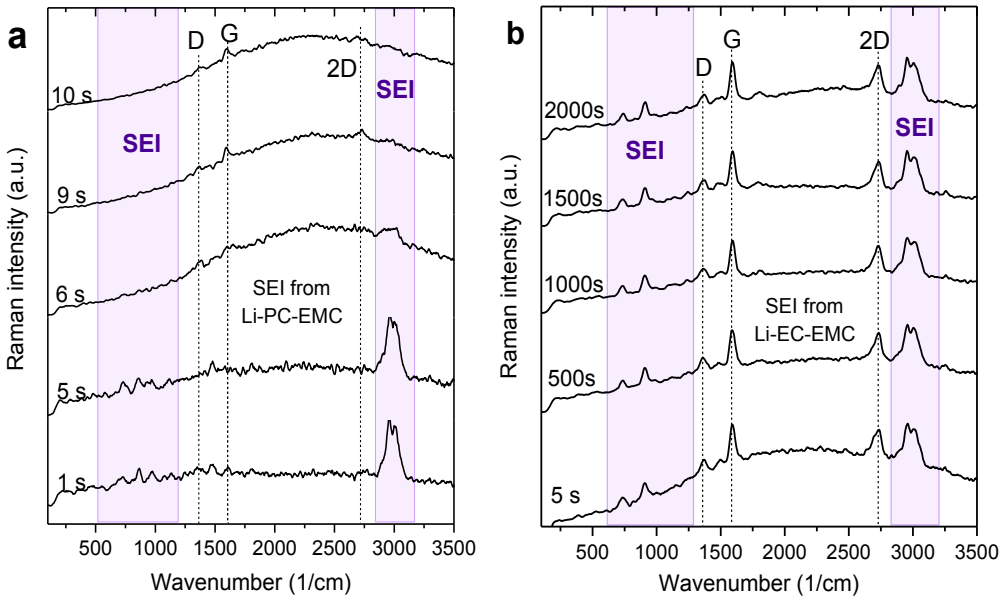

Figure 3.9 Thermal stability of SEI layer formed in (a) Li-PC-EMC and (b) Li-EC-EMC

3.3.3 Kinetic observation on SEI formation by single laser spot

3.3.3.1 Appropriate SERS sensor for graphite material

Normal Raman spectroscopy cannot observe much difference of SEI film formed in EC-based electrolyte and PC-based electrolyte. The components of organics and inorganics are also difficulty to distinguished, since many inorganics peaks are overlapped by the Raman scattering of organics. As explained in the experimental section, SERS sensors were fabricated to solve this issue via the sensitive SERS enhancement. There are three SERS sensors were tested in this chapter, the MLA, Flat sensor and convex sensor. HOPG was used as probe to test the sensitivity of these three SERS sensors. *Figure 3.10* is the SERS spectra of HOPG, measured with three SERS sensors. The MLA sensor and Flat sensor show week G peaks of HOPG, while relative strong G peak can be detected using Convex sensor.

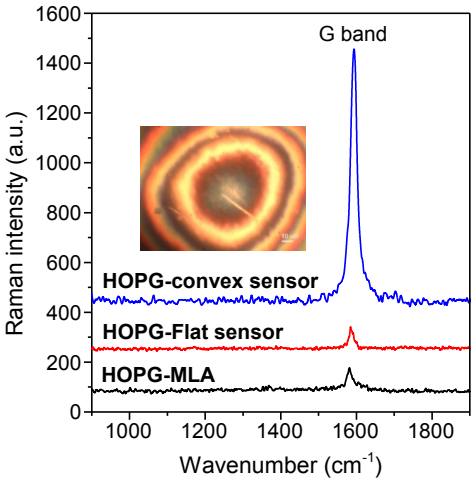

Figure 3.10 SERS spectra measured at the surface of HOPG with three types of SERS sensors. Laser wavelength: 532 nm; Exposure time: 1s.

To generate SERS hotspot, the narrow gap between metal NPs and sample play a key role, which means the contact point of SERS sensor on sample is crucial. The substrate of MLA is PDMS, a flexible material, which makes the sensor hardly to contact HOPG surface. The substrate of Flat sensor is SiO_2 wafer. The hard and flat substrate could contact to somewhere of HOPG surface, but the contact point is difficulty to find out. The Convex sensor may contact with HOPG

surface at the center of convex SiO_2 substrate. The contact point can be easily found from the newton ring pattern (the optical image in *Figure 3.10*). Therefore, in this study, Convex sensor was chosen to observe the SERS spectra of SEI film.

3.3.3.2 Kinetic SEI formation on graphite anode in Li-EC-EMC

SERS sensor was used on the surface of graphite for the kinetic measurement on SEI formation. The SERS sensor was pressed to contact the graphite surface, so that the gap between SERS sensor and graphite is limit for forming SERS film. However, the rough particle structure allows the possibility of SEI film formed at the gap between the SERS sensor and graphite. To avoid the thermal damage by laser irradiation, the laser power was reduced to around 3 mW and the exposure time for single measurement was expanded to 10 s.

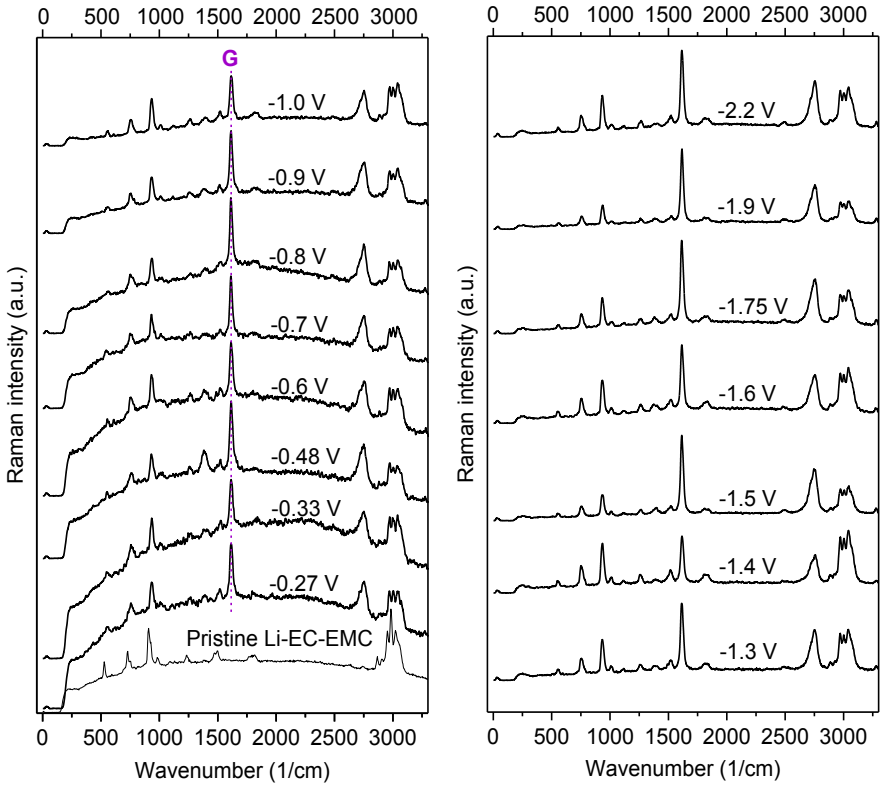

Figure 3.11 Kinetic SERS spectra during the formation of SEI film in Li-EC-EMC from the voltage of -0.27 V to -2.2 V

Figure 3.11 is the kinetic SERS spectra at the interface of electrolyte and graphite surface during the first charging cycle. A Raman spectrum of pristine Li-EC-EMC is also displayed for

comparison. The nature potential measured on the working electrode of graphite (vs $LiCoO_2$) is around -0.2 V. Along with the negative voltage changing, a series of in-situ Raman spectra was continuously recorded from the voltage of -0.27 V to -2.2 V, which involves the main electrolyte decomposition. Comparing to the Raman peaks of pristine electrolyte, there are some variations of peaks' intensity caused by interfacial reaction, such as the peak of O-C-O of organics around 510 cm^{-1}, C-H peaks around 3000 cm^{-1} and so on, but no obvious new peak is observed. Another apparent phenomenon is the fluorescent background of electrolyte, which due to the Li-EC solvation (coordination complex) [12], start to decrease from 0.8 V. The Raman spectra were detected at the solid-liquid interface, so that the fluorescence from liquid electrolyte is unavoidable. The decrease in fluorescent background may result from the decomposition of Li-EC solvation and the low fluorescent products (constitute SEI film) by the interfacial reaction. The more products generated from electrolyte reduction, the lower fluorescence could be detected.

3.3.3.3 Kinetic SEI formation on graphite anode in Li-PC-EMC

The kinetic SEI formation in Li-PC-EMC was observed in the same way (*Figure 3.12*). Different from the result of Li-EC-EMC, the fluorescent background remains all the time. PC-based electrolyte was believed to generate loose SEI film. The low density ratio of SEI products at the interface maybe one of the reason why the fluorescence from electrolyte still influence the observed spectra. Moreover, there is another difference comparing to EC-based electrolyte. Other than the Raman peaks from regular organic component, a new peak appear at the lower wavenumber than 300 cm^{-1} starting from the negative voltage lower than -0.9 V. Since the signals were cut off around 250 cm^{-1} by the notch filter, the entire peak cannot be displayed. This peak is most possible to be attributed to inorganic compounds Li_2CO_3, according to the Raman frequency observed on pure Li_2CO_3 crystal and other references [1, 13]. As a comparison, the Raman spectrum of pure Li_2CO_3 reported by other reference is shown in *Figure 2.12* (a), the SERS and Raman spectra of pure Li_2CO_3 crystal using convex sensor observed in this study is shown in *Figure 2.13* (b). Using convex sensor, only the peaks at low wavenumber could be detected. Besides, since the peaks of Li_2CO_3 at the range from 300 to 1200 cm^{-1} are overlapped by organics peaks in SEI film, the peak at lower wavenumber than 300 cm^{-1} is chosen to identify Li_2CO_3 products. The presence of Li_2CO_3 in Li-PC-EMC is a crucial difference from the absence of Li_2CO_3 in Li-EC-EMC, which may influence the performance of SEI film. In chapter 4, a further analysis on this peak will be explain by using 785 nm laser and Au NPs SERS sensor.

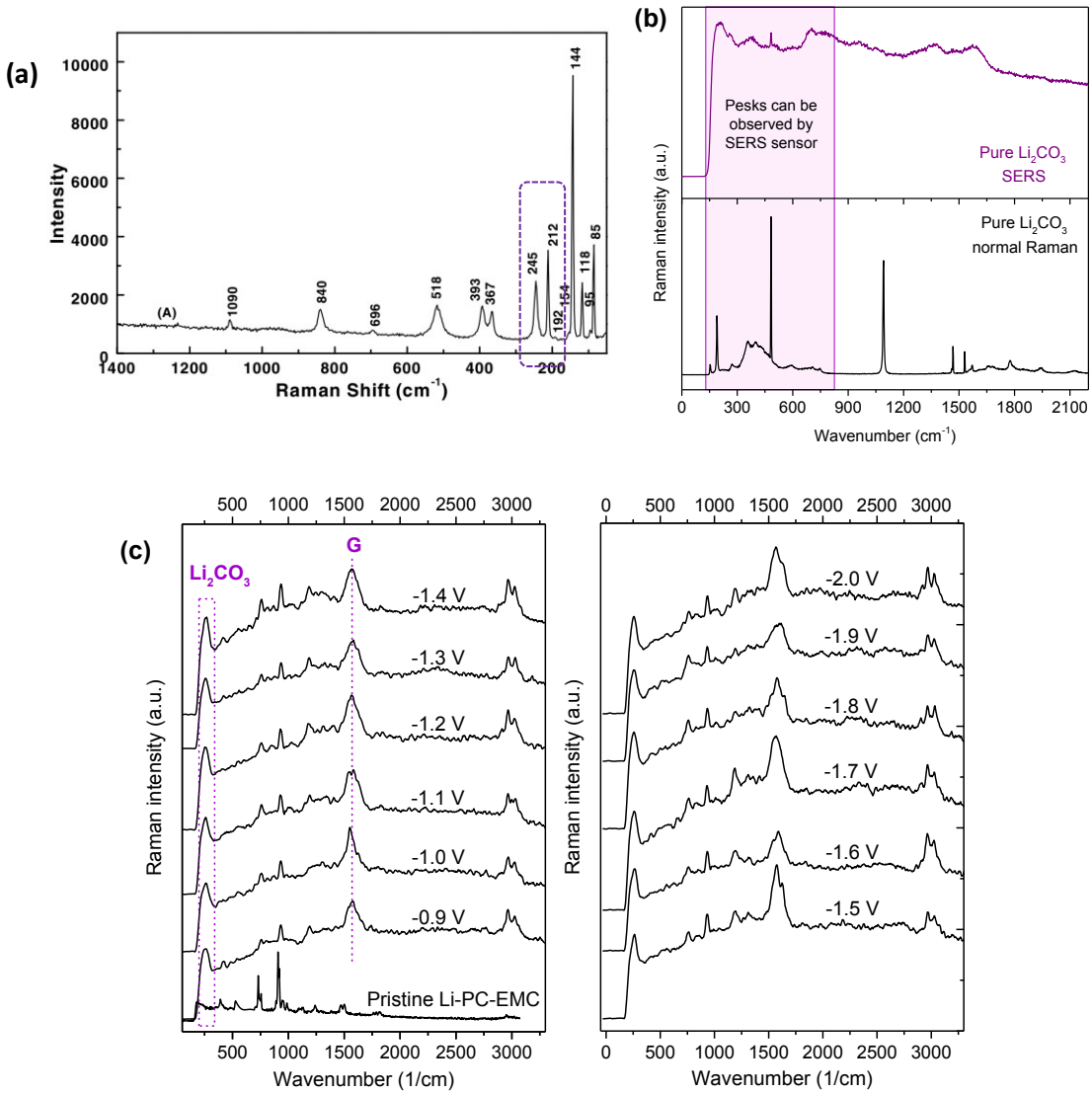

Figure 3.12 (a) Raman spectrum of pure Li_2CO_3 refer to the book of Balbuena et al. [1] (b) SERS and Raman spectra of pure Li_2CO_3 with and without Ag NPs convex sensor, measured in this study. (c) Kinetic SERS spectra during SEI formation in Li-PC-EMC from the voltage of -0.9 to -2.0 V

3.3.4 Kinetic observation on SEI formation in PC-based electrolyte using multi laser spots

The kinetic observation in section 3.3.3 was conducted on graphite surface, using single laser spot. The diameter of the single laser spot was about 2 μm, which involved numerous graphite

particles, so that the Raman peaks would include the signals from both of the basal and edge of graphite. In order to investigate precise reaction on graphite in Li-PC-EMC, HOPG was used as graphite model with clear basal and edge plane. Moreover, the real-time 2D mapping of the SEI formation was monitored by using the Raman spectroscopy installed with 11 x 11 multi laser spots. When CV scan started, a series of 2D Raman mappings were recorded continuously. *Figure 3.13* is one of the Raman spectrum measured at a 20 x 20 μm^2 area of the HOPG surface, when the voltage was around -2.0 V. Since the measurement was carried out at the interface of HOPG and electrolyte, many peaks of SEI film are overlapped by the peaks from electrolyte. However, comparing with the pristine electrolyte, some new peaks can be distinguished. They are the peak of inorganic product Li_2CO_3 at the lower wavenumber than 300 cm^{-1}, the peak of organic product LiOR at 1020 cm^{-1} and the peak of organic product $ROCO_2Li$ at 1170 cm^{-1}. Besides, the G peak and the D peak from HOPG were also detected.

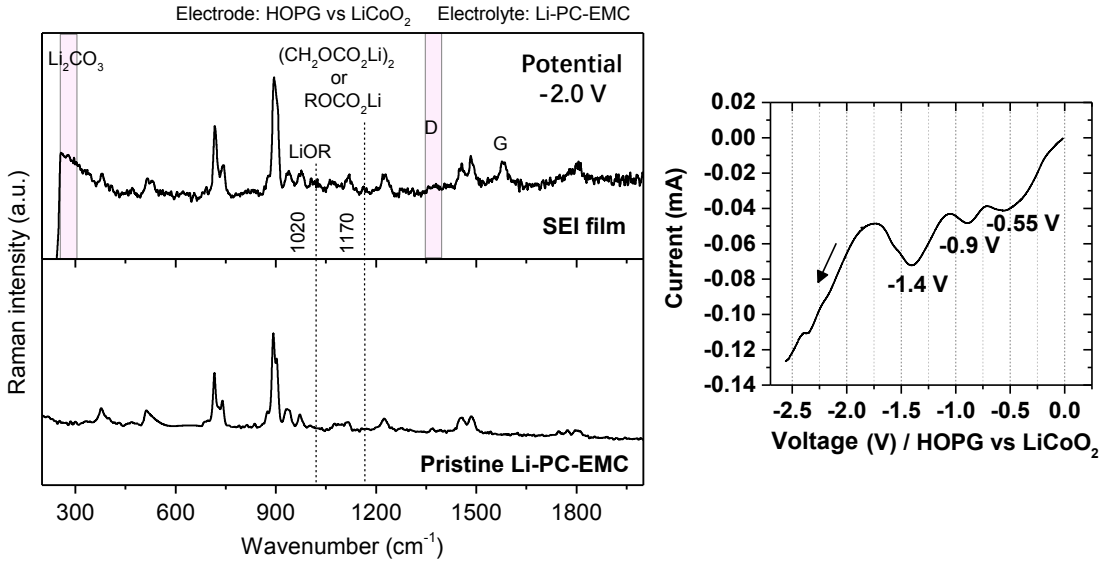

Figure 3.13 Raman spectrum of the SEI film at HOPG surface formed in Li-PC-EMC at the voltage of -1.2 V (HOPG vs $LiCoO_2$)

Before analyzing the kinetic variation in the peaks of the inorganic and organic products, the 2-D Raman intensity mapping of D peak was investigated. D peak is the breathing modes of sp2 atoms originate from defects, so that it can be used for estimating the edge area of graphite. *Figure 3.14* shows the optical image of the focusing area at HOPG surface and the Raman intensity mapping of D peak observed from the same area. The optical image displays the clear basal and edge plane of graphite. Accordingly, in the Raman mapping of the intensity of D peak, the red

area standing for the high intensity of D peak presents the approximate area of the edge plane of graphite, corresponding to the structure shown in the optical image. This result identify the resolution of 2-D Raman mapping is sufficient to distinguish the different vibration at the basal plane and the edge plane. Based on this demonstration, the kinetic formation of inorganic product and organic products at the basal and the edge of graphite will be investigated at the focusing area.

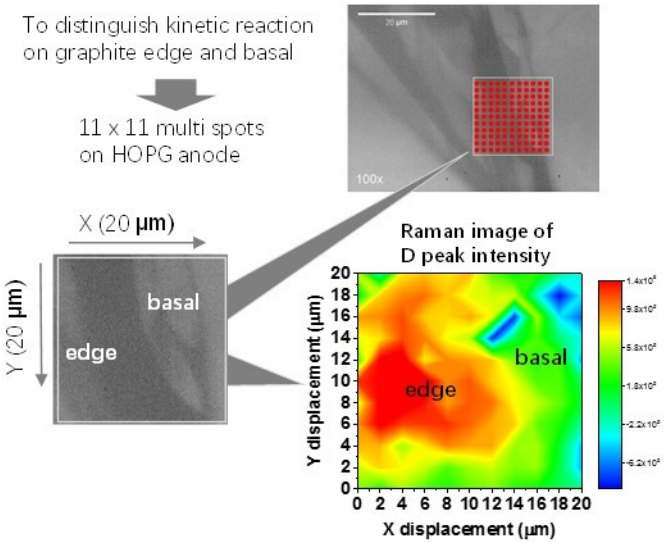

Figure 3.14 Schematic of area monitoring on HOPG basal and edge plane

The kinetic Raman intensity mappings of the Li_2CO_3 peak along with CV scan are shown in *Figure 3.15*. The *Figure 3.15* (a) display the X-Y Raman intensity mapping of D peak for comparison. The *Figures 3.15* (b) and (c) are the variation in the 1-D Raman intensity mapping of Li_2CO_3 peak along with voltage changing from -0.1 to -1.5 V. These two graphs were plotted with the method introduced in section 3.2.2. For each single measurement, 121 Raman spectra were detected with the 11 x 11 multi laser spots, and the X-Y Raman intensity mapping of Li_2CO_3 peak could be plotted. Meanwhile, the software for Raman spectra measurement can accumulate the data spot from the same axis value into single data spot, so that the 2-D X-Y Raman mapping can be transferred into 1-D X (or Y) Raman intensity mapping. Along with CV scanning, the real-time Raman spectra at the focusing area was continuously monitored, simultaneously, the kinetic variation in the transferred 1-D X and Y Raman intensity mapping was recorded as shown in *Figures 3.15* (b) and (c).

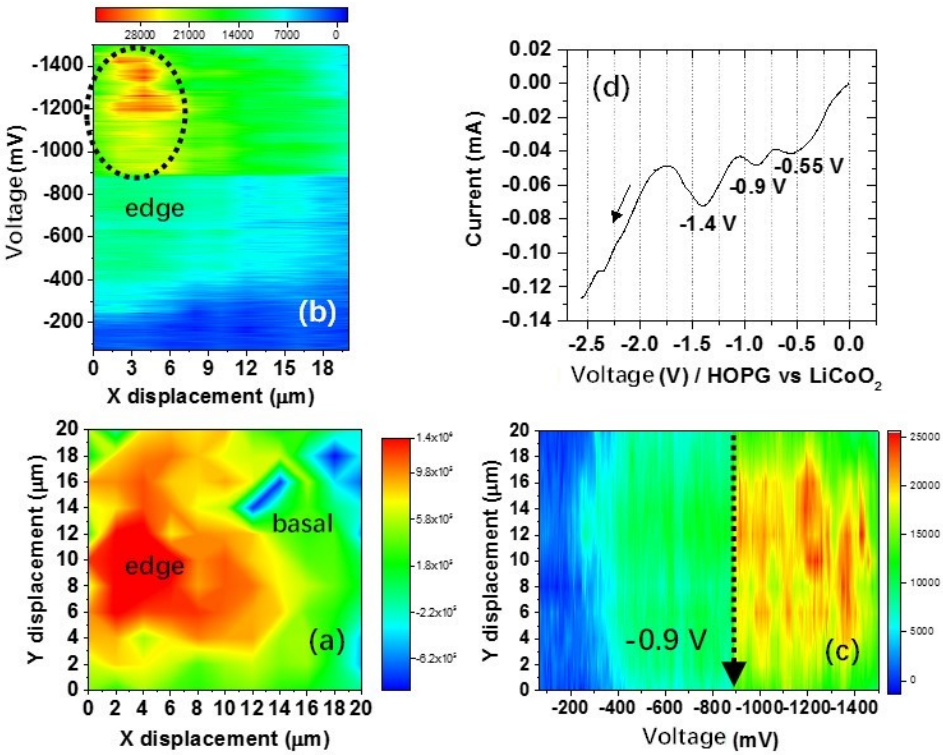

Figure 3.15 (a) X-Y Raman intensity mapping of D peak; (b)(c) Kinetic Raman intensity mapping of Li_2CO_3 peak along with charging cycling; (d) Cyclic voltammetry of HOPG anode versus $LiCoO_2$ cathode, from 0 to -2.5 V with the scan rate of 1mV/s. Graph (b) are plotted from hundreds of X-Y Raman intensity mapping of Li_2CO_3 peak. The 2-D Raman mapping was transferred to 1-D line data consisted to the accumulated data from each X displacement. Graph (c) was plotted in the same way, but accumulated data from each Y displacement. Along with CV scan and voltage changing, the transferred 1-D line results were kinetically observed as graphs (b) and (c).

The scale bar in *Figure 3.15* show the relation of peak intensity and color. The red color stands for the higher peak intensity. The peak variation in *Figure 3.15* (b) suggests that the appearance area of Li_2CO_3 peak was only observed at the edge area of HOPG anode, comparing to the Raman intensity mapping of D peak in *Figure 3.15* (a). Besides, the obvious increase in the Raman intensity of Li_2CO_3 in *Figures 3.15* (a) (b) demonstrate the decomposition of PC-based electrolyte around -0.9 V that lead to the inorganic product of Li_2CO_3.

Moreover, the variations in the peak intensities of organic products were also analyzed. According to former discussion, the peaks at 1020 cm^{-1} and 1170 cm^{-1} are attributed to organic product LiOR and $ROCO_2Li$. *Figure 3.16* is the kinetic variation in the 1-D X Raman intensity mapping of the peaks at 1020 cm^{-1} (a) and 1170 cm^{-1}(b). Comparing to the structure of the

focusing area, the product LiOR may be generated at both of the basal and edge plane of graphite, and the product $ROCO_2Li$ may be formed mainly at the edge plane of graphite. Besides, the formation of these two organic products were observed to occur start from -1.2 V that is posterior to the formation of Li_2CO_3.

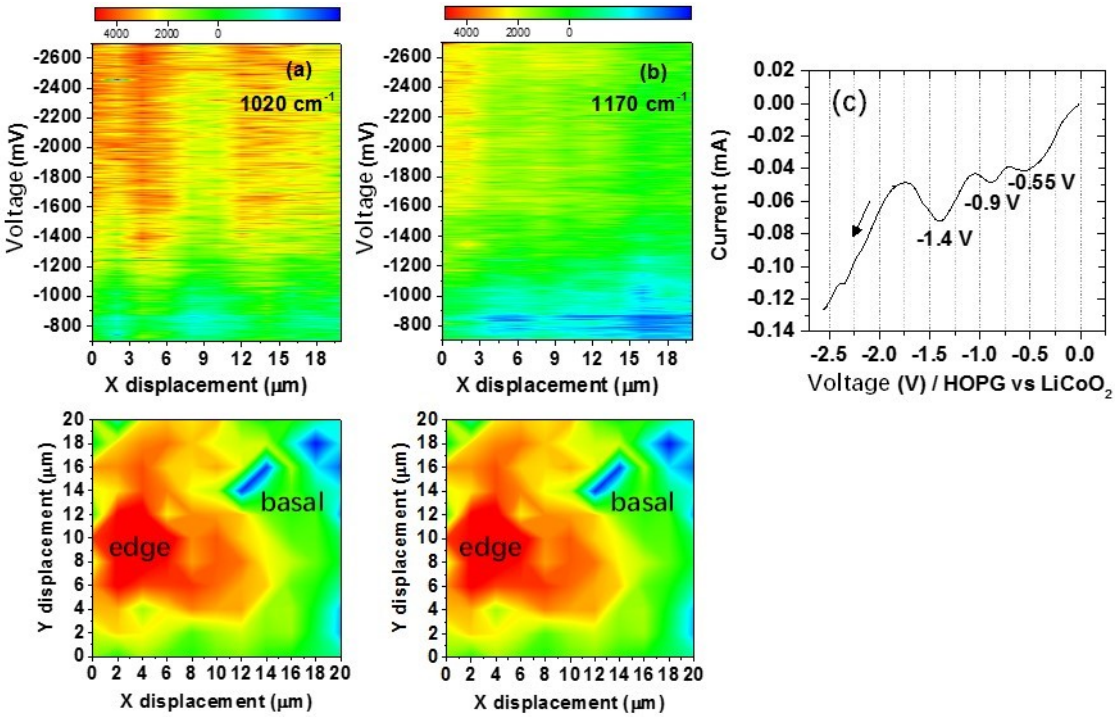

Figure 3.16 Kinetic Raman intensity mapping of the peaks at 1020 cm^{-1} and 1170 cm^{-1}, along with charging cycling.

The observation using multi laser spot demonstrates the decomposition of electrolyte at HOPG anode maybe -0.9 V, which is corresponding to the previous literature about the reaction potential [14-17]. Furthermore, the formation area of Li_2CO_3, LiOR and $ROCO_2Li$ were also investigated, which was nearly not discussed in previous literatures.

3.4 Conclusion

In this chapter, SERS technique was successfully applied in the observation on SEI film at the surface of graphite anode in LIB. According to the previous reports and the thermal stability of SEI film observed in this chapter, the unstable SEI film formed in PC-based electrolyte was confirmed. To discover the difference of PC-based electrolyte and EC-based electrolyte, the kinetic SEI film formation was focused by using SERS sensor. The convex lens transmission SERS sensor was demonstrated to show good performance and was used for detecting the kinetic reaction during SEI film formation. The results suggest that, an apparent new peak appear when using Li-PC-EMC, comparing to the peaks observed in Li-EC-EMC. This peak maybe attributed to the inorganic compounds Li_2CO_3. Furthermore, in Li-PC-EMC, the multi-laser spot was employed for area monitoring on HOPG basal and edge plane. The formation Li_2CO_3 and $ROCO_2Li$ was demonstrated to occur at the edge of graphite and ROLi product was detected on both edge and basal plane.

This chapter found the Li_2CO_3 product maybe one of the difference between EC-based electrolyte and PC-based electrolyte. The formation of Li_2CO_3 will be further analyzed by Au NPs in chapter 4.

References

[1] P.B. Balbuena, Y. Wang, Lithium-ion batteries: Solid-Electrolyte Interphase, Imperial College Press, London, 2004.

[2] P. Verma, P. Maire, P. Novák, Electrochimica Acta, 55 (2010) 6332-6341.

[3] D. Aurbach, M.L. Daroux, P.W. Faguy, E. Yeager, Journal of The Electrochemical Society, 134 (1987) 1611-1620.

[4] M. Onuki, S. Kinoshita, Y. Sakata, M. Yanagidate, Y. Otake, M. Ue, M. Deguchi, Journal of The Electrochemical Society, 155 (2008) A794-A797.

[5] K. Tasaki, The Journal of Physical Chemistry B, 109 (2005) 2920-2933.

[6] G.V. Zhuang, K. Xu, H. Yang, T.R. Jow, P.N. Ross, The Journal of Physical Chemistry B, 109 (2005) 17567-17573.

[7] K. Xu, Y. Lam, S.S. Zhang, T.R. Jow, T.B. Curtis, The Journal of Physical Chemistry C, 111 (2007) 7411-7421.

[8] J. Vatamanu, O. Borodin, G.D. Smith, The Journal of Physical Chemistry C, 116 (2012) 1114-1121.

[9] Y. Masahiro, S. Mikiko, K. Masahiro, H. Takayuki, Applied Physics Express, 9 (2016) 122002.

[10] D. Alves Dalla Corte, G. Caillon, C. Jordy, J.-N. Chazalviel, M. Rosso, F. Ozanam, Advanced Energy Materials, 6 (2016) 1501768-n/a.

[11] A. Li, P. Du, Z. Chen, R. Zhao, W. Huang, L. Zou, D. Huang, H. Chen, Ionics, 21 (2015) 2431-2438.

[12] V. Ittah, D. Huppert, Chemical Physics Letters, 173 (1990) 496-502.

[13] Y. Hase, I.V.P. Yoshida, Spectrochimica Acta Part A: Molecular Spectroscopy, 35 (1979) 379.

[14] A. Naji, J. Ghanbaja, B. Humbert, P. Willmann, D. Billaud, Journal of Power Sources, 63 (1996) 33-39.

[15] K.A. Hirasawa, T. Sato, H. Asahina, S. Yamaguchi, S. Mori, Journal of The Electrochemical Society, 144 (1997) L81-L84.

[16] K. Xu, Chemical Reviews, 114 (2014) 11503-11618.

[17] K. Xu, Chemical Reviews, 104 (2004) 4303-4418.

Chapter 4: Depth profile on SEI film and the mechanism of Li_2CO_3 formation in LIB

4.1 Introduction

In chapter 3, the Li_2CO_3 product was considered to be the product in PC-based electrolyte according to the kinetic SERS spectra during SEI formation. However, the observed Raman frequencies of Li_2CO_3 were at the low wavenumber (<300 cm^{-1}), which were partially cut off by the notch filter installed on the 532 nm laser of our Raman machine. Since the notch filter installed on the 785 nm laser of our Raman machine only cut off the signals lower than 200 cm^{-1}, it allows measuring the Raman frequencies at the range of 200-300 cm^{-1}, which cannot be precisely analyzed in chapter 3. Thus, in this chapter, the laser of 785 nm will be used for further exploring the generation of Li_2CO_3 and its mechanism. To observe the SERS spectra, Au NPs SERS sensor was used because the laser of 785 nm is suitable to irradiate the plasma resonance at the Au NPs surface (introduced in section 1.1.2.2).

There are controversies among the researches about the decomposition products of PC-based electrolyte and EC-based electrolyte. one of the controversies is the presence of Li_2CO_3 products in the SEI film. Li_2CO_3 is mostly believed to originate from a two-electron reduction pathway (eq 1, take PC as example) of cyclic carbonates [1-3].

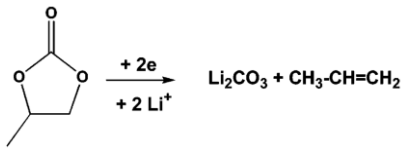

(eq 1)

Aurbach and co-workers estimated the semi-carbonates as the main components of SEI via the single-electron pathway as eq 2, and the Li2CO3 was considered as an artificial product due to poor humidity management, which could be understood as the Li2CO3 should not exist as a reduction product under well humidity management. This was supported by numbers of researches [4-11].

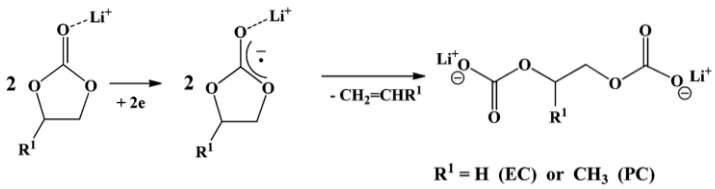

(eq 2)

However, many of them still described Li_2CO_3 as an SEI component according to their research [12-21]. These researches reported that the Li_2CO_3 could be observed on either first cycling

graphite, or aged graphite surface, and consider Li_2CO_3 as one of the main components. The role of Li_2CO_3 in SEI film was reported from many aspects, the innermost layer of SEI [9, 22], the Li^+ ion transportation media [23, 24], and so on.

At the present, the Li_2CO_3 generation and the reaction mechanism during SEI formation is not clearly understood yet. Other than many reported controversial factors [1, 9, 25], the interfacial behavior of PC and EC at graphite surface may also affect the reaction, but not sufficiently studied so far. Therefore, the solvent interaction and interfacial adsorption without Li^+ ion were mainly concerned in this research. The solvent interaction is a basic factor for the interfacial property of a solution. The interfacial behavior may concern to the reduction pathway, products, and further affect the SEI and batteries properties.

In summary, to have a closer understanding of the Li_2CO_3 product in SEI film, SEI films are further discussed in this chapter. The observation on Li_2CO_3 generation is precisely demonstrated by Au NPs SERS sensor, the mechanism of Li_2CO_3 generation is figured out, and the depth profile of SEI film is analyzed. This chapter further apply SERS and Raman spectroscopy to the composition, reaction mechanism and depth profiling of the interfacial reaction in LIB.

4.2 Experimental section

4.2.1 Samples and materials

Graphite anode: Mesocarbon microbeads (MCMB) graphite powder was coated on Cu foil, purchased from MTI Corporation; Cathode: a $LiCoO_2$ thin film was deposited on the flat surface of a silver foil, purchased from MTI Corporation. When exploring the interfacial behavior of PC at the basal and edge graphite, HOPG (Highly oriented pyrolytic graphite) purchased from ALLIANCE Biosystems, Inc. was used as graphite model, purchased from ALLIANCE Biosystems, Inc.

For observing preferential adsorption of carbonate solvent, the mixed solvent of PC:EMC (1:1) and EC:EMC (1:1) were prepared. In following expression, the two mixed solvent will be short for PC-EMC and EC-EMC. PC-EMC and EC-EMC were used to analyze the interfacial molar fraction of PC (x_{PC}) and EC (x_{EC}). The interfacial molar fraction (x_i) in standard samples was calculated by the equation $x_i = \frac{n_i}{n_{total}}$. The x_i on graphite surface was estimated by the linear relationship obtained by standard samples.

For analyzing SEI formation, 1M $LiPF_6$ was dissolved in these solvents respectively, to prepare the electrolyte solution. The electrolyte solution with 1M $LiPF_6$ dissolved will be short for Li-PC-EMC and Li-EC-EMC.

4.2.2 Raman measurement

In order to determine the Li_2CO_3 product in SEI film at low frequency, a confocal Raman spectroscopy with a laser of 785 nm was used for the in-situ measurement. The notch filter installed on 785 nm laser can cut off the signal low than 200 cm^{-1}, which allow the measurement of Li_2CO_3 at the range of 200-300 cm^{-1}.

To figure out the interfacial behavior of PC and EC at the interface, Raman mapping were carried out at the graphite surface in contact with different electrolyte solvent, with the laser of 532 nm, because 532 nm laser is suitable to excite the Raman scattering of organic compounds in electrolyte solvents. x

Depth profile measurement mode was conducted with the laser of 785 nm for qualitatively

analyzing the depth profiling of the Li_2CO_3 product in SEI film.

4.2.3 SERS sensor

Au NPs SERS sensor was designed for measuring the Li_2CO_3 product in SEI film by using 785 nm laser. Similar to the SERS sensor used in chapter 3, the substrate is also convex lens (quartz) with the diameter of 2 mm and the thickness of 0.8 mm. The Au Nanoparticles were sputtered on the convex surface with the diameter around 50 nm. The schematic and SEM image of the SERS sensor are explained in *Figure 4.1*.

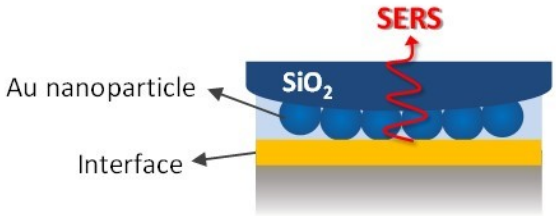

Figure 4.1 The structure of the Au NPs convex SERS sensor

4.2.4 Cell set up for the in-situ SERS measurement and electrochemical reaction

The electrochemical cell and cyclic voltammetry are the same as the explanation in Chapter 3. The difference from chapter 3 is that the measurement in this chapter was conducted after the SEI film formation, but not during the cyclic voltammetry scanning.

4.3 Results and discussion

4.3.1 Li_2CO_3 generation and mechanism

4.3.1.1 Detection of Li_2CO_3 products by using Au NPs SERS sensor

Li_2CO_3 has been reported to be one of the products of the SEI, but there are also a number of report claimed that Li_2CO_3 was not present or not the main compound. The presence of Li_2CO_3 appears to be considered as the by-products depend on the moisture content of the electrolyte. To test the influence of moisture, the moisture situation in this study was roughly divided into "lower humidity" and "higher humidity". The lower humidity group is the LIB model cell managed by vacuum pumping. All electrode, electrolyte, electrochemical cell and SERS sensor were vacuum treated in glove-box over 10 h to eliminate trace water. The higher humidity group is the electrochemical cell without any special treatment.

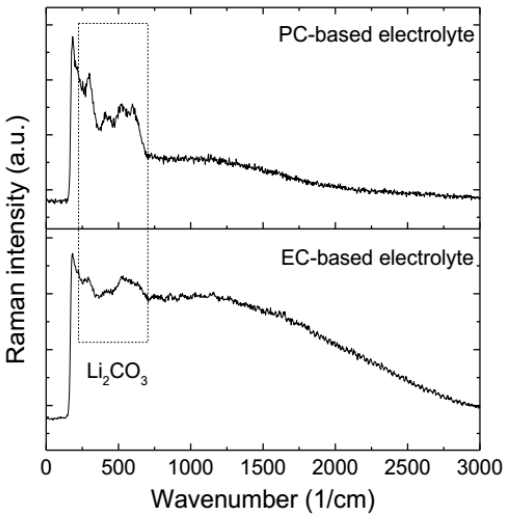

Figure 4.2 SERS spectra on SEI film in EC-based electrolyte and PC-based electrolyte under the condition without special humidity control. Strong peaks from Li_2CO_3 were enhanced by Au NPs SERS sensor comparing to other weak peaks from organic compounds.

To demonstrate the Li_2CO_3 generation under high humidity as previous literature mentioned, the SERS spectra were measured on the SEI film that was formed under no special humidity control. The SERS spectra of SEI film formed in PC-based electrolyte and EC-based electrolyte

was measured using the Au NPs SERS sensor under the laser irradiation with the wavelength of 785 nm. *Figure 4.2* shows the SERS spectra in the higher humidity. The drastic strong Li_2CO_3 peaks at low frequencies [26] was enhanced by SERS sensor. It describes that, in both of Li-PC-EMC and Li-EC-EMC, Li_2CO_3 would be generated in large amounts under higher moisture, which is corresponding to many literatures [25]. Meanwhile, it also demonstrates that Au NPs SERS sensor maybe has higher sensitivity to enhance the Raman scattering of Li_2CO_3, comparing to the enhancement of other peaks (G peak and other peaks of organic compounds in SEI film).

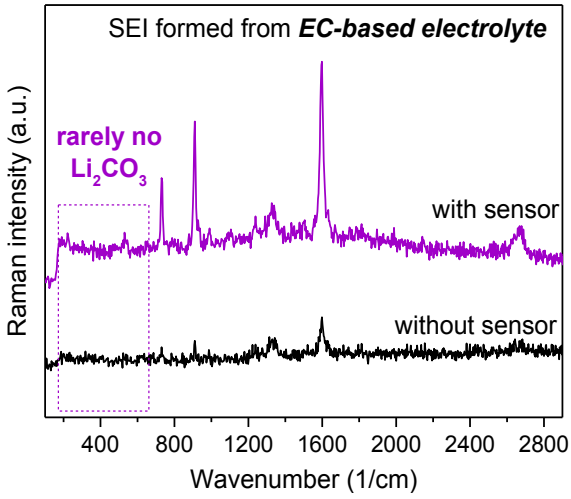

Figure 4.3 SERS and Raman spectra on SEI film in EC-based electrolyte with and without Au SERS sensor. No peak from Li_2CO_3 is detected when using sensor or not.

Other than demonstrating the Li_2CO_3 product in higher humidity, SERS spectra were also measured on the SEI film formed in low humidity, to discover that if Li_2CO_3 could be also detected with well moisture control. The low humidity was controlled by vacuum treating all the samples, electrochemical cell and SERS sensor more than 10 h in glove-box, and then assembled and sealed the electrochemical cell well. Afterward, the CV scanning was also carried out in glove box with the voltage range of -3.0 to 3.0 V, and the scan rate of 0.5 mV/s. After 5 cycles, the electrochemical cell was taken out of the glove box and measured by using Raman spectroscopy. *Figure 4.3* is the Raman spectra of SEI film when using EC-based electrolyte in low humidity, measured with SERS sensor and without sensor respectively. As a result, there is no obvious Li_2CO_3 peak observed in the products of EC-based electrolyte regardless of using sensor or not. Only peaks of organic compounds and graphite are observed by Au NPs SERS sensor.

However, it is different in *Figure 4.4*, which was measured on the SEI film form in PC-based

electrolyte. Other than the organic peaks and graphite peaks observed on SEI film without SERS sensor in *Figure 4.4*, notable Li_2CO_3 peaks (210 cm^{-1} and 290 cm^{-1} [26]) still can be detected when using the SERS sensor. Comparing to the peaks in *Figure 4.2*, The weaker peaks of Li_2CO_3 indicate that the amount of Li_2CO_3 is reduced, because the partial Li_2CO_3 produced by the reaction with water was avoided in low humidity. These results support the presence of Li_2CO_3, but only support the presence of Li_2CO_3 when using PC-based electrolyte. Rarely no or undetectable amount of Li_2CO_3 was generated in the products of EC-based electrolyte. In addition, it also suggests that the Li_2CO_3 generation could be affected but not only affected by moisture. Li_2CO_3 generation also depends on the different solvent species (PC and EC in this study). But the reason why PC and EC would lead to different products is not understood clearly.

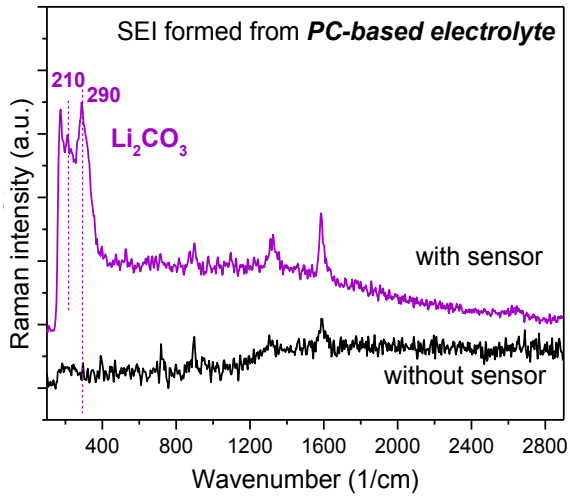

Figure 4.4 SERS and Raman spectra on SEI film in PC-based electrolyte with and without Au SERS sensor. Clear peaks of Li_2CO_3 can be detected when using SERS sensor.

4.3.1.2 Mechanism of Li_2CO_3 formation and its relation with interfacial behavior of PC and EC at the graphite surface

There are a plenty of works on the main component of SEI film, which have been ascribed to be organic compounds. This study concentrates on the controversial inorganic compounds Li_2CO_3 for a closer look at their reaction mechanism. The reaction generating Li_2CO_3 is believed to occur at the edge of graphite along with other interfacial reaction for SEI film formation. Li_2CO_3 would be produced from cyclic carbonate at the interface, but to the present, the spatial

confirmation of the interfacial behavior of PC and EC at graphite surface is not reported in the literatures on LIB work. In this chapter, the only electrolyte solvent EC-EMC and PC-EMC without Li salt are investigated by using Raman spectroscopy to identify the interfacial behavior of PC and EC. The acyclic carbonate DMC was also used as the mixed solvent of EC-DMC when demonstrating and comparing the different interfacial molar fraction of PC (x_{pc})and EC (x_{EC}).

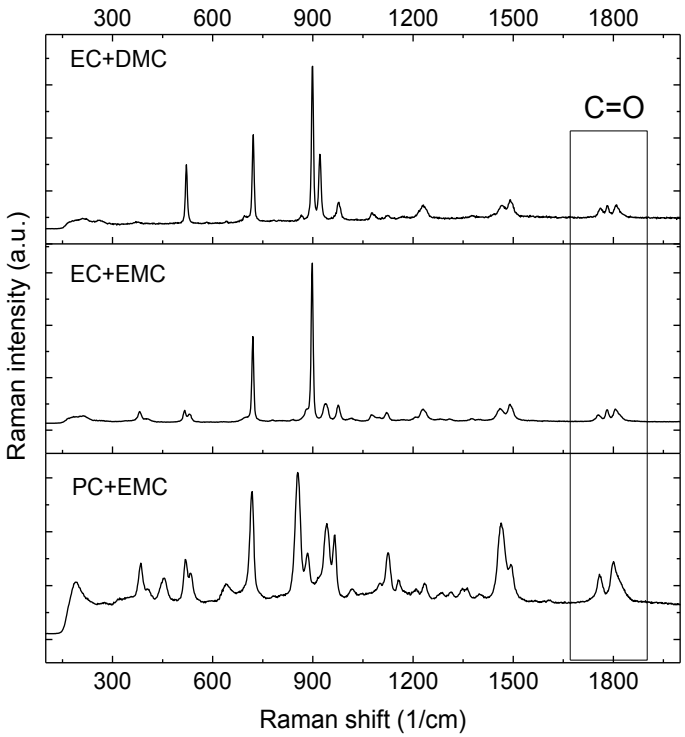

Figure 4.5 Raman spectra of bulk EC/EMC (1:1), EC/DMC (1:1) and PC/EMC (1:1)

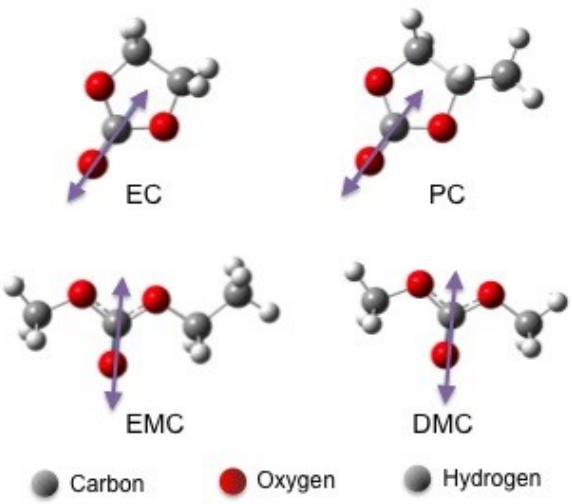

Figure 4.6 C═O stretching vibrations of PC, EC, EMC and DMC, simulated by DFT

Measuring Raman mapping at the interface of graphite and solvent is useful to find the interfacial molar fraction of each solvent species. At first, as the fundamental information of each electrolyte solvent for further analysis, *Figure 4.5* shows the Raman spectra of three mixed solvents and the peaks' assignment correspond to EC-EMC, PC-EMC and EC-DMC based on the reference studies [27] and DFT calculation. The specific peaks around 1800 cm^{-1} are attributed to the stretching vibration of C═O as shown in *Figure 4.6*. To quantify the molar fraction of each solvent species in their respective mixed solvent, a series of mixed solvent of PC-EMC, EC-EMC and EC-DMC are prepared to calculate the linear relationship of x_i dependence on the ratio of peak intensity. *Figure 4.7* presents the zoom area of the peaks of C═O stretching vibration. The linear relation formulations are y=3.084-4.15x for PC-EMC, y=3.77+9.11x for EC-EMC and y=2.37-2.76x for EC-DMC, respectively. The x_{PC} and x_{EC} at the graphite surface could be estimated by these linear relation formulations and the observed Raman peaks' intensity.

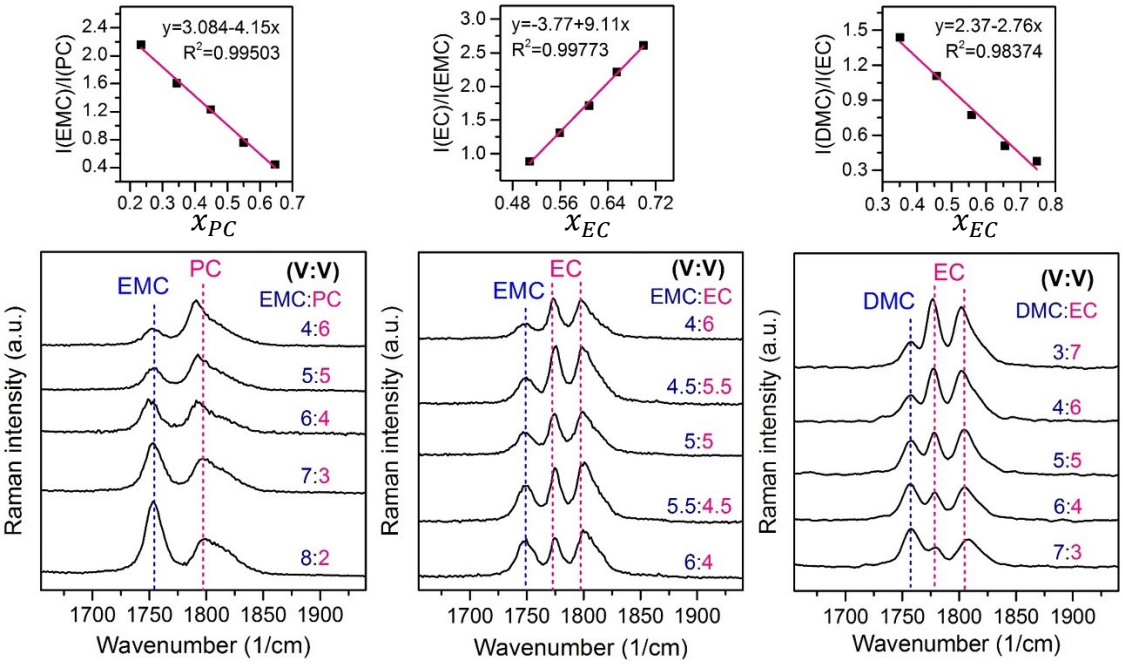

Figure 4.7 Raman spectra of C═O vibration from the mixture solvent of PC-EMC, EC-EMC, and EC-DMC with a series of ratio, and the molar fraction (x_{PC} and x_{EC}) dependence on the ratio of I(cyclic) and I(acyclic) in the above graphs

SERS sensor is not used for studying the solvent distributing at the graphite surface, because

of the close contact between SERS sensor and graphite electrode leave no space to sufficient solvent molecules. Besides, since the graphite electrode composes from many particles and pores inside, the Raman scattering measurement is carried out in micrometer scale but not nanometer scale, to find out the x_{PC} from a macroscopic view. It results in the Raman mapping profiles display a rough and broad tendency but not visible sharp interfaces. In the present work, the variation tendencies of x_{PC} and x_{EC} at the interface was discovered. *Figure 4.8* shows the X-Z Raman mapping at the interface of graphite and PC-EMC. the x_{PC} is calculated according to the intensity ratio of the C═O peak and the linear relation formulation in *Figure 4.7*. The surface of graphite is roughly estimated from the Raman intensity mapping of G peak of graphite in *Figure 4.8 (a)*. Correspondingly, in *Figure 4.8 (b)*, the x_{PC} appear to show the lower value toward graphite surface and interior. The interior porous graphite structure allows the low PC concentration among the internal graphite particles is detectable. It suggests that at the surface of graphite particles, the molar fraction of PC molecules is lower than bulk sample.

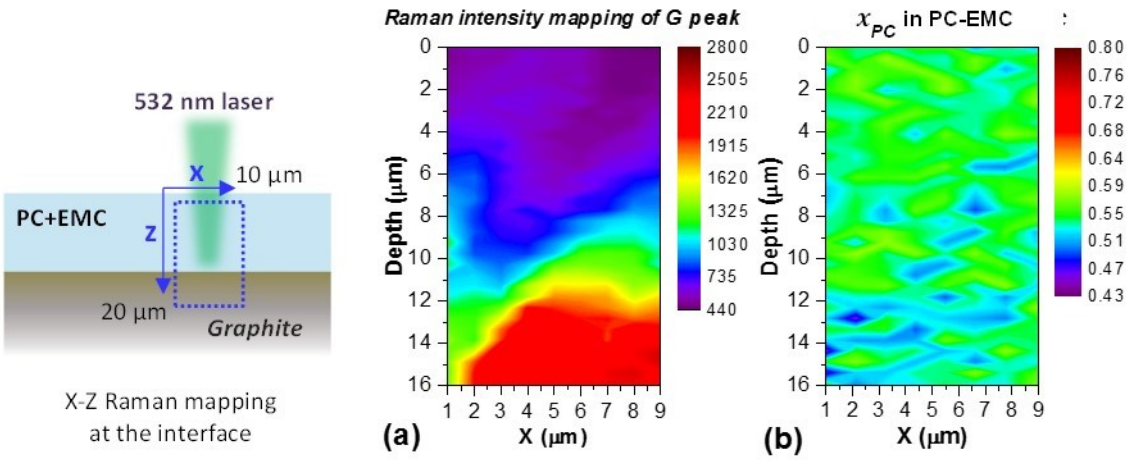

Figure 4.8 X-Z Raman mapping on I(G) (a) and PC molar fraction ($\boldsymbol{x_{PC}}$) (b) at the interface of graphite and PC-EMC

However, in the case of EC-based electrolyte, the X-Z Raman mapping at the interface of graphite and EC-EMC is shown in *Figure 4.9*. Different from PC-EMC, there is no decrease tendency of EC molar fraction toward graphite surface. The x_{EC} molecules at the interface maintains the same level as bulk sample. To the present, there is no research on the adsorption behavior of PC or EC at the graphite surface, which also cannot be demonstrated in this study. What we can understand here is that, in some way, PC is not preferentially adsorbed (or

accumulated) at graphite surface in PC-EMC, but EC didn't show the same phenomenon in EC-EMC.

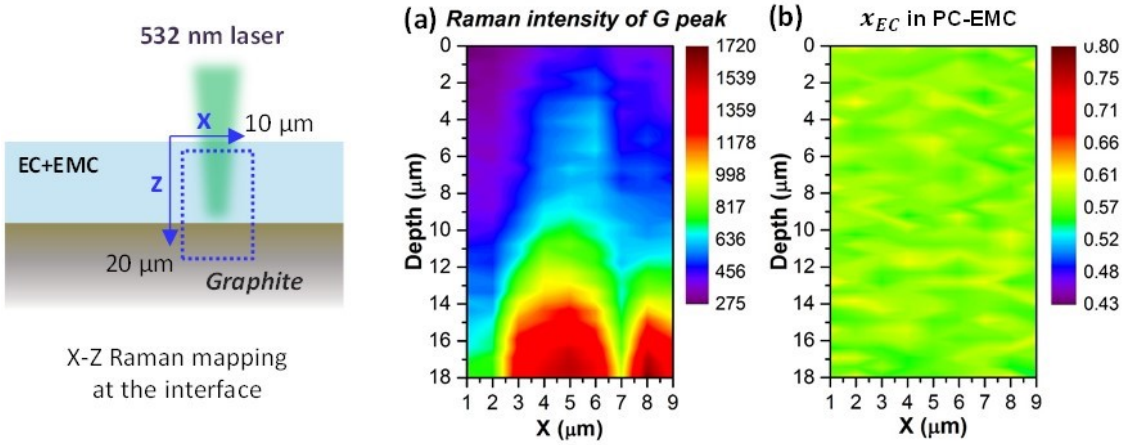

Figure 4.9 X-Z Raman mapping on I(G) (a) and EC molar fraction ($\boldsymbol{x_{EC}}$) (b) at the interface of graphite and EC-EMC

This conclusion is further reinforced by the X Raman mapping of x_{PC} and x_{EC} at graphite surface, under voltage of 0 V and 0.5 V. *Figure 4.10 (a)* is the x Raman mapping of x_{PC} in PC-EMC, x_{EC} in EC-EMC and x_{EC} in EC-DMC with no applied voltage. Apparently, the x_{PC} is always lower than x_{EC} in their respective mixed solvents. In the bulk samples of PC-EMC, EC-EMC and EC-DMC, the x_{PC} and x_{EC} are 0.55, 0.61 and 0.56, respectively. However, at the graphite surface, the x_{PC} and x_{EC} in PC-EMC, EC-EMC and EC-DMC are 0.51, 0.59 and 0.62, respectively. It indicates that the molar fraction we observed does not depend on their bulk samples, but lie on the interfacial behavior of different solvent species, PC and EC in this study. Moreover, it was demonstrated in previous research that Li^+ ion intercalation starts around 0.2 to 0.5 V and the reduction of cyclic carbonate starts around 1.0 V in the actual batteries. Therefore, in this study, the molar fraction of PC and EC was also observed under the voltage of 0.5 V in *Figure 4.10 (b)* to figure out the interfacial molar fraction of solvent species when Li salt was absent. As a result, when each voltage is applied, the x_{PC} is still lower than x_{EC} in their respective mixed solvents.

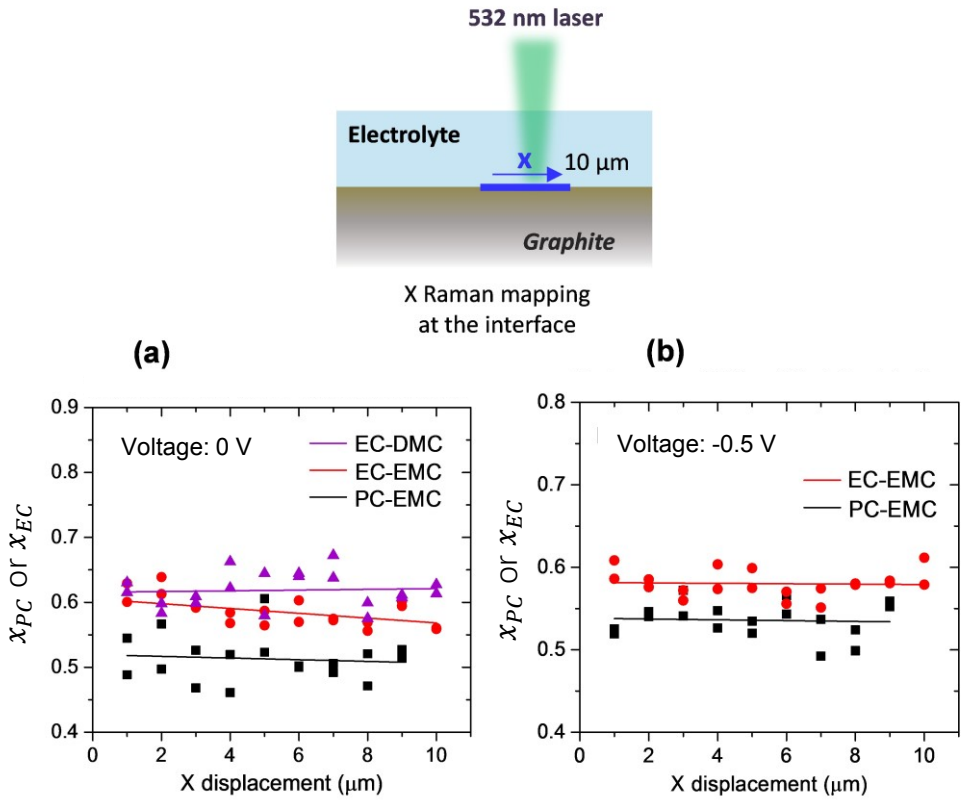

Figure 4.10 Raman mapping of the molar fraction of PC and EC ($\boldsymbol{x_{PC}}$ and $\boldsymbol{x_{EC}}$) at the graphite surface under a voltage of (a) 0 V, (b) -0.5 V in their respective mixed solvents (C.E.&R.E.: $LiCoO_2$)

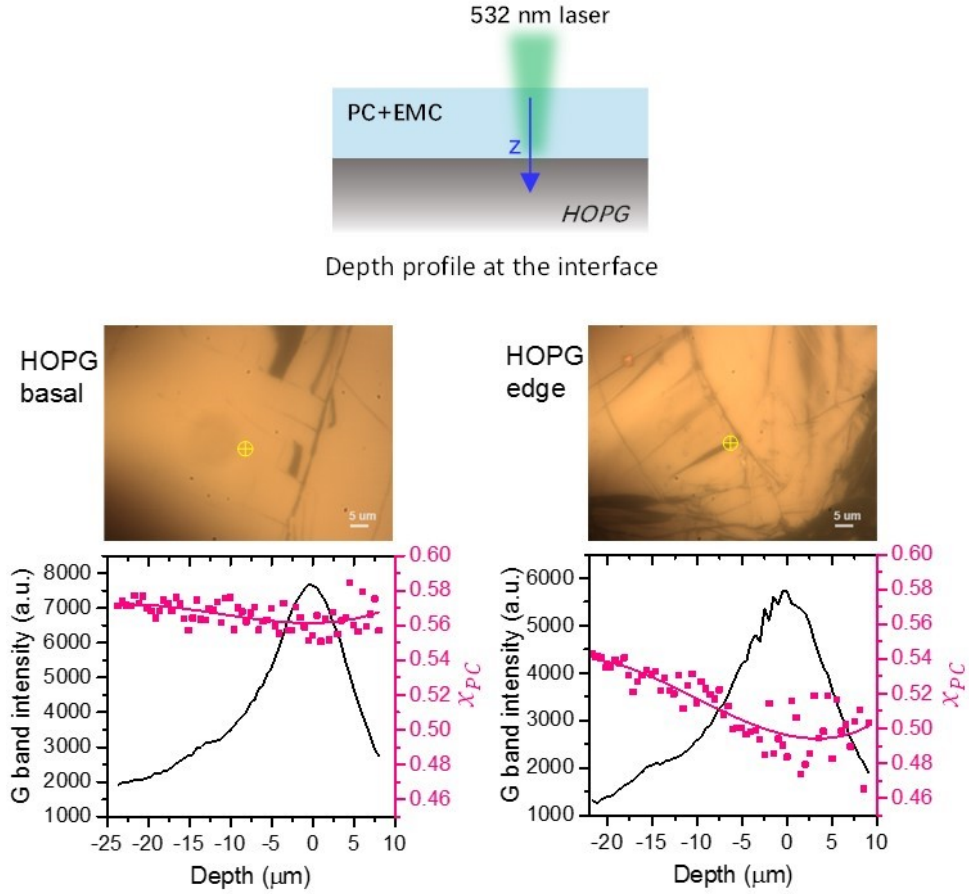

Figure 4.11 Depth profile on PC molar fraction at HOPG basal and edge plane. The optical images of HOPG surface indicate the measurement position at basal and edge plane of HOPG. The depth profiling of the Raman intensity of G peak and calculated PC molar fraction are plotted with X-Y-Y style in their respective measurement position

To have a closer look at the interfacial behavior of PC at the graphite surface, the depth profile on PC molar fraction at HOPG surface is carried out. HOPG is the highly oriented graphite layers, which allow distinguishing the basal and edge plane of graphite. The depth profile on the interface of PC-EMC and HOPG would be useful to compare the PC molar fraction at the basal and edge plane of graphite as seen in *Figure 4.11*. The depth profile on Raman intensity of G peak is for distinguishing graphite surface, according to the vertex. The PC molar fraction are calculated by the linear relation formulation in *Figure 4.7* and the intensity ratio of the C═O peak. At the basal plane, the PC molar fraction at the graphite surface maintain the same level as bulk sample. However, at the edge plane, the PC molar fraction gradually reduced toward the graphite surface, down to the same molar fraction as the X-Z Raman mapping shown in *Figure 4.8*. It indicates that

the lower molar fraction of PC is dominated by the edge of graphite, which is also the position for the reaction of cyclic carbonate and SEI film formation. According to the reaction formulation eq 1 and eq. 2, the organic compounds could be formed through the reaction of electrolyte species and electrons, which is mostly believed to be single-electron reduction pathway, while the Li_2CO_3 may be generated in the side reaction, 2-electron reduction pathway, when electrolyte molecules access more electron [28]. Based on the CV in *Figure 3.8*, the reduction current in Li-PC-EMC and Li-EC-EMC is at similar level. And then further considering the results of lower PC molar fraction at the edge plane of graphite, comparing with EC, some PC molecules may access more electron than EC molecule does. It may lead to more 2-electron reduction in PC-based electrolyte than EC-based electrolyte and further generate more Li_2CO_3 products. The schematic is explained in *Figure 4.12*. In conclusion, the interfacial molar fraction of cyclic carbonate at the edge of graphite would be related to the Li_2CO_3 generation. Lower interfacial molar fraction of cyclic carbonate leads to more products of Li_2CO_3.

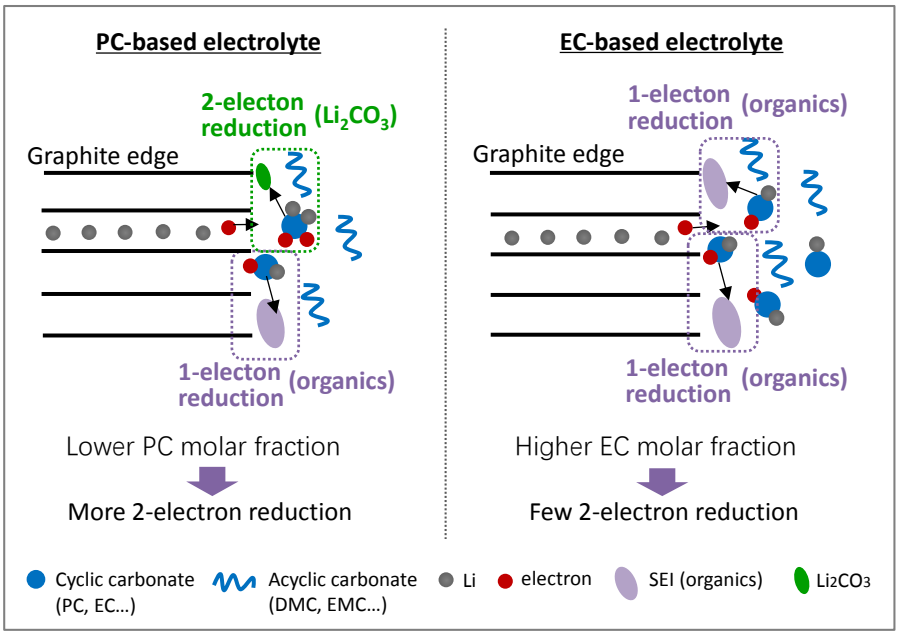

Figure 4.12 Schematic of proposed mechanism of Li_2CO_3 generation in PC-based electrolyte and its relation with interfacial molar fraction of cyclic carbonate.

4.3.1.3 Correlation of interfacial behavior and solvent molecules interaction

Although the lower interfacial molar fraction of PC was demonstrated, the mechanism of the

fewer PC at the interface is still not clear. In this section, some phenomena were observed about the solvent molecule interaction in their mixed solvents, which maybe meaningful to the interfacial behavior of PC and EC to a certain extent.

There is a theory about the primary solvation sheath of Li+ which is generally occupied by cyclic carbonate molecules. Cyclic carbonate molecules (such as EC and PC) are preferred by Li+ due to their higher permittivity and dipole moment (PC: dielectric constant of 65 under 25 °C; EC: dielectric constant of 69 under 25 °C and 90 under 40 °C [29, 30]). It was also identified in other papers that, a central Li^+ could be surrounded by a number of carbonyl groups from carbonate molecules, whose lone-pair electrons should be most effective in neutralizing the Coulombic attraction of the small cation [31, 32]. This structure was discussed with Li^+ ion dissolved. Before or after Li^+ ion intercalation, there should be free electrolyte solvent at the interface. Thus, in following part, the state of the only solvent without Li^+ ion will be discussed. Many researches have reported the molecular aggregates in solution, such as the dye solute in water solvent [33-35], nonionic surfactant in nonaqueous solvent [36-38] and so on. According to that, without Li^+ ion in the solvents, the inhomogeneous distribution of cyclic and acyclic carbonate may also exist as cyclic aggregates, due to their difference of polarity.

Figure 4.13 shows the Raman spectra of pure PC, pure EMC and mixed PC-EMC with a peak resolution of 2 cm^{-1}. In the Raman spectrum of PC-EMC, the Raman peaks' frequencies are mostly the same as the peaks of pure PC and EMC, except for the peak at 1800 cm^{-1} that blue shifted 10 cm^{-1} from the peak at 1790 cm^{-1} of pure PC. The blue shift come from the interaction between PC molecules but not from PC-EMC interaction, because there is no frequency shift of EMC in mixed solvent. A similar phenomenon of C=O frequency shift was also discussed in the Li^+ solvation sheath structure that the asymmetric stretching vibration of carbonyl ($\nu_{C=O}$) at ~1800 cm^{-1} was observed to be strongly perturbed by the dissolution of lithium salts [39-41]. It indicates that the C=O vibration is the main interaction bind site of Li^+ and PC. In the mixed solvent, it can be identified that PC-PC interaction also exist before Li^+ dissolved and the C=O vibration is also the bind site.

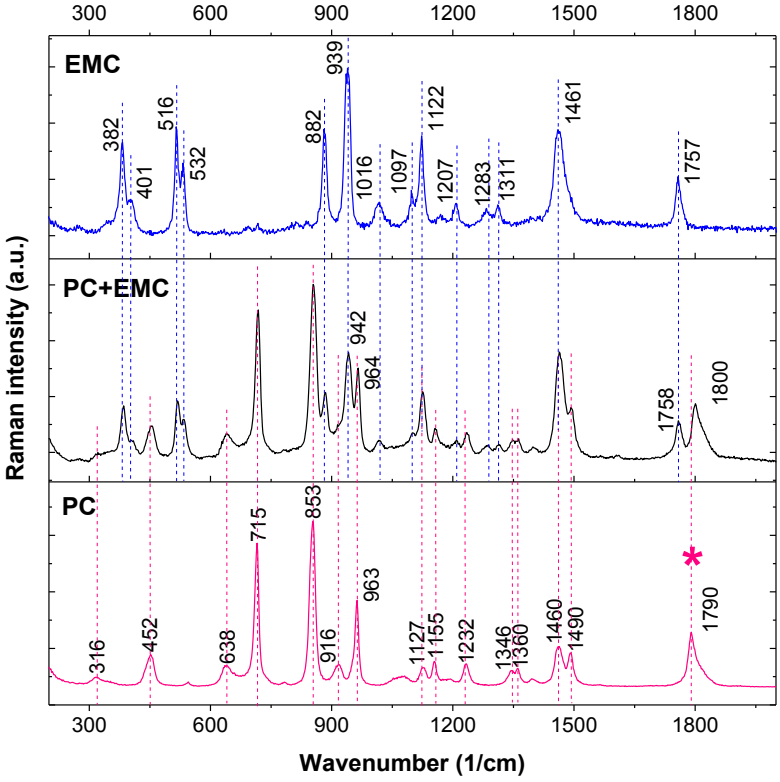

Figure 4.13 Peak shift of the PC in PC-EMC mixed solvent comparing to the peaks of pure PC and pure EMC

The interaction of PC-PC in PC-EMC mixed solvent could be considered as a molecular aggregation that is similar to other solution mentioned before. There are several molecule aggregation modes, J-aggregates, H-aggregates, S-aggregates, R-aggregates and so forth [42]. It was identified that the absorbance peak would be red-shift (J type) or blue-shift (H, S and R type) in different aggregation type. In *Figure 4.13*, only one blue-shift peak could be observed at C=O bond. The aggregate type of PC maybe H, S or R type dominated with a bind site of C=O. The accurate structure needs to be simulated by extra computational calculation, but not demonstrated in this study.

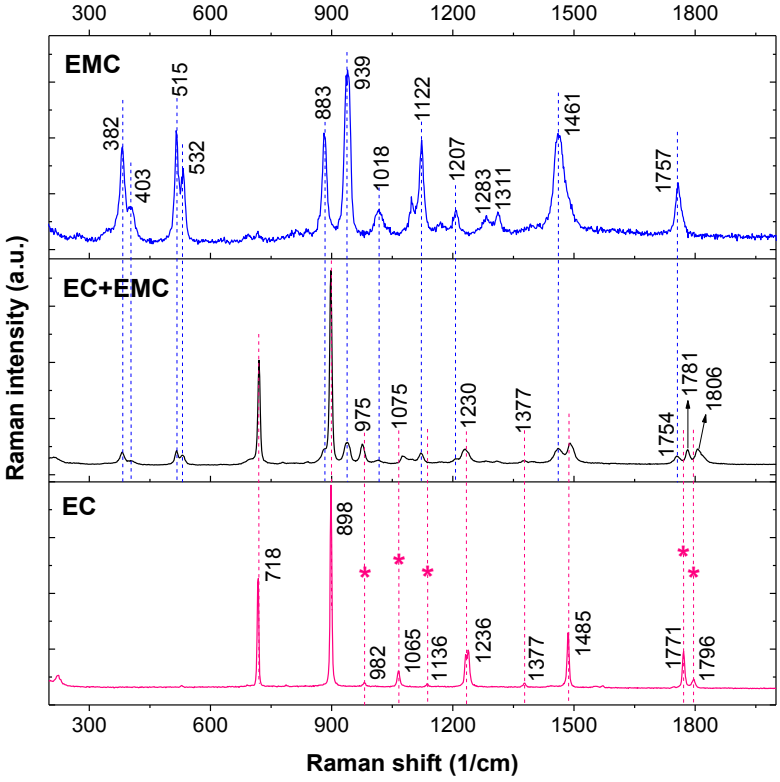

Figure 4.14 Peak shift of the EC in EC-EMC mixed solvent comparing to the peaks of pure EC and pure EMC

In the same way, Raman spectra of pure EC, pure EMC, pure DMC, mixed solvent EC-EMC and PC-EMC mixed solvent were measured and displayed in *Figures 4.14* and *4.15*. Similar to PC-EMC, the peaks of EMC in EC-EMC and the peaks of DMC in EC-DMC were not shifted comparing with pure EC. However, in the 10 peaks of EC in EC-EMC, 5 peaks were shifted obviously (marked with asterisks in *Figure 4.14*). There are three blue-shift peaks, 1075 cm^{-1} (shifted from 1065 cm^{-1} in pure EC), 1781 cm^{-1} (from 1771 cm^{-1}) and 1806 cm^{-1} (from 1796 cm^{-1}), and one red-shift peak, 975 cm^{-1} (from 982 cm^{-1}). Besides, the peak at 1136 cm^{-1} disappeared in the EC-EMC mixed solvent. The blue-shift C=O peak (1781 cm^{-1} and 1806 cm^{-1}) and the blue-shift in-plane ring stretching (1075 cm^{-1}) suggest the binding site of EC-EC is not only C=O vibration, but also the ring plane vibration. In the case of S or R aggregates unit, a stronger in-plane ring interaction would lead to more aggregation number. Although there have been some controversies on the solvation number of the Li^+ ion in PC and EC electrolytes, many research suggested that EC show stronger aggregation and more aggregation number than PC [43]. According to the PC-PC interaction and EC-EC interaction observed in this study, EC also show stronger aggregation than PC, and may further lead to more aggregate number.

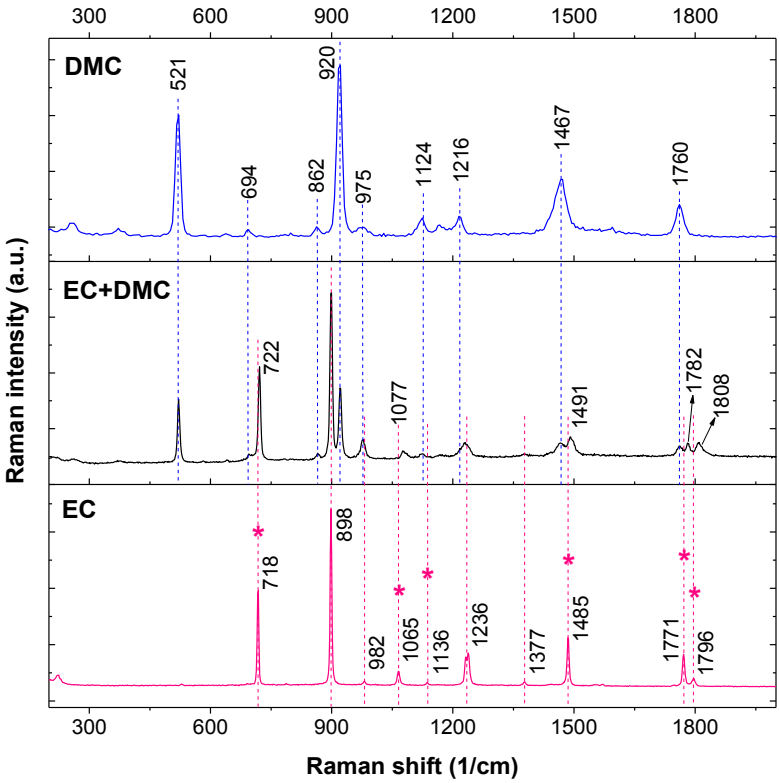

Figure 4.15 Peak shift of the EC in EC-DMC mixed solvent comparing to the peaks of pure EC and pure EMC

In the 10 peaks of EC from EC-DMC, 6 peaks were shifted obviously (marked with asterisks in *Figure 4.15*). There are 5 blue-shift peaks, 722 cm^{-1} (shifted from 718 cm^{-1}), 1077 cm^{-1} (from 1065 cm^{-1}) and 1491 cm^{-1} (from 1485 cm^{-1}), 1782 cm^{-1} (from 1771 cm^{-1}) and 1808 cm^{-1} (from 1796 cm^{-1}). Besides, the peak at 1136 cm^{-1} also disappeared in the EC-DMC mixed solvent. The blue-shift C=O peak (1790 cm^{-1} and 1806 cm^{-1}) and the blue-shift in-plane ring stretching (1075 cm^{-1}) suggest the binding site of EC-EC is not only C=O vibration, but also the ring plane vibration. The more shift peaks of EC indicate that EC in EC-DMC show even more aggregation than it in EC-EMC. The aggregation number of EC in EC-DMC maybe more than EC is in EC-EMC.

In conclusion, the aggregation force and number may follow the order: EC (in EC-DMC) > EC (in EC-EMC) > PC (in PC-EMC). This order follows the same order of the interfacial molar fraction in *Figure 4.10*. It suggests that the aggregation of solvent molecules may be related to the interfacial molar fraction of PC and EC at the graphite surface in some ways.

4.3.2 Depth profile on SEI formed on graphite anode, using Raman spectroscopy and SERS

In order to obtain more information about Li_2CO_3 in SEI film, depth profile measurement was further conducted to estimate the Li_2CO_3 location. To avoid the thermal damage, laser power was reduced to 3 mW. *Figure 4.16* illustrates the depth profile on each peak in SERS spectra of SEI film formed from PC-based electrolyte. The depth profiling was conducted in micrometer scale due to the objective lens we used is 50x long-focus with low numerical aperture (NA) value, so that the depth resolution is not high enough for accurate depth profile. The estimated SEI film from 0 to 5 μm is not indicating the thickness of actual SEI film, but only represent the relative depth displacement in micrometer level. The vertex of the depth profile on G peak can be considered to figure out the surface of graphite anode. The increase and subsequent vertex (marked as (1)) in the Raman intensity of the G peak likely correspond to the laser beam moved from interior SEI film toward the graphite surface. Significant increase in I(1380 cm^{-1}) toward vertex (1) likely corresponds to the laser beam moving toward graphite surface as well, since peak 1380 cm^{-1} mainly come from the C−C vibration from graphite edge. Besides, the peak at 1380 cm^{-1} is also partially from the organic vibration C-H. Thus, the slight bump around location (3) maybe from the organic component in SEI film. The depth profile on I(910 cm^{-1}), which corresponds to the CH_3 and CH_2 vibration of organic product $ROCO_2Li$ [44], gradually decreases but maintains higher intensity (from (2) to (4)) until near graphite surface. It is roughly equal to the profile of various bond of interior SEI film. Moreover, the depth of I(290 cm^{-1}) is believed to be related to the distribution of Li_2CO_3, which here appears to be embedded in the outer layer (around location (2)) of organic SEI film. It reveals that the Li_2CO_3 produced from PC-based electrolyte does not consist the innermost layer of SEI, but being embedded in the organic compounds around interior layer. The depth profile in *Figure 4.16* only preliminarily distinguishes the relative position of Li_2CO_3 in SEI film.

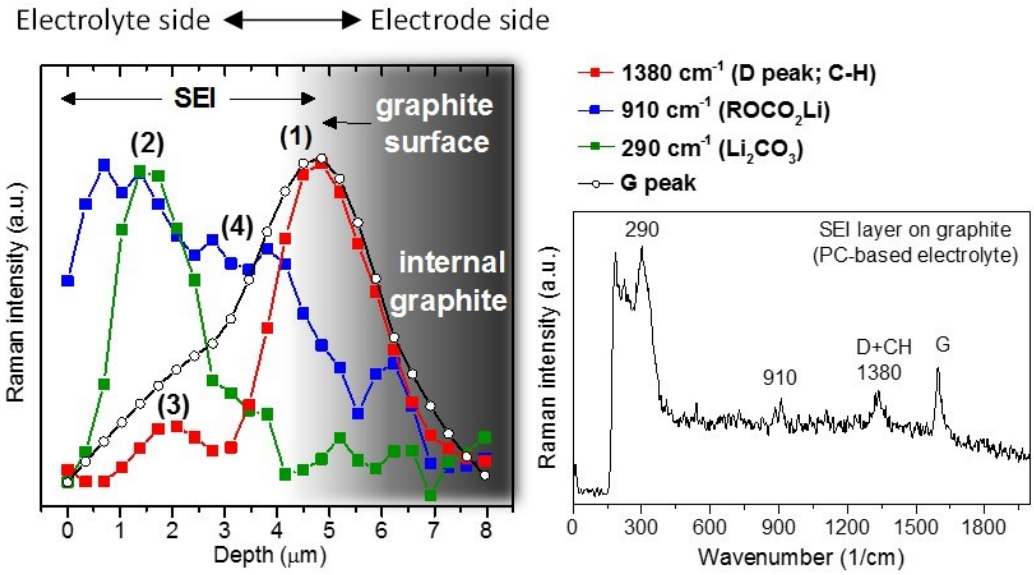

Figure 4.16 Depth profile of the SEI film formed from Li-PC-EMC. Right: Dependence of Raman intensity of the 4 peaks in the left graph on depth displacement; Left: SERS spectra of the SEI film formed by Li-PC-EMC. Location (1) suggests the surface of graphite; positions from (2) to (4) reflect the organic compounds in the entire SEI film; location (3) indicates the C-H chain of the SEI film; the Li_2CO_3 peak appears at a higher intensity around location (2) and (3).

4.4 Conclusion

The study in this chapter describes the interfacial analysis in Li-ion batteries by using a special designed Au NPs SERS sensor.

Firstly, the SERS spectra of the SEI film revealed the presence of Li_2CO_3 in PC-based electrolyte and the absence of Li_2CO_3 when using EC-based electrolyte.

Besides, Raman mapping studies were performed to elucidate the interfacial behavior of the PC and EC and its correlation with the Li_2CO_3 generation. The interfacial behavior of PC and EC at the graphite surface was found to be different. Molar fraction of PC at the interface was lower than bulk sample, especially at the edge of graphite. Contrarily, the molar fraction of EC at the graphite surface is similar to bulk sample and higher than PC. It indicates that the interfacial molar fraction of cyclic carbonate may affect the reduction pathway (1-electron reduction or 2-electron reduction) and further influence the formation of Li_2CO_3 product.

Finally, the rough depth profile on the Li_2CO_3 was conducted by using SERS sensor and reveal that Li_2CO_3 products may be embedded in organic layers of SEI film.

The SERS measurement, Raman mapping and depth profile on SEI film could give a closer look at the SEI composition, reaction mechanism and internal SEI structure from the viewpoint of bond vibration. It is possible to gain new insight into understanding interfacial reaction and expect the application of well-designed SERS sensor in SEI observation.

References

[1] Y. Wang, S. Nakamura, M. Ue, P.B. Balbuena, Journal of the American Chemical Society, 123 (2001) 11708-11718.

[2] D. Aurbach, Y. Ein - Eli, Journal of The Electrochemical Society, 142 (1995) 1746-1752.

[3] Y. Ein - Eli, S.F. McDevitt, D. Aurbach, B. Markovsky, A. Schechter, Journal of The Electrochemical Society, 144 (1997) L180-L184.

[4] S.H. Kang, D.P. Abraham, A. Xiao, B.L. Lucht, Journal of Power Sources, 175 (2008) 526-532.

[5] A.M. Andersson, K. Edström, Journal of The Electrochemical Society, 148 (2001) A1100-A1109.

[6] E. Peled, D. Bar Tow, A. Merson, A. Gladkich, L. Burstein, D. Golodnitsky, Journal of Power Sources, 97–98 (2001) 52-57.

[7] G.V. Zhuang, P.N. Ross, Electrochemical and Solid-State Letters, 6 (2003) A136-A139.

[8] P. Verma, P. Maire, P. Novák, Electrochimica Acta, 55 (2010) 6332-6341.

[9] K. Edström, M. Herstedt, D.P. Abraham, Journal of Power Sources, 153 (2006) 380-384.

[10] S. Malmgren, K. Ciosek, M. Hahlin, T. Gustafsson, M. Gorgoi, H. Rensmo, K. Edström, Electrochimica Acta, 97 (2013) 23-32.

[11] M. Nie, D. Chalasani, D.P. Abraham, Y. Chen, A. Bose, B.L. Lucht, The Journal of Physical Chemistry C, 117 (2013) 1257-1267.

[12] H. Bryngelsson, M. Stjerndahl, T. Gustafsson, K. Edström, Journal of Power Sources, 174 (2007) 970-975.

[13] M. Nie, D.P. Abraham, Y. Chen, A. Bose, B.L. Lucht, The Journal of Physical Chemistry C, 117 (2013) 13403-13412.

[14] R. Dedryvère, S. Leroy, H. Martinez, F. Blanchard, D. Lemordant, D. Gonbeau, The Journal of Physical Chemistry B, 110 (2006) 12986-12992.

[15] G.V. Zhuang, H. Yang, B. Blizanac, P.N. Ross, Electrochemical and Solid-State Letters, 8 (2005) A441-A445.

[16] Z. Wang, Y. Sun, L. Chen, X. Huang, Journal of The Electrochemical Society, 151 (2004) A914-A921.

[17] Z. Wang, X. Huang, L. Chen Journal of The Electrochemical Society, 151 (2004) A1641-A1652.

[18] N. Liu, H. Li, Z. Wang, X. Huang, L. Chen, Electrochemical and Solid-State Letters, 9 (2006)

A328-A331.

[19] Z. Wang, X. Huang, L. Chen Journal of The Electrochemical Society, 150 (2003) A199-A208.

[20] P. Lu, C. Li, E.W. Schneider, S.J. Harris, The Journal of Physical Chemistry C, 118 (2014) 896-903.

[21] R. Marom, O. Haik, D. Aurbach, I.C. Halalay, Journal of The Electrochemical Society, 157 (2010) A972-A983.

[22] S. Shi, P. Lu, Z. Liu, Y. Qi, L.G. Hector, H. Li, S.J. Harris, Journal of the American Chemical Society, 134 (2012) 15476-15487.

[23] S. Shi, Y. Qi, H. Li, L.G. Hector, The Journal of Physical Chemistry C, 117 (2013) 8579-8593.

[24] P. Lu, S.J. Harris, Electrochemistry Communications, 13 (2011) 1035-1037.

[25] K. Xu, Chemical Reviews, 114 (2014) 11503-11618.

[26] Y. Hase, I.V.P. Yoshida, Spectrochimica Acta Part A: Molecular Spectroscopy, 35 (1979) 379.

[27] D. Alves Dalla Corte, G. Caillon, C. Jordy, J.-N. Chazalviel, M. Rosso, F. Ozanam, Advanced Energy Materials, 6 (2016) 1501768-n/a.

[28] G.V. Zhuang, H. Yang, B. Blizanac, P.N. Ross, Electrochemical and Solid-State Letters, 8 (2005) A441-A445 %@ 1099-0062.

[29] Y. Chernyak, Journal of Chemical & Engineering Data, 51 (2006) 416-418.

[30] J. John J. McKetta, Encyclopedia of Chemical Processing and Design, CRC Press, 1984.

[31] M. Takeuchi, N. Matubayasi, Y. Kameda, B. Minofar, S.-i. Ishiguro, Y. Umebayashi, The Journal of Physical Chemistry B, 116 (2012) 6476-6487.

[32] O.O. Postupna, Y.V. Kolesnik, O.N. Kalugin, O.V. Prezhdo, The Journal of Physical Chemistry B, 115 (2011) 14563-14571.

[33] N. Kometani, H. Nakajima, K. Asami, Y. Yonezawa, O. Kajimoto, The Journal of Physical Chemistry B, 104 (2000) 9630-9637.

[34] H. Yao, T. Isohashi, K. Kimura, The Journal of Physical Chemistry B, 111 (2007) 7176-7183.

[35] A. Chowdhury, S. Wachsmann-Hogiu, P.R. Bangal, I. Raheem, L.A. Peteanu, The Journal of Physical Chemistry B, 105 (2001) 12196-12201.

[36] K. Kon-No, T. Jin-No, A. Kitahara, Journal of Colloid and Interface Science, 49 (1974) 383-389.

[37] E. Ruckenstein, R. Nagarajan, The Journal of Physical Chemistry, 84 (1980) 1349-1358.

[38] T. Wärnheim, Current Opinion in Colloid & Interface Science, 2 (1997) 472-477.

[39] M. Deepa, S.A. Agnihotry, D. Gupta, R. Chandra, Electrochimica Acta, 49 (2004) 373-383.

[40] H. Tsunekawa, A. Narumi, M. Sano, A. Hiwara, M. Fujita, H. Yokoyama, The Journal of

Physical Chemistry B, 107 (2003) 10962-10966.

[41] C.M. Burba, R. Frech, The Journal of Physical Chemistry B, 109 (2005) 15161-15164.

[42] J. Kunzler, L. Samha, R. Zhang, H. Samha.

[43] Y. Kameda, Y. Umebayashi, M. Takeuchi, M.A. Wahab, S. Fukuda, S.-i. Ishiguro, M. Sasaki, Y. Amo, T. Usuki, The Journal of Physical Chemistry B, 111 (2007) 6104-6109.

[44] S. Matsuta, T. Asada, K. Kitaura, Journal of the Electrochemical Society, 147 (2000) 1695-1702.

Chapter 5: General conclusion

5.1 Conclusion

Interface reaction occurs in a wide variety of fields and plays a key role in understanding the various phenomena. The investigation in interfacial reaction requires experimental methods, which discriminate interfacial structure with high resolution. Raman spectroscopy can support the information of molecular vibration in situ and kinetically, which are the advantages for observing interfacial phenomenon. Moreover, a suitable SERS sensor can enhance the sensitivity of Raman scattering from the small amount component. Therefore, in this study, the investigation was carried out in the interfacial reaction that takes place in three samples, APTES SAMs, SLG and SEI film, by using Raman spectroscopy and SERS.

The studies were completed in two parts: demonstration and application. For demonstration, chapter 2 describes the depth profile on internal structure of APTES SAMs in atomic level and the time-resolved investigation in the kinetic reaction of APTES SAMs and SLG, by using Raman spectroscopy and SERS. The originalities of chapter 2 are firstly realizing depth profile on ultra-thin sample in nanometer scale using SERS, firstly finding the phase transition point of APTES SAMs and the thermal stability of SLG under laser heating. For application, chapter 3 presents the kinetic observation on the SEI film formation in LIB by using SERS. The originalities are firstly applying transmission type SERS sensor to the observation of SEI film in LIB and monitoring SEI formation. Chapter 4 further observes the depth profile on SEI film and analyzes the reaction mechanism of Li_2CO_3 formation. The originalities are firstly detecting Li_2CO_3 using SERS sensor, figuring out the correlation of Li_2CO_3 formation with interfacial molar fraction of cyclic carbonate, and depth profiling on the SEI film using SERS sensor.

The depth profile using SERS is realized in high resolution in chapter 2. The internal structure of APTES SAMs is discussed. An ideal APTES SAMs on silica surface supposed to be the one single molecule layer, while the alignment of APTES molecule has been demonstrated to be not orderly in actual preparation. The depth profile on APTES SAMs was measured using Ag NPs as SERS sensor. To control the accurate depth position when measuring depth profile, a piezo field gradient stage was installed. As a result, the internal structure was vertically distinguished from some specific variation, Ag-N, NH_2, CH_2, Si-O, and so on. Moreover, some frequency shifts occurred during depth profiling and could be analyzed to discuss the bonding behaviors at the interfaces. The depth profile and frequency shift of NH_2 suggest a lot of free amino groups, because some hydrogen bonds maybe formed on amines at the substrate surface. It is also possible that some of the molecules aligned towards the substrate surface with the head and tail groups.

From the frequency shift of Si-O bond, it could speculate that not every APTES molecule was bonded with each other, free and bonded Si–O band existed at the same time.

Besides, the kinetic observations under laser heating are discussed in chapter 2. Using the surface-enhanced anti-Stokes and Stokes Raman scattering, the kinetic variation of the peaks of APTES SAMs is recorded. The phase transition point is calculated to be around 118 °C. Furthermore, phase change process can be analyzed in detail. Thermal damage could be primarily responsible for the variation in the O–Si–O, Si–C–C and carbon chain, and the Si–O–Si bands, the bending vibration at Si–CH_2 and the NH_2 group still show high SERS sensitivity after the phase change. Other than APTES SAMs, the kinetic surface reactions of SLG basal plane and edge under excitation laser heating are also investigated. The thermal instability is calculated to occur around 220 ºC at the edge, but more than 500 ºC at the basal. Moreover, the peaks ratio suggest that the oxygen bond increased in pace with defect increasing at the basal. However, at SLG edge plane, point defects were partially eliminated fist at low temperature and generated again above 220 ºC. The results in chapter 2 demonstrate the capability of Raman spectroscopy and SERS in interfacial analysis.

The application of SERS in Li-ion battery is discussed in chapters 3 and 4. The studies are focused on the comparison of EC and PC, because PC was demonstrated to be bad at forming effective SEI. The difference between EC and PC may lead to a new insight into understanding the influence of interfacial reaction on the formation of SEI film. The kinetic observation on SEI film and thermal stability at the graphite electrode are monitored using Ag NPs transmission SERS sensor. The results suggest that, an apparent new peak appear when using Li-PC-EMC, comparing to the peaks observed from Li-EC-EMC. This peak maybe attributed to the organic compounds Li_2CO_3. Moreover, the kinetic reaction is also monitored using 11 x 11 multi laser spots. The real-time area monitoring at the HOPG anode demonstrates that Li_2CO_3 and $ROCO_2Li$ should be generated at the edge of graphite and the formation of ROLi product occur at both of edge and basal plane of graphite.

The formation of Li_2CO_3 is reinforced in chapter 4 from the observation on SEI film using Au NPs sensor. The SERS spectra further demonstrate the presence of Li_2CO_3 product in PC-based electrolyte and the absence of Li_2CO_3 when using EC-based electrolyte. To understand the mechanism of Li_2CO_3 formation, the interfacial behavior of PC and EC at the graphite surface was analyzed. Molar fraction of PC at the interface was found to be lower than its bulk sample. On the contrary, the molar fraction of EC at the graphite surface is also similar to bulk sample and higher than PC. The lower molar fraction of PC maybe related to lower aggregate number of PC-

PC comparing to EC-EC aggregate. Besides, using HOPG as graphite model, the lower molar fraction of PC was further demonstrated to occur at the edge of graphite only. The edge of graphite is exact the main reaction position for SEI formation. Based on the reaction formula of Li_2CO_3, Li_2CO_3 could be formed at the edge of graphite via two-electron reduction. The lower interfacial molar fraction of PC at the graphite surface makes PC access more electrons, which may affect the reduction pathway to more two-electron reduction and further generate more Li_2CO_3 products. Finally, the depth profiling of SEI film formed in PC-based electrolyte was preliminarily distinguished in micrometer scale. The relative position of Li_2CO_3 in SEI film was observed to be far away from the graphite surface and embedded in the organic compounds. It reveals that the Li_2CO_3 produced from PC-based electrolyte does not consist the innermost layer of SEI, but embedded in the interior layer together with other organic components.

The results in this thesis demonstrate the capacity of SERS and Raman spectroscopy when analyzing interfacial reaction. The measurements on APTES SAMs and SLG with well-known structure, not only support the demonstration, but also help to find new phenomena. The application of SERS was also successfully realized in detecting SEI film in Li-ion battery. The in-situ observation on thin-film materials was completed with atomistic resolution, high quality, and kinetically by using SERS. These studies shown high potential of SERS to be applied in various interfacial reaction processes.

5.2 Perspectives

This thesis demonstrates the potential of SERS to interfacial analysis of thin-film materials. The depth profiling of APTES SAMs show a spectroscopic method for distinguishing interior structure of ultra-thin layer sample. The observation on the thermal stability of APTES SAMs and SLG suggest an effective approach for studying kinetic reaction. It has high potential to be used in investigating vertical structure of organic and inorganic thin-film structure, in monitoring temperature variation of a number of materials no matter at ultra-high temperature or low temperature, and in analyzing kinetic reaction of various physical and chemical processes.

The original observation in this these could also be useful to many fields. The phase transition point of APTES SAMs and thermal stability of SLG demonstrated in this thesis could support the further research and industrial application. The detection of Li_2CO_3 supplies more evidence for the controversies about SEI film and helps to further understand the reaction mechanism of SEI film formation from all aspects.

However, there are many issues could be improved step by step in the application of SERS in SEI film. The in-situ cell did not support the three electrodes measurement, so that it cannot monitor the accurate potential of working electrode. Improving the design or setting up a glove box on the Raman machine are possible solution to this issue. In addition, there are also some possible issues about SERS sensors could be improved, such as damage of SEI outer layer from SERS sensor, improvement on SERS sensor for the objective lens with higher numerical aperture, optimization of Au NPs diameter to elevate the SERS sensitivity for SEI detection, and so on. Not only the application in the observation on SEI film, when using SERS on any other materials, the SERS sensor would be always one of the key point.

Designing suitable sensor to each material, making flexible use of the advantage of Raman spectroscopy and SERS, and combing with other supporting device, the analysis on many tough materials is expected to realize more and more in future.

List of Achievements

Original articles

Estimated phase transition and melting temperature of APTES self-assembled monolayer using surface-enhanced anti-stokes and stokes Raman scattering, Applied Surface Science, 363, 572–577, 2016.
Yingying Sun, Masahiro Yanagisawa, Masahiro Kunimoto, Masatoshi Nakamura and Takayuki Homma

Thermal stability of single-layer graphene subjected to confocal laser heating investigated by using in situ anti-Stokes and Stokes Raman spectroscopy, Electrochemistry, 2016 (In press)
Yingying Sun, Masahiro Yanagisawa, and Takayuki Homma

Presentations

In-situ Raman spectroscopy study on the preferential adsorption of electrolyte species on electrode surface of Lithium ion battery, PRiME 2016/230th ECS meeting, E03-1596, Oct. 2016, Hawaii, USA,
Yingying Sun, Masahiro Yanagisawa, and Takayuki Homma

In-situ temperature measurements on the phase change point of monolayer APTES by Surface-enhanced anti-Stokes and Stokes Raman scattering, The 7th International symposium on surface science, Nov. 2014, Shimane, Japan,
Yingying Sun, Masahiro Yanagisawa, Masahiro Kunimoto, Masatoshi Nakamura and Takayuki Homma

Depth profiling of APTES self-assembled monolayer using surface-enhanced confocal Raman microspectroscopy, 表面科学学術講演会要旨集, 34, 129, 2014, Shimane, Japan,
Yingying Sun, Masahiro Yanagisawa, Masahiro Kunimoto, Masatoshi Nakamura and Takayuki Homma

Study on chemical structure inside APTES SAMs by using SERS: depth profile and phase transition process, CSJ2015, Tokyo, Japan,
Yingying Sun, Masahiro Yanagisawa, Masahiro Kunimoto, Masatoshi Nakamura and Takayuki Homma

Acknowledgements

Acknowledgements

This thesis is not only a milestone in more than three years of work at Waseda University and specifically within the Homma Lab., it is also the result of many experiences I have encountered at Waseda University and my research sites from dozens of remarkable individuals who I also wish to acknowledge. All of these made my experience in Japan has been nothing short of amazing.

First and foremost, I would like to acknowledge and express my heartfelt gratitude to my academic supervisor, Prof. Takayuki Homma for the continuous support of my Ph.D. study and related works, for his patience, motivation, and immense knowledge. His insightful comments throughout the research incented me to widen my research from various perspectives and with an elaborated methodology. I admire his rigorous attitude towards research.

Besides, I would like to thank Prof. Masahiro Yanagisawa, who helped me with the experiments and analysis, and guided me during the three-year Ph.D. course. His academic guidance and metal support help me to pass through the most difficult times when performing experiments, facing difficulties and writing papers. My sincere thanks also go to Assistant Prof. Masahiro Kunimoto, who motivated me and provided academic suggestions since I came to Japan. His enthusiastic attitude always let me feel released in this alien land. Many heartfelt thanks to Prof. Mikiko Saito, whose mutual care and concern always let me feel warm when I was under pressure. There are also many thanks to Prof. Yasuhito Fukunaka, who always give me precious advices at the weekly seminar and interim reports.

Moreover, I would like to thank the referees of my defense committee, Prof. Yoshiyuki Sugahara, Prof. Toshiyuki Momma and Prof. Kazuyuki Kuroda. Their inspiring comments and thoughtful insights taught me so much and helped me to perfect my thesis.

Furthermore, my heartfelt thanks go to my labmates Mr. Siggi Wodarz for his great support during the daily work and Ph.D. degree application. In addition, I thank my labmates Mr. Yasuhiro Tsuyuki, Ms. Minami Tsuzuki and Mr. Hidenori Takai for they generously sharing the glovebox with me. I also thank my groupmates, Mr. Masatoshi Nakamura, Ms. Moe Sasaki, Mr. Futa Yamaguchi, Mr. Yuta Sato, Mr. Satoru Yoshida, Mr. Ryouto Arahara, Mr. Nobuhito Onozuka and Mr. Tetsuya Yasuda. Our working for the project “Sentan keisoku” will always be the precious memory after my graduation. I also would like to thank my labmates, who are also international students, Ms. Ahn, Mr. Akash, Ms. Lin and Mr. Chris, for the stimulating discussions not only on

academic topic but also on the various cultures all over our colorful world. I will never forget all the fun we have had in the last many years and the precious time we spend in Japan.

I acknowledge the Ministry of Education, Culture, Sport, Science and Technology of Japan for providing me the scholarship to facilitate my Ph.D. research in the department of applied chemistry, Waseda University.

Last but not the least, my greatest appreciation goes to my family: my parents for supporting me spiritually throughout my free life and as well as my beloved person for all your love, patience, and encouragement during our short journey in Japan and in future.

Without all these precious support it would not be possible to enjoy this journey.